UNDERSTANDING EFFECTS OF NANO AND MICRO SCALE ADDITIVES ON RHEOLOGICAL, BUILDABILITY, AND MECHANICAL CHARACTERISTICS OF 3D PRINTED CONCRETE

A Dissertation

by

UGUR KILIC

Submitted to
School of Engineering and Applied Science of
University of Virginia

In partial fulfillment of the requirements of the degree of

DOCTOR OF PHILOSOPHY

in

Engineering Systems and Environment

May 2023

UNDERSTANDING EFFECTS OF NANO AND MICRO SCALE ADDITIVES ON RHEOLOGICAL, BUILDABILITY, AND MECHANICAL CHARACTERISTICS OF 3D PRINTED CONCRETE

A Dissertation

by

UGUR KILIC

Submitted to
School of Engineering and Applied Science of
University of Virginia

In partial fulfillment of the requirements of the degree of

DOCTOR OF PHILOSOPHY

in

Engineering Systems and Environment

Approved by:

Chair of Advisory Committee:	Jose Gomez
Committee Members	Osman E. Ozbulut (Advisor)
	Devin K. Harris
	Ji Ma
	Ehsan Baharlou
	Gabriel A. Amador

May 2023

Dedication

To my lovely family

Abstract

Understanding Effects of Nano and Micro Scale Additives on Rheological, Buildability, and Mechanical Characteristics of 3D Printed Concrete

Ugur Kilic
B.Sc. Middle East Technical University
M.S. University of Virginia

Advisor: Osman E. Ozbulut
Associate Professor, Department of Engineering Systems and Environment
University of Virginia

3D Concrete Printing (3DCP) is an emerging construction technology where the design, fabrication, and assembly process is digitally controlled. The cementitious mixtures used in 3DCP need to satisfy various rheological properties at different stages of 3DCP process such as pumping, extruding, and building. A workable mixture with low plastic viscosity and dynamic yield stress is needed during pumping and extrusion processes, while a mixture with high static yield stress and high thixotropy is needed to ensure shape retention and buildability. Due to these contradicting requirements, the research on the rheological properties of 3D printable cementitious mixtures is important for the development of novel mixtures for 3DCP. While contemporary mix design for 3DCP relies on a trial-and-error procedure, a scientific understanding on the effects of different additives on rheological properties of fresh cementitious mixtures can guide the mix design for 3DCP. As fresh state properties of printable mixtures are important to ensure smooth fabrication of 3D printed concrete structures, achieving good hardened-state properties of printed mixtures is essential to truly leverage the benefits offered by this technology. Incorporating nano and micro-scale fibers into printable mixtures can improve performance of 3D printed concrete structures.

This research aims to develop an understanding on the role of different additives on rheological characteristics and printability of cementitious mixtures as well as mechanical performance of 3D printed samples. First, the influence of a starch-based viscosity modifying agent (VMA) and attapulgite nanoclay (ANC) on rheo-viscoelastic and printability characteristics of cementitious

mixtures is evaluated. Then, the effect of cellulose nanofibers (CNF) on rheological and printability characteristics of the cementitious mixtures is evaluated. Next, the development of high-performance 3D printable mixtures using graphene nanoplatelets (GNPs) or polyethylene (PE) fibers is explored. The rheology of the GNP-reinforced and PE fiber reinforced cementitious mixtures is thoroughly evaluated using a shear rheometer. Tensile, flexural and compressive test specimens are fabricated using a 3D concrete printer with a screw type pumping mechanism. The mechanical tests are conducted in two directions, parallel and perpendicular to the printing direction, to evaluate the effect of anisotropy in 3D printed specimens. The findings of these investigations indicates that ANC can effectively alter rheo-viscoelastic properties of mortar composites for 3DCP, while the GNPs and PE fibers significantly enhance mechanical properties of 3D printed samples. In addition, tensile and flexural behavior of 3D printed samples shows considerable anisotropy.

Acknowledgement

I would like to express my deep appreciation and sincere gratitude to my advisory committee for their invaluable guidance and support throughout my dissertation work. My advisor, Dr. Osman E. Ozbulut, has been an inspiring mentor whose continuous support, encouragement, and guidance have been the key enablers for the successful completion of this dissertation. I consider it a great honor to have been granted the chance to collaborate with him during my doctoral studies at the University of Virginia. I am grateful for the continuous support and feedback provided by the other committee members, Dr. Devin K. Harris, Dr. Jose Gomez, Dr. Ji Ma, Dr. Ehsan Baharlou, and Dr. Gabriel A. Amador. I thank them for their valuable input, which has improved the quality of my research and my ability to conduct research in the future.

I also would like to express my gratitude to Mr. Sebring Alden Smith from Lacy Hall for his exceptional help and support in test setup and test specimen preparation. I also want to thank to Mr. William “Bill” Ordel and Mr. Kenneth “Ken” Herrick from Virginia Transportation Research Council for their guidance and assistance in setting up some of my tests and preparing some test specimens for my experiments.

I would like to acknowledge the support I received from the Department of Engineering Systems and Environment in pursuing my graduate studies at the University of Virginia. I would like to express my appreciation to Ryan W. Henry, the Laboratory Manager of Engineering Systems and Environment, for his support during the course of my research.

I would like to extend my appreciation to my friends, Abdou K. Ndong, Zhangfan Jiang and Heze Chen for their encouragement and support throughout my academic journey. Their friendship and support have been invaluable to me.

Finally, I am grateful to my family for their unwavering love and support throughout my academic journey. Without their support, none of my achievements would have been possible.

Nomenclature

3DCP	3D Concrete Printing
ACI	American Concrete Institute
AM	Additive Manufacturing
ANC	Attapulgite Nanoclay
ANOVA	Analysis of Variance
ASTM	American Society for Testing and Materials
C-S-H	Calcium Silicate Hydrate
CaCO3	Calcium Carbonate
CAD	Computer - Aided Design
CH	Calcium Hydroxide
CNF	Cellulose Nanofibers
CNT	Carbon Nanotubes
CSA	Calcium sulfoaluminate
DIC	Digital Image Correlation
DTG	First derivative of TG
DYS	Dynamic Yield Stress
EA	Expansive agent
EB	Elastic Buckling
ECC	Engineered Cementitious Composite
FA	Fly Ash
FDM	Fused Deposition Modeling
FE	Finite Element
GNP	Graphene Nanoplatelets
JSCE	Japan Society of Civil Engineers

LVER	Linear Viscoelastic Range
MCC	Microcrystalline Cellulose
MTS	Materials Testing System
NC	Nano-Clay
NS	Nano Silica
PC	Plastic Collapse
PE	Polyethylene
PP	Polypropylene
PVA	Polyvinyl Alcohol
SEM	Scanning Electron Microscope
SF	Silica Fume
SLA	Stereolithography
SLS	Selective Laser Sintering
SP	Superplasticizer
SVM	Support Vector Machine
SYS	Static Yield Stress
TGA	Thermogravimetric Analysis
UHPC	Ultra-High-Performance Concrete
VMA	Viscosity Modifying Agent
w/b	Water to binder ratio

Symbols

τ	Shear Stress
$\dot{\gamma}$	Shear Rate
τ_o	Dynamic Yield Stress
η	Plastic Viscosity
G'	Storage Modulus
G''	Loss Modulus
G^*	Complex Shear Modulus
R^2	Coefficient Of Determination
b_{exp}	Experimental Layer Breadth
n_{theo}	Expected Number of Printable Layers
n_{max}	Maximum Number of Printable Layers

Table of Contents

List of Tables

List of Figures

1. Introduction

1.1. Research Motivation

3D Concrete Printing (3DCP), which is also known as additive manufacturing of concrete or additive construction, is an emerging construction technology where the design, fabrication, and assembly process is digitally controlled. Compared with conventional concrete construction, 3DCP offers several advantages including architectural design freedom, lower labor costs, faster and more accurate construction, reduced waste, and higher degree of customization [1, 2]. Extrusion-based 3DCP, where a gantry system or robotic arm is used to deposit printable cementitious mixture through a nozzle layer-by-layer, is the most common technique for commercial applications.

The cementitious mixtures used in extrusion-based 3DCP need to satisfy various rheological properties at different stages of 3DCP process such as pumping, extruding, and building [3, 4]. Extrudability refers to the smooth and uninterrupted extrusion of the cementitious mixture through the nozzle with good surface quality [5], while buildability can be described as the ability of the printed structure to resist deformation due to the gravity induced stresses generated by the subsequent layers [6]. A workable mixture with low plastic viscosity and dynamic yield stress is needed during pumping and extrusion processes, while a mixture with high static yield stress and high thixotropy is needed to ensure shape retention and buildability. Due to these contradicting requirements, the *research on the rheological properties of 3D printable cementitious mixtures is important* for the development of novel mixtures for 3DCP.

While contemporary mix design for 3DCP relies on a trial-and-error procedure, a *scientific understanding* on the effects of different additives on rheological properties of fresh cementitious mixtures can guide the mix design for 3DCP. The use of chemical admixtures such as viscosity modifying admixtures (VMA), superplasticizers (SP), and accelerators is a common approach to alter the rheological properties of concrete and to set the required fluidity and consistency before printing [7-12]. Among these different admixtures, VMA is the most widely used admixture in cement matrix to keep the viscosity of the cementitious mix at the desired level. Another approach to modify the fresh properties of printable concrete is the use of nanomaterials. Due to their high aspect ratio, electro-mechanical interaction, and material filling mechanism at the microstructure level, nanoclay (NC) can serve as an excellent additive for altering the fresh properties of cementitious mixtures [8–10]. Although previous studies have explored the effects of NC on fresh properties of cementitious composites, there is limited understanding on the link between the fresh properties and printability characteristics of cementitious composites and their use in combination with the VMA.

Another nanomaterial that can be used to modify rheological characteristics of printable mixtures is cellulose nanofilaments (CNFs). CNFs offer unique features such as high aspect ratio, abundant availability, renewability, biodegradability, good mechanical properties and low cost [11, 12]. In addition, cellulose-based nanomaterials have been shown to enhance the mechanical properties of cementitious mixtures [13, 14]. As a result, there is a great potential for CNF to be used in 3DCP instead of the chemical admixtures for rheology modification. However, to the author's knowledge, there is no study on the use of CNF in the development of printable mixtures.

While fresh state properties of printable mixtures are important to ensure smooth fabrication of 3D printed concrete structures, *achieving good hardened-state properties of printed mixtures is essential to truly leverage the benefits offered by this technology*. Incorporating nano and micro-scale fibers into printable mixtures can improve performance of 3D printed concrete structures. Graphene nanoplatelets (GNPs) are two-dimensional carbon-based nanomaterials and have been used as a nanofiller to improve the mechanical and durability performance of cementitious materials. GNPs are known for their unique properties, such as high strength, high electrical conductivity, and high thermal conductivity [15]. These properties has made them attractive in development of high performance cementitious composites [16–19]. While the hardened properties of cast GNP-reinforced cementitious composites have been widely researched, there has been limited studies on the rheological and mechanical characteristics of GNP-reinforced printed cementitious composites.

Due to limited tensile strength and ductility of cementitious materials, current 3D concrete printing technologies require integration of reinforcement into structural members, which limits the efficiency of automatic construction and hampers fabrication of optimized complex structures. One potential approach to improve tensile properties of 3D printable mixtures is the addition of micro-scale polymer fibers such as polyvinyl alcohol (PVA), polyethylene (PE), and polypropylene (PP). Among them, PE fibers that possess a high strength-to-weight ratio can significantly improve the ductility and tensile strength of cementitious composites [20]. These fibers, comprised of long-chain hydrocarbon polymers, serve as a reinforcing material in cementitious composites, fostering a more ductile and resilient matrix [21]. The incorporation of PE fibers in the cementitious mixtures results in a synergetic effect, augmenting the interfacial bonding between the cementitious matrix and the fibers while simultaneously mitigating the formation and propagation of micro-cracks [22]. This enhanced bond strength and crack resistance consequently improve the overall durability and load-bearing capacity of the structure. As such, the integration of PE fibers into 3D printable cementitious mixtures represents a promising avenue, however, inclusion of high ratio of fibers into printable mixtures is not straightforward and requires further understanding on the effects of PE fibers on rheological properties of cementitious mixtures.

1.2. Research Goals and Objectives

This research aims to develop an understanding on the role of different additives on rheological characteristics and printability of cementitious mixtures as well as and mechanical performance of 3D printed samples. First, the influence of a starch-based viscosity modifying agent (VMA) and attapulgite nanoclay (ANC) on rheo-viscoelastic and printability characteristics of cementitious mixtures is evaluated. Then, the effect of cellulose nanofibers (CNF) on rheological, printability and mechanical characteristics of the cementitious mixtures is evaluated. Next, the development of high-performance 3D printable mixtures using graphene nanoplatelets (GNPs) or polyethylene (PE) fibers is explored. In these investigations, rheological properties are evaluated from shear rheology measurements include static yield stress, plastic viscosity, and dynamic yield stress. Viscoelastic properties including storage modulus, loss modulus and linear viscoelastic range are determined from oscillatory tests. A direct printing test using a screw type 3D concrete printing is conducted to assess the relationship between the evaluated rheo-viscoelastic properties of cement mixtures with the printability and buildability of the developed mixtures. Mechanical properties of 3D printed specimens are evaluated through direct tensile, flexural and compression testing. Along with cast specimens, printed specimens are prepared and tested considering different directions to account for process-induced anisotropy. The findings from these studies provide a better understanding on how nano and micro scale reinforcements modify rheo-viscoelastic, buildability and mechanical characteristics of 3D printable cementitious composites.

1.3. Organization of this Dissertation

This dissertation comprises eight sections that are structured as follows:

Section 1 introduces the concept of 3D printing of cementitious materials and methods for improving the fresh and hardened properties by incorporating nano and micro scale additives. The driving factors behind this research and its objectives are explained.

Section 2 provides a concise overview of the process of additive manufacturing of cementitious mixtures. Additionally, a comprehensive review of rheological and printability characterization of cementitious mixtures are presented. Furthermore, the potential improvements in fresh, buildability and mechanical properties of cementitious mixtures with nano and micro scale reinforcements is discussed.

Section 3 explains the experimental methods used in this research, encompassing the rheo-viscoelastic characterization of cementitious composites, printability and buildability assessments of cementitious mixtures, and mechanical characterization tests. Various rheological and mechanical tests, including stress growth, ramp, amplitude sweep, tensile, flexural, and compressive tests, are conducted to examine the rheological properties of the composites. Also, details about the mechanical test setup and various tests, including direct tensile, flexural and compressive tests, conducted to determine the mechanical properties of the cementitious composites.

Section 4 investigates the effects of VMA and ANC on the rheo-viscoelastic properties including static and dynamic yield stress and viscoelastic properties as well as printability characteristics of cementitious composites. ANOVA analysis, thermogravimetric analysis (TGA), and buildability assessments are conducted to evaluate the composites' performance. At the end of this section, the link between the rheological and buildability properties of 3D printable cementitious mixtures is established.

Section 5 examines the effects of CNF on the rheo-viscoelastic, printability, and mechanical characteristics of cementitious composites. Similar to section 4, this section also includes rheo-viscoelastic properties and printability characteristics of cementitious composites with various CNF concentrations. A rigorous mechanical characterization is done by testing the printed specimens in three orthogonal directions.

Section 6 explores the influence of GNP on the rheo-viscoelastic and mechanical characteristics of cementitious composites. This section focuses on the mechanical characterization, and microstructural analysis to evaluate the performance of composites containing GNP.

Section 7 assesses the effects of PE fibers on the rheo-viscoelastic and mechanical characteristics of cementitious composites. The section investigates the rheo-viscoelastic and mechanical characteristics and microstructural analysis to determine the impact of PE fibers on the composites.

Section 8 provides a summary of the research, conclusions, and recommendations. This final section highlights the key findings and suggests potential avenues for future research and practical applications in the field of cementitious composites.

2. Literature Review and Background

2.1. Additive Manufacturing of Cementitious Mixtures

Additive Manufacturing (AM), an innovative and rapidly advancing manufacturing technology, leverages metal, ceramic, and polymer materials to build three-dimensional structures layer by layer from a computer-aided design (CAD) model [23–26]. Over the last few years, this breakthrough technology has found widespread applications across a multitude of industries, such as aerospace, automotive, healthcare, consumer products, energy, and many others, revolutionizing the way products are manufactured and designed [27–29]. According to Wohler's 2022 State of 3D Printing Report, the additive manufacturing industry experienced a growth of 19.5% in 2021, a significant increase from the 7.5% growth in 2020. This rapid expansion across multiple sectors, including aerospace, healthcare, automotive, consumer products, and energy, has been a key driver for the development of various manufacturing methods like Fused Deposition Modeling (FDM), Stereolithography (SLA), Micro-stereolithography, Direct Metal Laser Sintering, Electron Beam Melting, PolyJet, Selective Laser Sintering (SLS), Laminated Object Manufacturing, Powder bed fusion, Inkjet printing, and contour crafting, among others [30, 31]. These methods share a common process of printing successive material layers on top of each other from a computer-aided design (CAD) model [1].

In the past decade, 3D printing of cementitious materials has gained significant interest in academic research and the construction industry due to its numerous advantages over traditional construction methods [32, 33]. Using this technology, fresh concrete is extruded through a nozzle on a 3D printer to build structural components layer by layer [34]. 3D concrete printing (3DCP) offers considerable flexibility in architectural design, as it eliminates the need for formworks during construction, potentially reducing labor requirements [35, 36]. Furthermore, it enables the construction of complex geometries and designs that would be difficult or impossible to achieve using conventional techniques, opening up new possibilities for architectural creativity and innovation [37, 38].

The 3DCP process can be broadly divided into several steps: design, material preparation, printer setup, layer-by-layer printing, curing, post-processing, and inspection and testing [39, 40]. The first step in 3D concrete printing is creating a digital model of the structure using computer-aided design (CAD) software. This model includes all necessary details, such as dimensions and shape, and is then converted (slicing) into a series of instructions that the 3D printer will follow, which is known as G-Code [41]. A specialized concrete mix is prepared for the printing process. This mix has specific properties to ensure it can be extruded through the printer nozzle while maintaining structural integrity. It usually contains a blend of cement, sand, aggregates, water, and additives, such as accelerators or retarders, to control the viscosity and setting time [42]. The printing process is performed using a specialized 3D concrete printer by extruding the concrete mix through the nozzle in a controlled manner, following the instructions from the G-Code. The printer moves along the X, Y, and Z axes to create the structure layer by layer. The concrete is deposited in a continuous bead, with each new layer adhering to the one below it [5, 43]. This process is shown in Figure 2-1 and repeated until the entire structure is completed. After printing, the structure is left to cure, and post-processing may be performed to improve aesthetics or structural properties.

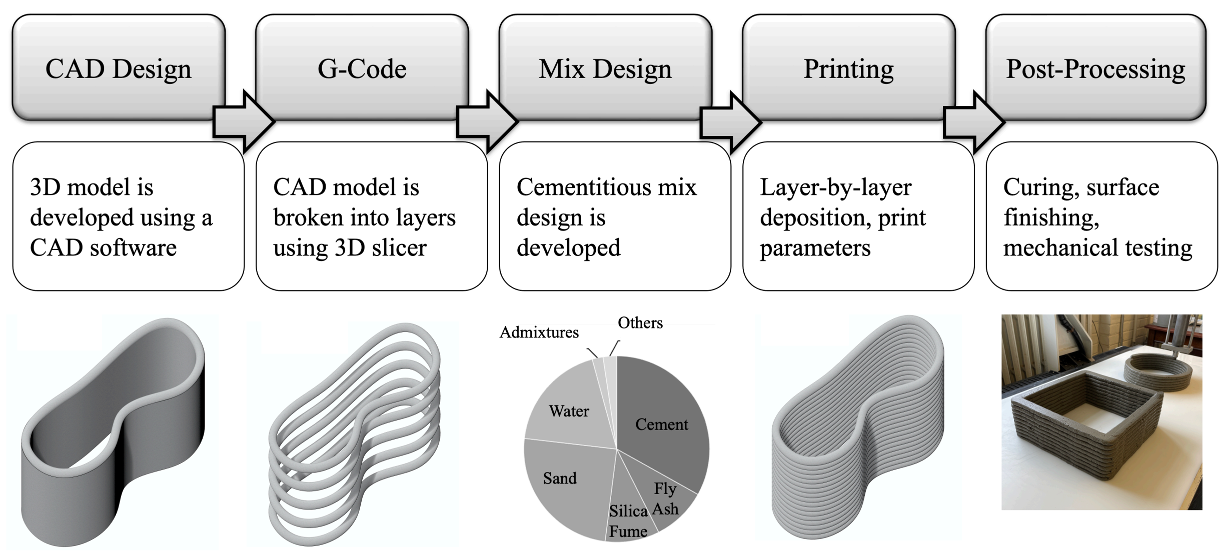

Figure 2-1: 3D printing process

The combination of additive manufacturing with other advanced technologies, such as robotics, digital fabrication, and the Internet of Things (IoT), is expected to drive the development of fully automated, smart construction systems that can improve efficiency, safety, and productivity on construction sites [44]. This convergence of technologies will not only revolutionize the construction process but also provide new opportunities for more integrated and holistic approach to building design and construction [45]. With the current technological advancements, there are three main types of 3D concrete printers that are widely used: gantry systems, robotic arm systems, and crane systems [46]. Gantry systems, as shown in Figure 2-2a, have a relatively simple and stable structure, providing high precision in the concrete extrusion process. These systems are generally more affordable and easier to maintain compared to other printer types. However, their limitations include a restricted printing area constrained by the frame size, making them less suitable for large-scale projects or complex geometries. Robotic arm systems, depicted in Figure 2-2b, offer greater flexibility and maneuverability, allowing them to print intricate and unconventional designs. These systems can also be integrated with advanced sensing and control technologies for improved performance. However, their limitations include a higher cost of implementation, increased maintenance requirements, and a smaller printing volume compared to gantry and crane systems. Lastly, crane systems, illustrated in Figure 2-2c, provide an extended reach, making them suitable for constructing large-scale structures. They can cover a vast printing area and are capable of being easily relocated, which is beneficial for projects with multiple construction sites. However, the primary limitations of crane systems include lower precision compared to gantry and robotic arm systems and potential difficulties in maintaining consistent material deposition due to the long reach of the crane. Choosing the most suitable system depends on factors such as structure size, complexity, and available resources.

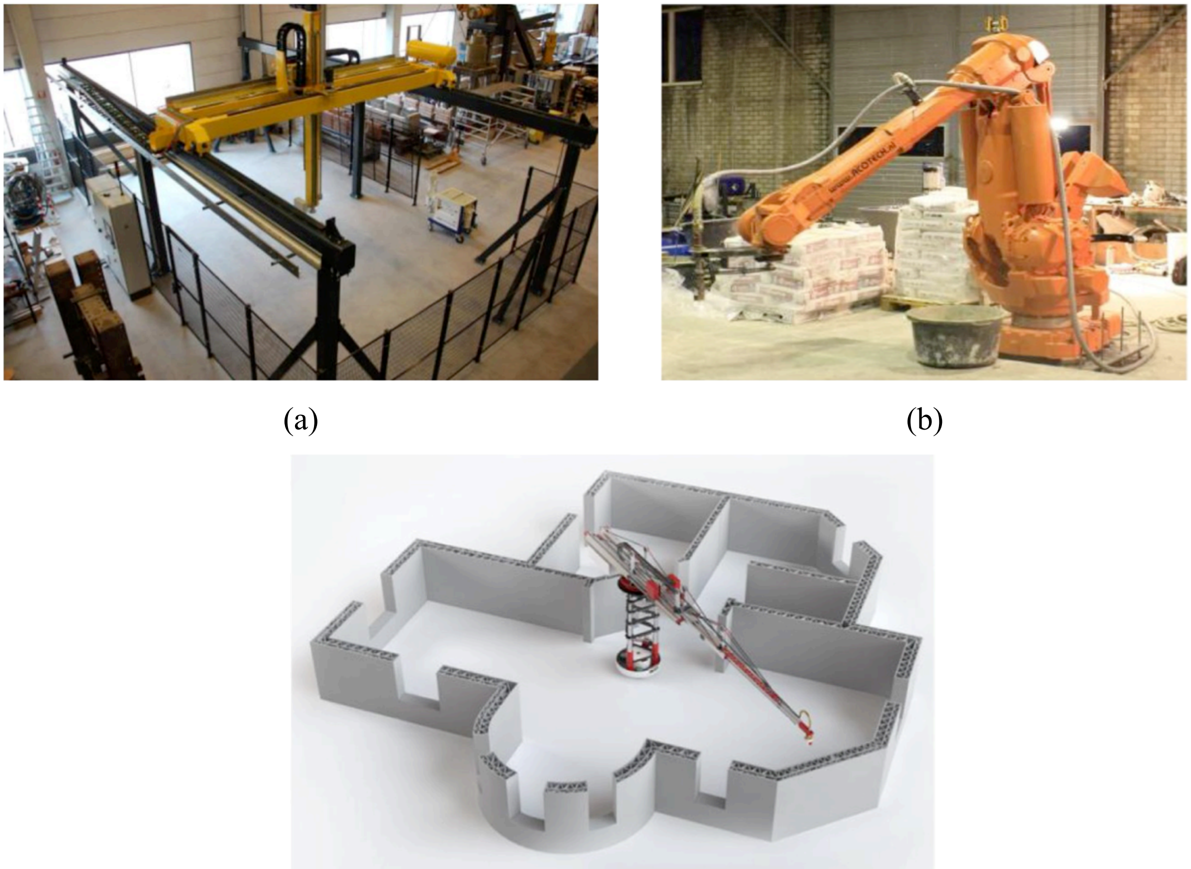

(a) (b)

(c)

Figure 2-2: (a) Four-axis gantry printer, (b) six-axis robotic printer, (c) crane printer [46]

In recent years, 3D concrete printing has seen an increase in adoption across a variety of applications, demonstrating its versatility and potential in the construction industry. Notable examples (illustrated in Figure 2-3) include the construction of Europe's first 3D printed house in 2021, which marked a significant milestone in the field [47]. Moreover, the successful completion of a 3D printed castle showcased the 3DCP technology's capability to handle intricate architectural designs [48]. A multistory 3D-printed home in Houston, USA, exemplified the technology's potential for scalability and efficiency in residential construction [49]. The utilization of 3D printing with ultra-high-performance concrete (UHPC) for manufacturing military and security elements in 2022 further expanded its application range, highlighting its relevance in defense and security sectors [49]. Additionally, NASA's 3D-Printed Habitats Challenge underscored the technology's potential in addressing the unique opportunities of extraterrestrial construction and habitation [50]. These diverse applications emphasize the growing significance of 3D concrete printing in revolutionizing the construction industry.

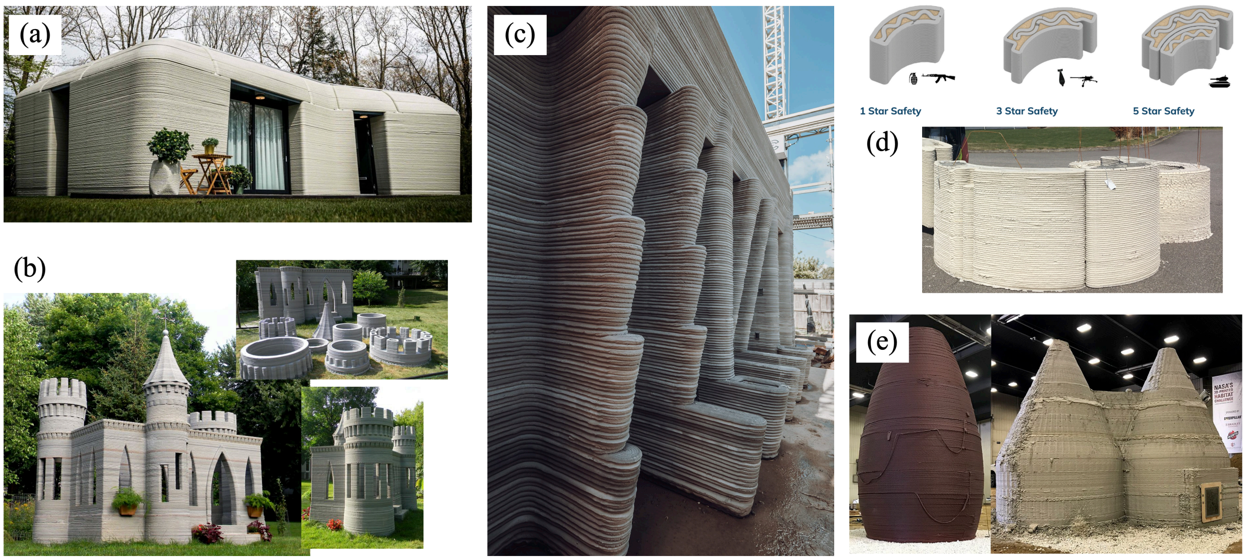

Figure 2-3: (a) Europe's first 3D printed house in 2021, (b) 3D printed castle, (c) a multistory 3D-printed home in Houston, USA, (d) military and security elements manufactured by 3D printing using UHPC, and (e) NASA's 3D-printed habitats challenge

As the adoption of 3D printing technology in the construction sector grows, researchers and practitioners are increasingly focused on understanding and optimizing the rheological and mechanical properties of cementitious mixtures for additive manufacturing [51–53]. This has led to the development of novel cementitious composites that are specifically tailored for 3D printing applications, offering improved performance characteristics such as enhanced strength, durability, and sustainability [54–56]. Moreover, environmental concerns and sustainability have become important considerations in the construction industry. The potential for additive manufacturing to reduce material waste, minimize energy consumption, and lower greenhouse gas emissions has made it an attractive option for sustainable construction [57, 58]. As a result, research in the field of 3DCP is increasingly focused on developing environmentally friendly materials and methods that can contribute to a more sustainable built environment.

2.2. Rheological and Printability Characterization of Cementitious Mixtures

In 3D concrete printing (3DCP), the rheological and printability characteristics of cementitious mixtures play a crucial role in determining the success of the construction process. Conventional construction methods involve casting cementitious mixtures in predefined formworks, where the concrete hardens and assumes the shape of the molds. In contrast, 3DCP demands the cementitious material to be extruded seamlessly from the printer nozzle, retaining its shape upon deposition. This process necessitates a delicate balance between flowability and rigidity, creating a unique set of requirements for 3D printable cementitious mixtures [5, 6].

3D printable cementitious mixtures typically exhibit Bingham visco-plastic behavior, wherein the material acts as a rigid body at low shear stresses but flows as a viscous fluid when subjected to shear stresses exceeding the yield stress [59]. Researchers have identified two distinct yield stresses for 3D printable cementitious mixtures: dynamic yield stress (DYS) and static yield stress (SYS) [3, 60]. These yield stresses are measured using rotational rheological tests and reflect the material's ability to resist deformation before flow and maintain flow, respectively [61]. It is essential for 3D printable cementitious mixtures to possess low dynamic yield stress and plastic viscosity to ensure smooth extrusion, while high static yield stress is required to resist deformation after extrusion [62]. Lu et al. [63] reported that suitable materials for 3DCP should exhibit low plastic viscosity and dynamic yield stress for optimal delivery performance, as well as high static yield stress for enhanced deposition performance. In a separate study, Le et al. [43] found that a relatively low dynamic yield stress, ranging between 0.3 and 0.9 kPa, was ideal for achieving proper extrudability. Furthermore, Panda et al. [64] demonstrated that improved buildability (up to 15 layers) without significant deformation of the bottom layer could be achieved due to an increased static yield stress.

The most common method for determining SYS involves measuring the peak stress when a constant shear rate is applied typically for 60 seconds. de Matos et al. [65] investigated the SYS measurements of cementitious mixtures by different methods. Figure 2-4 illustrates the SYS measurement method in their study. The study revealed that, shear stress initially linearly increases until it reaches a limit value, which is considered the static yield stress. Upon maintaining the shear and breaking the sample structure, the shear stress maintains constant or declines, resulting in a stress overshoot phenomenon [66, 67]. In some cases, a well-defined peak stress may not be observed, however, the maximum shear stress measured is taken as the SYS.

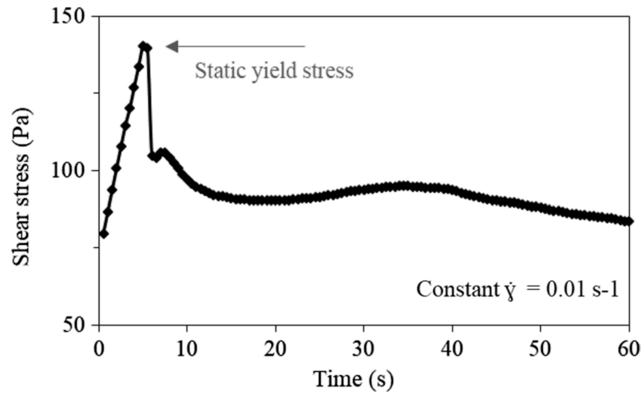

Figure 2-4: Determination of static yield stress [65]

On the other hand, the dynamic properties of the cementitious mixtures are characterized by the Bingham and Herschel-Bulkley models, the most widely used rheological models for characterizing the flow behavior of non-Newtonian fluids. Both models provide valuable insights into the relationship between shear stress and shear rate, allowing for a better understanding of cementitious material's flow properties, workability, and performance in various applications [68, 69]. For example, Chen et al. [70] investigated the yielding behaviors of cement composites using Bingham and Herschel-Bulkley models. The calculation methods of these models are illustrated in Figure 2-5. In particular, the models are fitted on the down curves of a shear rate ascending and descending protocol, where the Bingham model is a linear fit whereas the Hershel-Bulkley model, a modified version of Bingham model, can capture non-linear behavior in the flow curve. The Bingham model describes a linear relationship between shear stress (τ) and shear rate ($\dot{\gamma}$) beyond the DYS. The equation for the Bingham model is as follows:

$$\tau = \tau_o + \eta\dot{\gamma} \tag{1}$$

where τ is the shear stress and $\dot{\gamma}$ is the shear rate. In equation (1), τ_o indicates the intersection point of the Bingham fit line with the y-axis (DYS), and η is the slope of the Bingham fit line (plastic viscosity). This model assumes that the fluid behaves as a rigid body below the yield stress and exhibits linear viscous behavior above the yield stress. On the other hand, the Herschel-Bulkley model is a more general form that encompasses a broader range of flow behaviors, including shear-thinning and shear-thickening. The equation for the Herschel-Bulkley model is:

$$\tau = \tau_o + \eta\dot{\gamma}^n \tag{2}$$

In this equation (2), n is the extra term which is defined as the flow behavior index. The Herschel-Bulkley model accounts for the non-linear relationship between shear stress and shear rate, with n determining the degree of shear thinning (n < 1) or shear thickening (n > 1). When n equals 1, the Herschel-Bulkley model reduces to the Bingham model, highlighting the fact that the Bingham model is a special case of the more general Herschel-Bulkley model. While both the Bingham and Herschel-Bulkley models have been used to describe the flow properties of cementitious mixtures, the Bingham model is more widely employed due to its simplicity and linear relationship between shear stress and shear rate beyond the dynamic yield stress [11, 71–73].

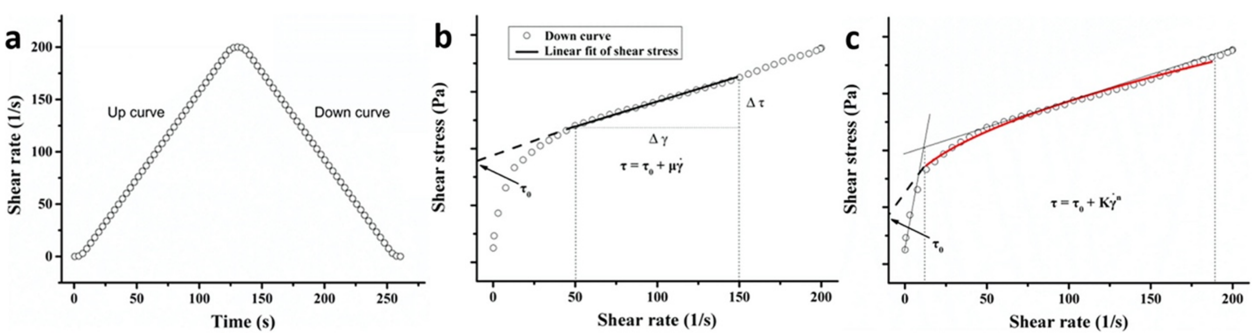

Figure 2-5: Determination of dynamic yield stress and plastic viscosity [70]

Besides rotational test methods, which focus on the yielding behavior of fresh cementitious mixtures, oscillatory test methods provide valuable insights into the visco-elastic behavior of the mixture [64, 74]. Fresh cement, as a concentrated suspension, comprises both elastic and viscous components [75]. Examining the visco-elastic behavior of 3D printable cementitious mixtures is crucial for assessing buildability and stability performance in 3DCP. Recent research has highlighted the importance of Storage Modulus (G'), Loss Modulus (G''), and Linear Viscoelastic Range (LVER) as key parameters for evaluating the buildability and stability performance of 3DCP [76, 77]. Ivanova et al. [78] conducted a study on the prediction of stability failure based on the values of elastic modulus and observed that a higher elastic modulus was required for a 40-layer hollow cylinder to remain stable. In another study, Moeni et al. [79] investigated the temporal variation of the elastic modulus of 3D printable mortar, noting that a high rate of increase in elastic modulus contributed to increased rigidity and elastic properties. They also emphasized the relevance of specific moduli properties, such as shear modulus (G), complex shear modulus (G*), and elastic modulus (G'), in examining the failure mechanism of 3DCP. In their study, they defined a linear visco-elastic domain (LVED), within the critical strain, where the storage modulus (G′) was constant. When the applied strain surpassed the critical strain (LVED), the storage modulus started to decrease which indicated the end of the LVED. Figure 2-6 illustrates results from their study that show the range of LVED.

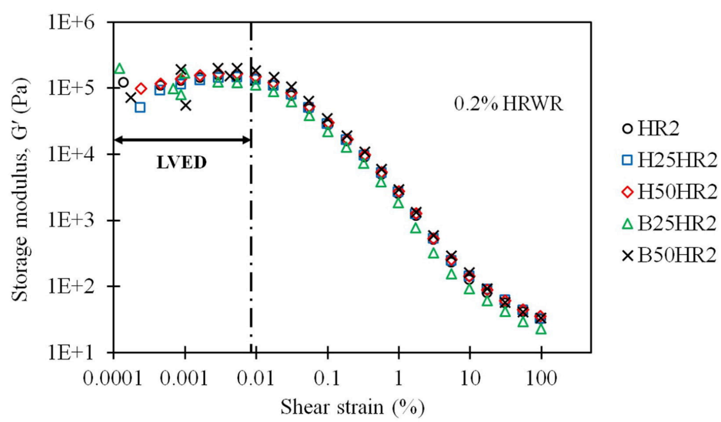

Figure 2-6: Storage modulus results with linear visco-elastic domain (LVED)

Fresh properties of cementitious mixtures play important role in the printability and buildability and can be altered through the use of different additives [80, 81]. Several researchers have explored the effects of various admixtures on the printability characteristics of cementitious composites. Chen et al. [82] explored optimal dosage of viscosity modifying admixture (VMA) to improve printability of limestone and calcined clay based cementitious mixtures. They found the inclusion of VMA at 0.24% of the binder mass results in better shape stability, buildability and green strength. Moeni et al. [79] studied the printability of mixtures with different dosages of high-range-water reducer and nanoclay using various rheological tests. They concluded that the addition of nanoclay improves the thixotropy of cement suspensions. Sikora et al. [83] revealed that the use of nanosilica in printable mortars considerably increases the hydration of the binder phase and yield stress of printable mixtures. Long et al. [11] evaluated the use of microcrystalline cellulose (MCC) for the development of printable mortar mixtures and found that the addition of 1% MCC results in 20% increase in plastic viscosity and 190% increase in yield stress. Wang et al. [84] examined the synergistic effects of a thixotropic superplasticizer and nanoclay on yield stress and green strength of printable mixtures.

2.3. Printability and Buildability Assessment

Shape stability is a crucial factor in determining the buildability and success of 3D printable cementitious composites. It refers to the material's ability to maintain its shape and structural integrity after being extruded from the printer's nozzle and deposited layer by layer during the 3D printing process. More specifically, the printed filament can either fail to retain its shape after extrusion as depicted in Figure 2-7a, or can successively hold its shape after extrusion and maintain its shape while the subsequent layers are being printed as shown in Figure 2-7b. Achieving and maintaining shape stability is essential to avoid deformation, slump, or collapse of the printed structure, which could compromise the final product's performance and aesthetics [85].

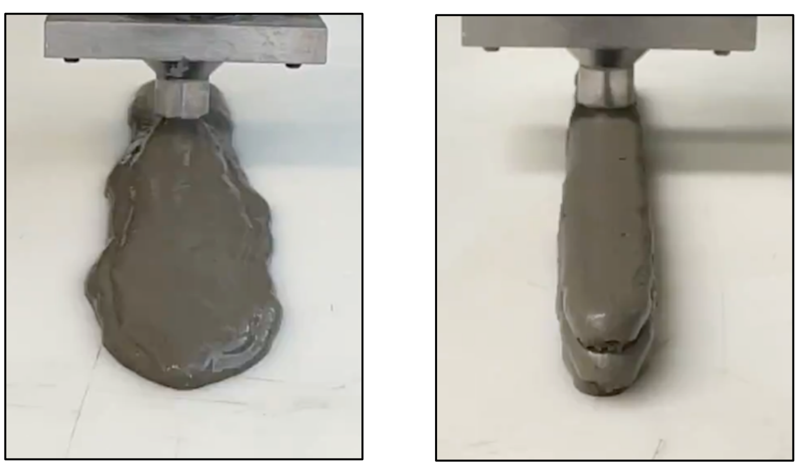

(a) (b)

Figure 2-7: Printed filaments that (a) fail to retain their shape, and (b) retain their shape after being extruded

Several factors influence the shape stability of 3D printable cementitious composites, including rheological properties, material composition and printing parameters [41, 43]. Rheological properties, such as, static yield stress, dynamic yield stress, and plastic viscosity are key rheological properties that significantly impact the shape stability of cementitious composites. High static yield stress helps the material resist deformation and maintain its shape after extrusion, while low dynamic yield stress and plastic viscosity ensure smooth extrusion without clogging or inconsistent material deposition [86]. The choice of cementitious binder, aggregates, and admixtures can also affect the rheological properties, setting time, and strength development of the material, thereby influencing its shape stability. For instance, the use of supplementary cementitious materials, such as fly ash or silica fume, and chemical admixtures like superplasticizers can modify the material's rheology and enhance shape stability [42, 87]. In addition, printing parameters such as print speed, layer height, and nozzle diameter can also impact the shape stability of 3D printable cementitious composites. Optimizing these parameters helps to achieve the desired material deposition and layer adhesion while maintaining the structural stability of the printed object [41]. Researchers continuously explore innovative material formulations and printing techniques to improve the shape stability of 3D printable cementitious composites, thereby enabling the construction of more intricate and complex geometries with enhanced structural performance [43].

Buildability, another crucial aspect of 3D printed cementitious structures, is specifically defined as the maximum height of successfully printed elements before it encounters failure due to yielding or buckling [88–90]. The capacity to extrude and maintain shape stability in layer-wise additively manufactured cement-based components is contingent upon the early-age rheological properties (shear moduli, yield stress, viscosity) of the deposited materials. Specifically, there are three printability phenomena, as illustrated in Figure 2-8, that could occur during the fabrication process: (i) Figure 2-8a demonstrates a successfully printed element prior to experiencing failure due to yielding or buckling, (ii) Figure 2-8b exhibits a plastic yielding (plastic collapse) failure, and (iii) Figure 2-8c presents an elastic buckling failure.

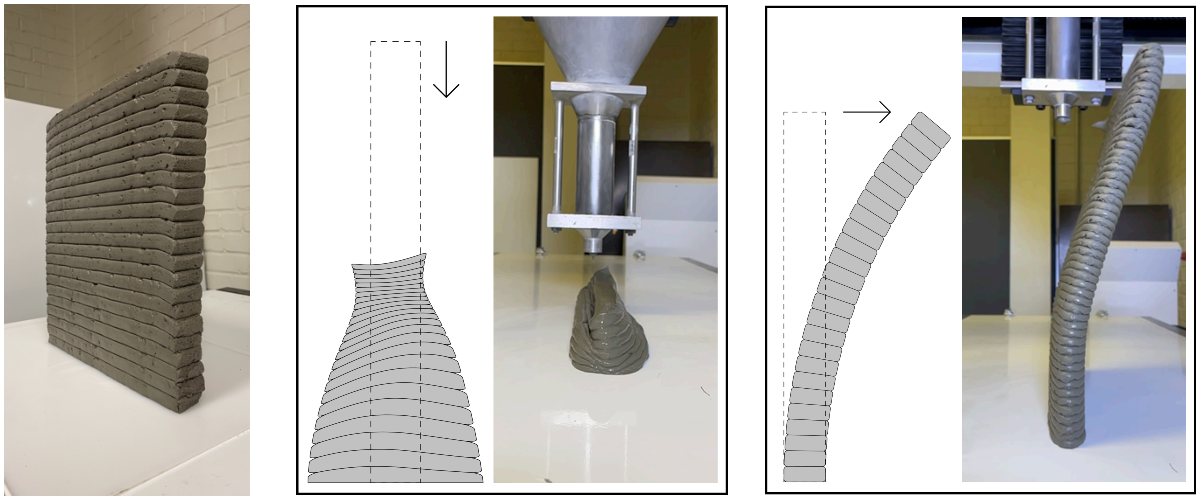

(a) (b) (c)

Figure 2-8: (a) Successfully printed element before it encounters failure due to yielding or buckling, (b) plastic yielding (plastic collapse) failure, and (c) elastic buckling failure

The buildability of 3D printed cementitious composites is significantly influenced by the material's rheological properties, such as static and dynamic yield stress, as well as its viscoelastic properties [46]. For instance, Panda et al. [91] conducted a study on the 3D printability of high-volume fly ash cementitious material and demonstrated the significant impact of yield stress on buildability. As shown in Figure 2-9, the nano-clay modified (NM) mix exhibited considerably greater buildability compared to the control mix (CM), which can be attributed to the high static yield stress and thixotropy of the NM mix. The yield strength of the NM mix was found to be approximately twice as high as that of the CM mix. It is suggested that the yield strength, a crucial fresh property of printable cementitious materials, plays a vital role in determining shape stability and buildability. Similarly, another research has determined that the storage modulus evolution rates, obtained from non-destructive time sweep tests, are more appropriate for describing the structuration of suspensions at rest [79]. In the context of the 3D printing process, this is particularly relevant to the properties of existing bed layers. Moreover, the study found a strong correlation between the storage modulus evolution of the mixtures and the results of printability tests, in terms of both extrudability and shape stability.

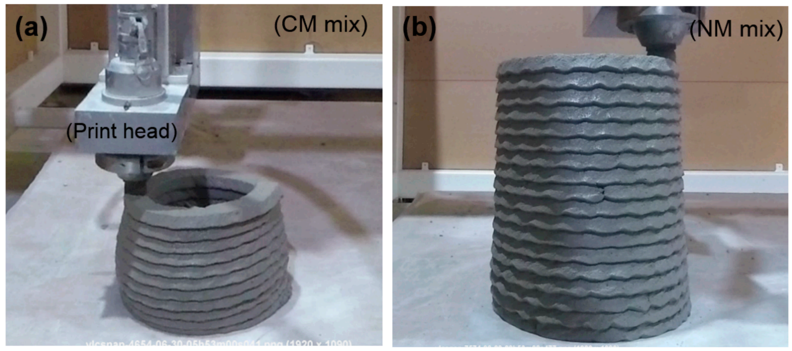

Figure 2-9: Demonstration of 3D printability of (a) control mix (CM), and (b) 0.5% nano-clay modified (NM) mixture

Another study [92], examining the failure of 3D printed cementitious mixtures, found that failure occurred at the 21st and 160th layers for the mixes with 0% (M0) and 0.1% (M0.1) nano-clay percentages, respectively. The mix with 0.3% nano-clay (M0.3), however, did not experience failure and reached the maximum print height limit of 320 layers, approximately 1.6 meters high, achievable by the gantry 3D printer used in the study. As shown in Figure 2-10, the failure mode for the M0 and M0.1 mixes was strength-based, occurring at the bottom-most layers without any significant radial deformations before failure. This observation supports that plastic yielding occurs in the bottom layers which leads to structural collapse.

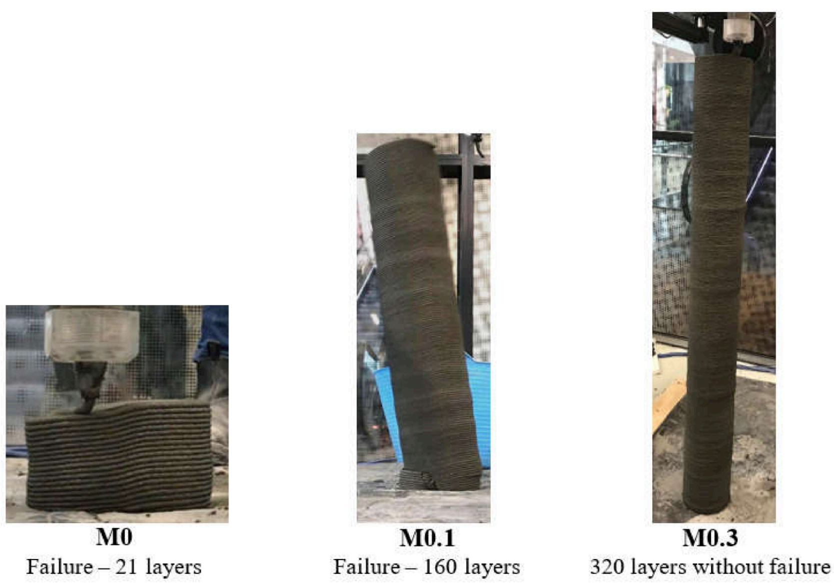

Figure 2-10: Buildability of 3D printed columns

Achieving optimal buildability demands a delicate balance between extrudability and structural stability, ensuring that the material can be smoothly extruded while maintaining its shape under the weight of successive layers [93]. Print parameters such as layer thickness, print speed, and curing conditions can also impact buildability, necessitating careful control and monitoring of the printing process to achieve the desired structural performance [86, 94]. For example, Wolfs et al. [39] reported that optimizing layer thickness and print speed could minimize the risk of structural failure during the printing process. It is worth mentioning that the focus of this dissertation does not include an in-depth examination of these print parameters.

2.4. Nano and Micro-scale Reinforcement for 3D Concrete Printing

Understanding the fresh behavior of cementitious materials for 3DCP has been a major subject of investigation in recent years. Researchers have experimented with various additives and admixtures to modify the fresh properties of cementitious materials, aiming to achieve the desired balance of flowability and rigidity for 3DCP applications. For instance, the incorporation of superplasticizers, retarders, or viscosity-modifying agents can significantly influence the thixotropic properties of cementitious mixtures, optimizing their performance in 3DCP. On the other hand, in recent years, the development of new materials and formulations has expanded the range of 3D printable cementitious mixtures, offering new possibilities for various construction applications. For example, researchers have experimented with incorporating nano and micro scale additives into 3DCP mixtures to enhance their performance in specific contexts, such as increased setting times, reduced environmental impact, or improved durability.

Numerous studies have explored the application of nano-scale and micro-scale reinforcements to enhance the microstructural, rheological, and hardened properties of 3D printed concrete. One such study investigated the use of calcium carbonate nanoparticles (CaCO3) to improve the mechanical performance of 3D printed composites [95]. The researchers found that the flexural and compressive strengths of the geopolymer composites were significantly better compared to those of pure geopolymer. Introducing nanoparticles up to 2.0 wt.% resulted in an improved bonding interface and enhanced cohesion between the binder and various particles.

Another study focused on the impact of nano clay (NC) powder and nano silica (NS) particles on the microstructural characteristics of 3D printed concrete, revealing improved stability as a result of these additives [96]. Additionally, the effects of incorporating carbon nanotubes (CNT) on the fresh and hardened properties of 3D printed mortar ink were studied [97]. The findings demonstrated that the inclusion of 0.1 wt.% CNT led to a 33.6% increase in compressive strength and a 46% increase in flexural strength. However, it was also noted that CNT did not significantly affect buildability, stacking stability, or integrity.

Micro-scale reinforcements have also been the subject of extensive research. For instance, studies have investigated the influence of different types of micro-scaled fibers, such as steel, glass, basalt, and polymeric fibers, on the hardened properties of printable cementitious composites. In one study, the addition of 1 vol.% of steel fibers was found to increase the compressive strength and flexural strength of concrete by 10% and 80%, respectively [98]. Similarly, glass fibers were reported to enhance compressive strength and flexural strength by 3-7% and 25-28%, respectively [99]. Polypropylene (PP) fibers were found to effectively increase the tensile strength of the composite by more than 20% [100].

In summary, the incorporation of nano-scale and micro-scale reinforcements in 3D printed cementitious materials has been demonstrated to improve various properties, including microstructural, rheological, and hardened properties. By optimizing the type and amount of reinforcement, it is possible to achieve superior performance in 3D printed concrete applications.

3. Experimental Methods

3.1. Overview

This chapter explains all the experimental tests and assessments regarding rheological, printability and mechanical characterization in this dissertation. It first presents the rheological test setup and test methods conducted to evaluate fresh properties of cementitious mixtures, accompanied by relevant details regarding the analysis and characterization of the rheological data. Then, it explains the printability and buildability characterization of cementitious mixtures, including the printing process parameters. The chapter then delves into the techniques used to assess hardened properties of cementitious mixtures. In particular, the test setup and methods for compression, tensile, and flexural strength characterization are described. It also includes details about Scanning Electron Microscope (SEM) and Digital Image Correlation (DIC) system that have been used to analyze the mechanical performance of the cementitious mixtures.

3.2. Rheo-viscoelastic Characterization of Cementitious Composites

3.2.1. Rheological Test Setup

Anton Paar MCR 301 rheometer, capable of reading torque values from 1 nNm to 200 mNm, is used for rheological measurements. The rheometer is equipped with a 400 ml capacity building cell (BMC 90) which is a cup with inner serrations to prevent wall slippage and a T-bar stirrer with four blades connected to the coupling of the rheometer. Once the mixture is ready, it is placed in the building cell and the torque measurements are performed with counterclockwise rotation of the stirrer for rotational measurements and oscillated with a constant frequency for oscillatory measurements. Note that the building cell has an inset cage on the inner wall of the cell to prevent slippage of the material while the shear force is being applied. The shearing is established between the blades of the stirrer and the inner wall of the building cell which corresponds to 20 mm. Due to the hydration of the cement in the mixes, the timing of the tests is regarded as the crucial factor for the accuracy and reproducibility of the measurements. Thus, a great care is taken to place the mortar samples into the building cell and start the rheological measurements immediately after the mixer is stopped. For all the mortar samples, the time passed between the end of the mixing and the start of the rheological measurement is adjusted as 1 min to ensure consistency. The rheometer and rheological test setup are shown in Figure 3-1a along with schematic representation and the geometry of the T-bar stirrer vane and building cell in Figure 3-1b.

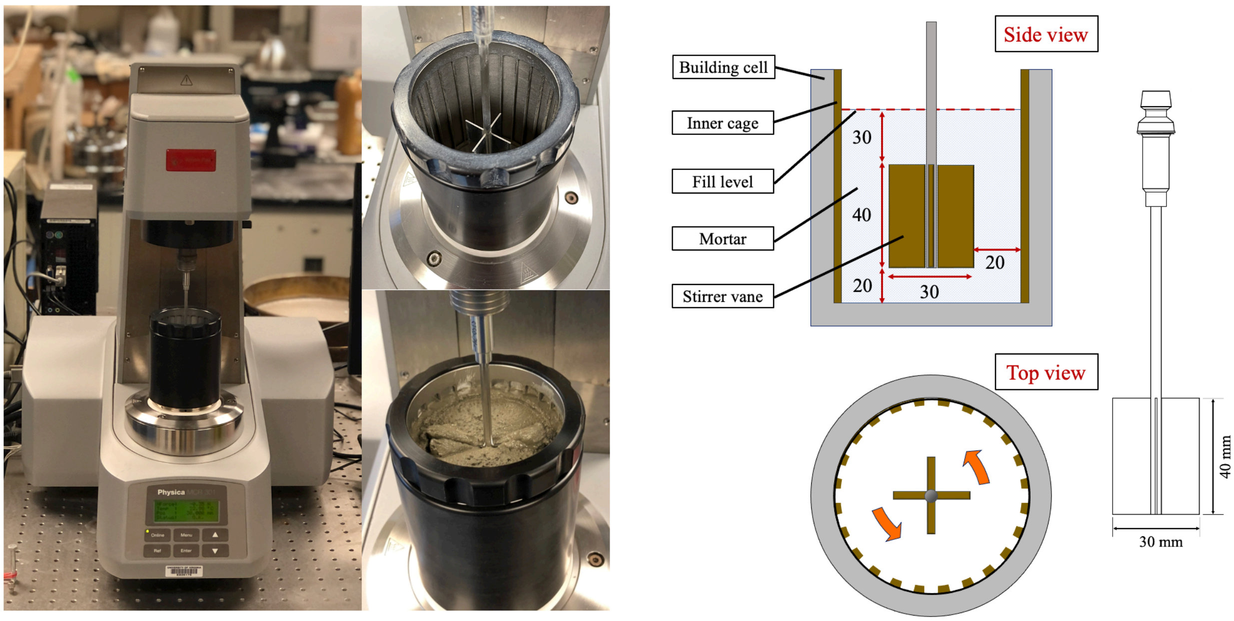

Figure 3-1: (a) Rheometer and the test setup with freshly poured mortar in the building cell, and (b) schematic representations of T-bar stirrer vane and building cell (all dimensions are in mm)

3.2.2. Stress Growth Test

To examine the rheo-viscoelastic behavior of 3D printable mortar mixtures, three consecutive rheological tests are conducted; stress growth test, ramp test, and amplitude sweep test. The stress growth test is performed by applying a constant shear rate of 0.1 s^{-1} for 60 s, and the rheometer records the shear stress response of the mortar mix. The stress growth test protocol and a typical result of this test from one of the mixes are shown in Figure 3-2a and b, respectively. During the stress growth test, the shear stress of the mix increases progressively to a maximum level, and the peak shear stress value is recorded as the static yield stress (SYS) of the mix [65, 70], as shown in red lines in Figure 3-2b. The SYS is an important material property that affects the structural build-up and stability of 3D printable concrete. SYS is the critical shear stress level that maintains the well-connected undisturbed microstructure of the mortar mix such that the material behaves elastically [60]. Conversely, if the applied shear stress is greater than the SYS, the microstructure of the mixture is broken, and the material behaves like a viscous liquid, which starts to flow and leads to failure in the stability of the structure. SYS plays a vital role in the stability of the structure after printing.

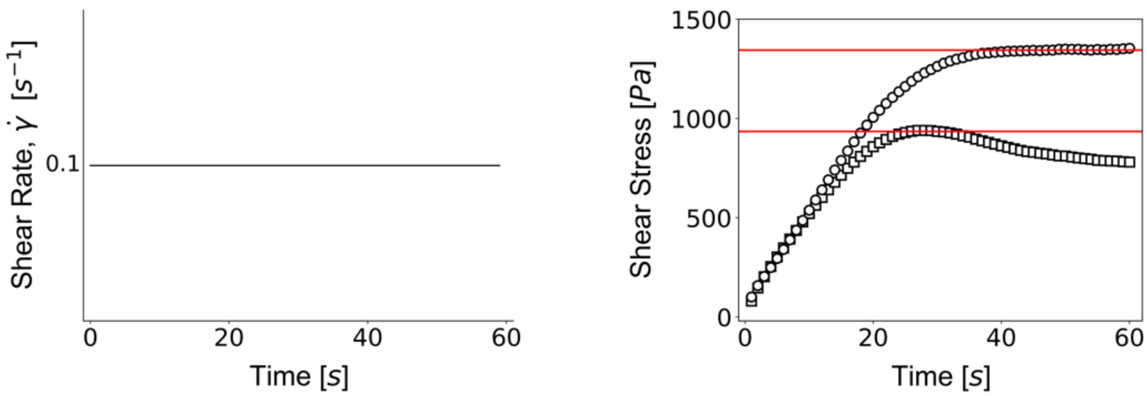

(a) (b)

Figure 3-2: (a) Stress growth test protocol, (b) typical example from stress growth test

3.2.3. Ramp Test

The ramp test is performed to determine the dynamic yield stress (DYS) and plastic viscosity (η) using the flow curves from the ramp test. During the ramp test, the shear rate is progressively increased from 0 s^{-1} to 100 s^{-1} in 30 s (ramp-up), and subsequently decreased from 100 s^{-1} to 0 s^{-1} in 30 s (ramp-down). The test protocol for ramp test is shown in Figure 3-3a. The Bingham visco-plastic material model is used to calculate DYS and plastic viscosity. In particular, the Bingham model fits a linear regression model on the higher shear rate region of the ramp-down curve (from 100 s^{-1} to 40 s^{-1}) as illustrated in Figure 3-3b, and DYS and plastic viscosity are calculated using the Bingham model equation:

$$\tau = \tau_o + \eta\dot{\gamma} \tag{1}$$

where τ is the shear stress, and $\dot{\gamma}$ is the shear rate. In this equation, DYS corresponds to the intersection point of the Bingham fit with the y-axis (shear stress), and plastic viscosity is the slope of the Bingham fit line. DYS and plastic viscosity are critical material properties studied to understand the pumpability and extrudability of the 3DCP [72]. DYS is defined as the minimum amount of stress required to maintain the flow of material after initiation, while plastic viscosity is considered as the resistance to flow [63, 101]. Therefore, a relatively low DYS and viscosity are necessary for a smooth, continuous, and uninterrupted extrusion of the mortar.

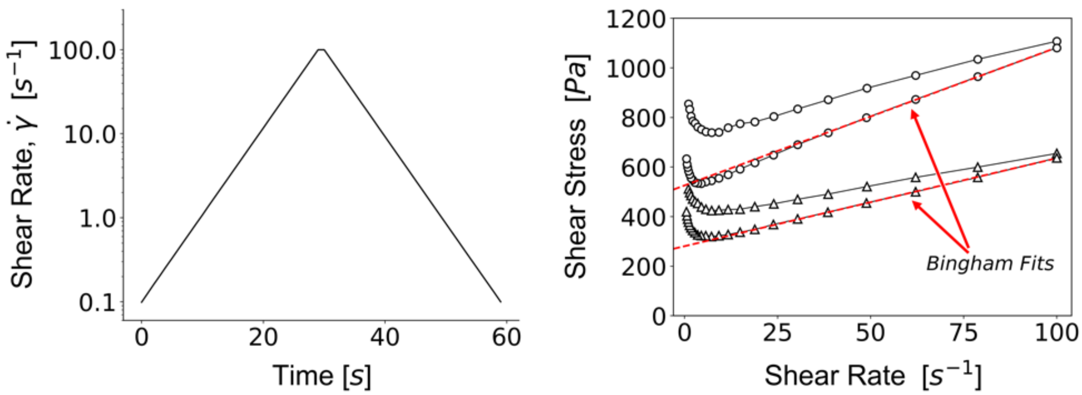

(a) (b)

Figure 3-3: (a) Ramp test protocol, and (b) typical example from ramp test

3.2.4. Amplitude Sweep Test

Another test conducted to investigate the effect of additives on the rheo-viscoelastic behavior of mortar mixtures for 3DCP is the amplitude sweep test. During this oscillatory test, the shear strain is gradually increased from 0.01% to 100% over a period of 400 s, while the angular frequency (ω) is held constant at 10 s^{-1} (as shown in Figure 3-4e). The material behaves as elastic up to a critical strain, which is referred to as the linear viscoelastic range (LVER) [102]. Within this range, the elastic energy is stored in the material, reflecting the strength of the microstructural bonds between the particles, as represented by the storage modulus [103, 104]. Beyond the LVER, energy dissipation occurs due to the applied shear, reflecting the viscous component of the mixture [105]. The storage modulus remains constant within the LVER, providing a quantitative measurement of the elastic component of the material. The LVER is defined as the shear strain corresponding to a 5% downward convergence from the initial constant storage modulus value, and storage modulus values are calculated at this point [106].

It is worth noting that a pre-shearing cycle was applied between the stress growth test, ramp test, and amplitude sweep test to eliminate any residual strains and create a consistent environment for all the mixtures. The pre-shearing cycle involved increasing the shear rate from 0 s^{-1} to 100 s^{-1} in 10 s, holding it at 100 s^{-1} for 10 s, and subsequently decreasing it from 100 s^{-1} to 0 s^{-1} in 10 s. After each pre-shearing cycle, the material is rested for 5 s before the subsequent test starts.

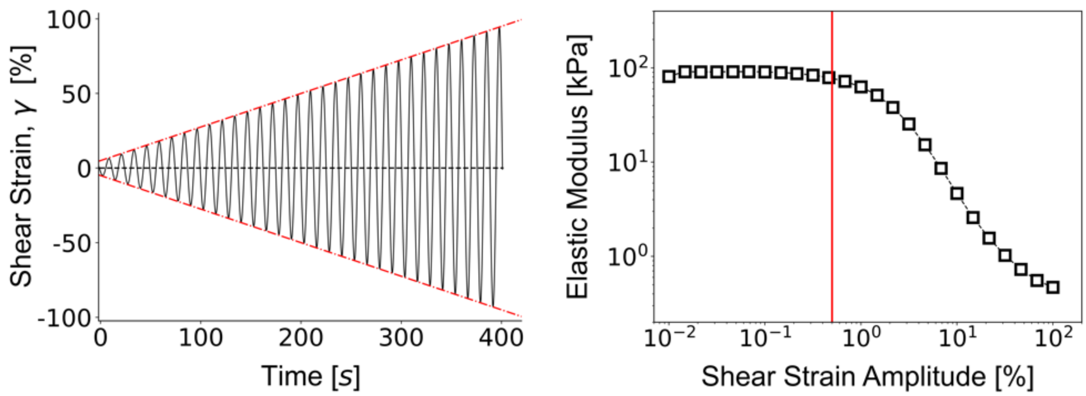

(a) (b)

Figure 3-4: (a) Amplitude sweep test protocol, (b) typical example from amplitude sweep test

3.3. Printability and Buildability Characterization of Cementitious Mixtures

A 3D printer with a screw pumping mechanism (Figure 3-5) is used for printability and buildability measurements of the most promising mortar mixtures. Two different extrusion types are performed: vertical extrusion and horizontal extrusion. Vertical extrusion is performed for buildability assessment and extrusion is done through a 15 mm diameter circular nozzle where the height of each layer is set to be one half of the nozzle diameter (i.e., 7.5 mm). Buildability of the structure is quantified as the maximum number of printable layers before failure by printing a single-line wall of a target structure. The target structure is selected to be a single wall of a common residential building which is described in the "Guide to Residential Concrete Construction" [107]. The dimensions of the target structure are provided from the description of the geometry of walls in the ACI guide. A wall height of 2.5 m (8 feet) has been the most common wall height that coincides with the manufacturing module of most building products. The wall thickness is recommended to be in the range of 200 and 250 mm (8 and 10 in) with little or no reinforcement. For this study, the wall thickness is set as 250 mm and with 2500 mm of the total wall height. The aspect ratio of the target wall (A) is calculated as the ratio of the total height and breadth of the wall and given as 2500/250 = 10. The selected mixes are printed until failure and the maximum number of experimentally printed layers before failure is reported in the results section. Also, the failure modes of the structures are analyzed through recorded videos while printing. For horizontal extrusion, a rectangular nozzle with a breadth of 20 mm and height of 10 mm is used for mechanical test specimen preparation.

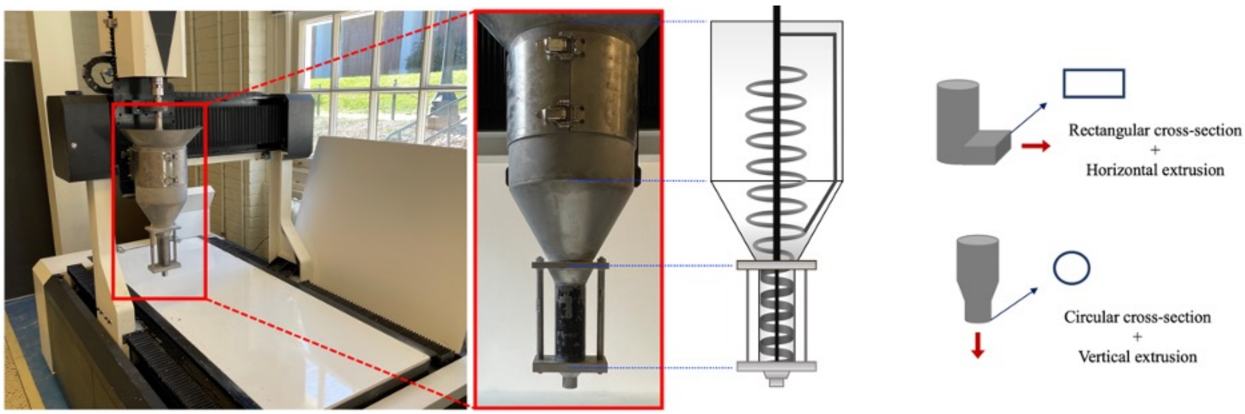

Figure 3-5: 3D printer with the schematic representation of screw pumping mechanism and nozzles

3.4. Mechanical Characterization of Cementitious Composites

3.4.1. Direct Tensile Tests

Following the guidelines set by the Japan Society of Civil Engineers (JSCE), uniaxial tensile tests were performed on dog-bone shaped samples to evaluate the tensile properties of ECC materials [106]. Three dog-bone shaped samples for each mix design were subjected to uniaxial tension after a 28-day curing period. The tensile test setup and the specific dimensions of the dog-bone shaped specimens can be found in Figure 3-6. A 100-kN capacity servo-hydraulic MTS machine was employed for the tensile tests, which were conducted under displacement control at a steady loading rate of 0.5 mm/min. As depicted in Figure 3-6, a laser extensometer was employed to accurately monitor the displacements during tensile tests. To facilitate these measurements, two silver tapes were applied to the gauge length of the test coupons, ensuring precise tracking of the displacements throughout the testing process. Additionally, a Digital Image Correlation (DIC) system was employed, only for the cementitious composites with micro scale fibers, to monitor the strain behavior during the tests. To facilitate DIC measurements, the surfaces of the test specimens were first painted in white color and then adorned with a random speckle pattern, as demonstrated in Figure 3-6. DIC is a non-contact, real-time optical system that captures sequential images for full-field deformation analysis, effectively tracking and correlating strain patterns to discern deformation behavior.

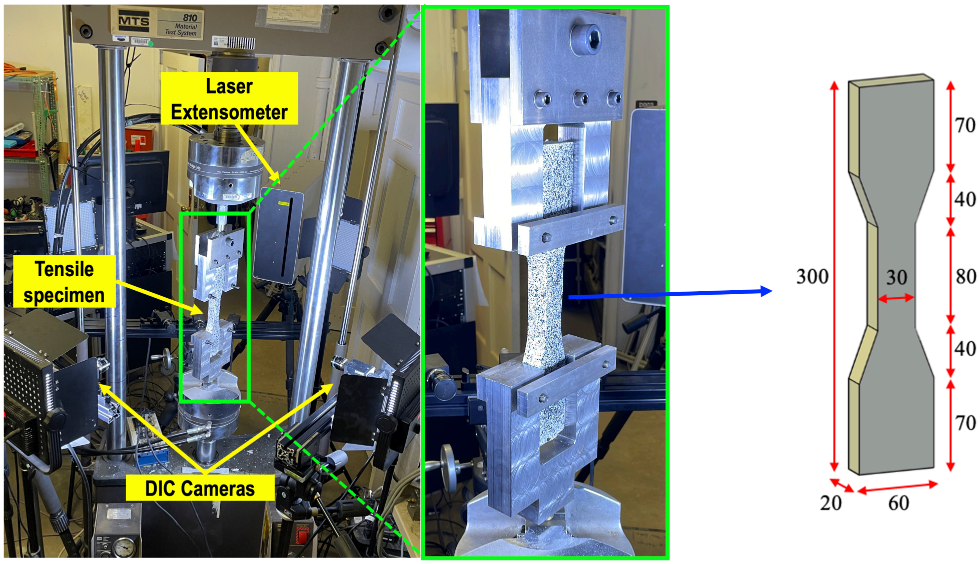

Figure 3-6: Tensile test setup and dog-bone shaped tensile coupon dimensions (dimensions are in mm)

3.4.2. Flexural Strength Tests

Four-point bending tests were conducted on prismatic specimens, with two distinct types of prismatic samples fabricated. For the nanoscale-reinforced composites, the prism dimensions were 40 x 40 x 160 mm, adhering to the ASTM C348 standard. In contrast, the microscale-reinforced composites followed ASTM C 1609, with dimensions of 40 x 80 x 300 mm. The span lengths for both types of specimens are illustrated in Figure 3-7. A loading rate of 0.075 mm/min was utilized during the tests. Throughout the four-point bending test, the load frame recorded the applied load, while the laser extensometer measured the mid-span beam net deflections. The same DIC system was employed to monitor the full field deformation as illustrated in Figure 3-8. For each mix design, three specimens were fabricated and tested after a 28-day curing period.

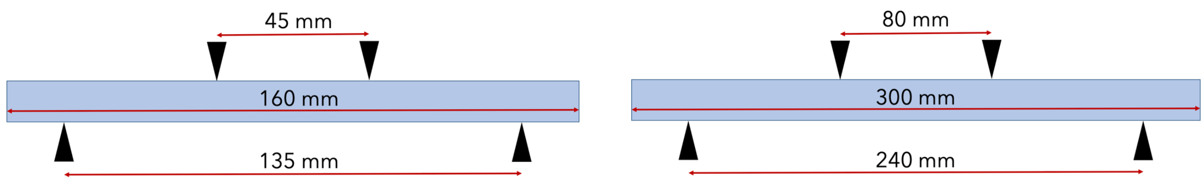

(a) (b)

Figure 3-7: Span lengths of the (a) nanoscale, and (b) microscale reinforced specimens

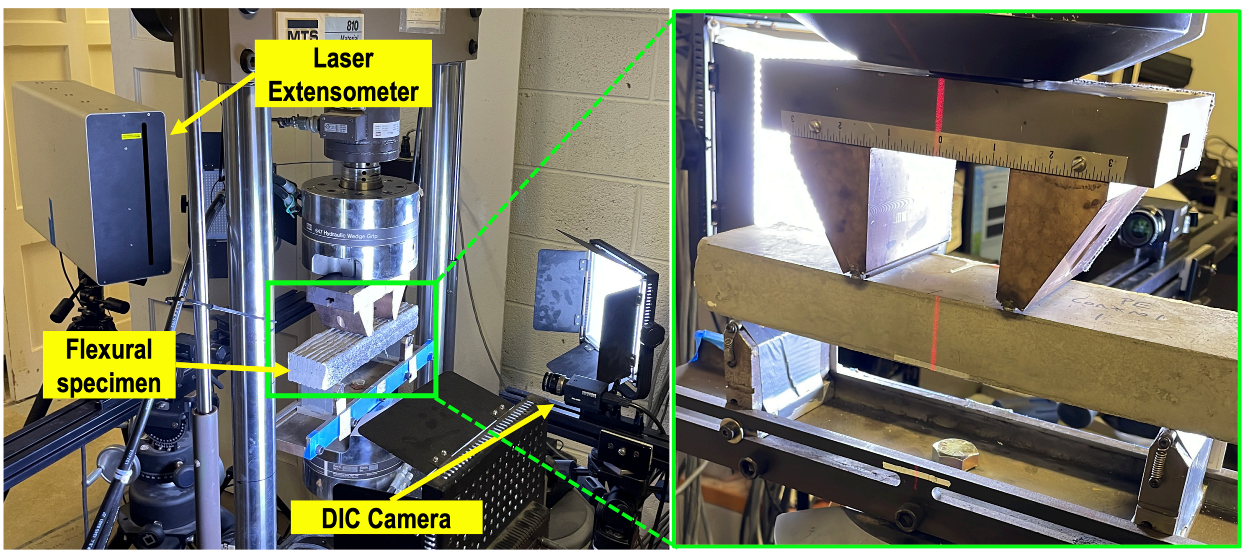

Figure 3-8: Flexural test setup

3.4.3. Compressive Strength Tests

Upon completion of a 28-day curing period, the compressive strength of the mortar samples was determined in accordance with ASTM C 109 standard. Three cubic samples, each measuring 50 × 50 × 50 mm, were assessed for each mixture. A hydraulic pressure-based compressive strength test was performed at a loading rate of 0.25 MPa/s.

4. Effects of VMA and ANC on Rheo-viscoelastic Properties and Printability Characteristics of Cementitious Composites

4.1. Overview

This section explores the effects of a viscosity modifying admixture (VMA) and attapulgite nanoclay (ANC) on rheological and viscoelastic properties as well as printability characteristics of mortar mixtures used for 3D printing. A total of sixteen mortar mixtures with varying dosages of VMA and ANC are prepared using a factorial design of experiments. Rheological properties of each mixture including static yield stress, plastic viscosity, and dynamic yield stress are evaluated through rotational rheological tests such as ramp test and stress growth test. Then, the viscoelastic properties such as storage modulus, loss modulus and linear viscoelastic range are determined using oscillatory rheology tests. A thermogravimetric analysis (TGA) is conducted to assess the effects of VMA and ANC on hydration characteristics of mortar mixtures. A statistical analysis is performed to further evaluate the individual and joint effects of VMA and ANC on key performance parameters. An unsupervised clustering algorithm is used to group the mixtures into three clusters based on the obtained rheological and viscoelastic properties. A direct printing test using a screw type 3D concrete printing is conducted to assess the printability and buildability of the mortar mixtures selected from each cluster.

4.2. Materials and Mixture Preparation

Ordinary Portland cement type I/II, calcium sulfoaluminate (CSA) cement, non-crystalline silica fume (SF) and class F fly ash (FA) are used as the binder of the mortar mixes. CSA cement offers rapid setting and high early strength, which helps shape retention and buildability of printable mixtures. Fly ash and silica fume are used as supplementary cementitious materials. To reduce the potential cracking and drying shrinkage, a shrinkage reducing expansive agent (EA) is added to the mixes. Industrial quartzite sand with a particle size distribution ranging from 0.15 mm to 0.60 mm is used as fine aggregate. Water to binder ratio (w/b) is kept at 0.37 and a high efficiency polycarboxylate based superplasticizer (SP) is used to increase the workability of the mortar mixes without any segregation. Proportions of these materials are shown in Table 4-1 as weight percentages of binder and kept constant for all mortar mixes. A viscosity modifying admixture (VMA), which is carbohydrate complex chemical-based admixture, and attapulgite nano-clay (ANC), are added in the mixes at varying ratios. Table 4-2 shows chemical composition and physical properties of all binder as well as ANC used in this study.

Table 4-1: Mix proportions (by weight of binder)

Binder				Silica Sand	Water	EA	SP
OPC	CSA	SF	FA				
0.68	0.05	0.05	0.22	0.52	0.37	0.03	0.012

Table 4-2: Chemical composition and physical properties of OPC, CSA, SF, FA, and ANC

[%]	OPC	CSA	SF	FA	ANC
SiO_2	22.9	6 – 10	88 – 90	50.8	55.20
Al_2O_3	4.9	20–24	0.6	26.9	12.20
Fe_2O_3	2.6	1–4	0.5	12.1	4.05
CaO	64.8	41 – 45	2 – 5	2.0	1.98
MgO	3.52	0.5 – 1.0	-	0.9	8.56
SO_3	-	18 – 25	-	0.33	-
TiO_2	0.2	-	0.05	-	0.49
K_2O	0.8	0.1 – 0.3	-	2.3	0.68
Na_2O	0.2	0.1 – 0.3	-	2.35	0.53
ZrO_2	-	-	5 – 7	-	-
LOI	2.5	-	-	2.32	-
Physical Properties:					
Specific Gravity (g/cm^3)	3.15-3.25	2.9	0.8	2.35	2.287
Fineness (mm)	0.045	0.025	0.045	0.035	0.03

To study the effects of the VMA and ANC on the rheological properties of the mortar mixtures, experiments are designed with factorial design (n^k) approach, where n represents the number of levels and k represents the number of factors. The VMA and ANC are considered to be the two factors ($k = 2$) and four levels for each factor ($n = 4$) are selected as shown in Table 4-3 to analyze the main effects and the interaction effects of the factors on the response variables.

Table 4-3: Factors and levels of experimental design

	Factors	
Levels	VMA/b	ANC/b
1	0.0%	0.0%
2	0.1%	0.2%
3	0.2%	0.4%
4	0.3%	0.6%

A total of sixteen mixes are prepared in the full design using the factors and the levels listed in Table 4-3. Table 4-4 shows the full factorial design of experiments for sixteen mixtures. Three samples for each mixture are prepared for the rheological measurements. To mix the mortar samples, a 20-quart capacity Hobart planetary floor mixer is used. First, the binders, expansive agent and sand are dry mixed for 5 min at 100 rpm until a homogenous mix is obtained. Then, 80 wt.% of the mixing water with dissolved SP is added to the mixture and initially mixed for 1 min. The mixer is stopped for 30 s after 1 min of initial mix to scrap down the bowl to re-mix the unmixed parts that may stuck on the sides or the bottom of the mixing bowl. Next, another 2 min of mixing is applied at 200 rpm. Then, 10 wt.% of the mixing water with dissolved VMA is added to the system and mixed for 2 min at 200 rpm. Finally, 10 wt.% of the remaining mixing water with dissolved ANC is added into the mixture and mixed for another 2 min at 200 rpm. Note that the ANC is first mixed in the water using a high shear mixer for 3 min at 5000 rpm prior to its addition to the mortar mixture. This step is a critical step in the process of creating a colloidal form of the material, where the ANC particles do not settle or separate over time. With the intense shear forces from high shear mixer, ANC agglomerates are broken down and uniformly dispersed in the liquid medium.

Table 4-4: Full factorial design for 16 mixes with the two factors and four levels

	ANC/b			
VMA/b	0 %	0.2 %	0.4 %	0.6 %
0 %	Mix 1	Mix 2	Mix 3	Mix 4
0.1 %	Mix 5	Mix 6	Mix 7	Mix 8
0.2 %	Mix 9	Mix 10	Mix 11	Mix 12
0.3 %	Mix 13	Mix 14	Mix 15	Mix 16

4.3. Rheo-viscoelastic Properties

4.3.1. Static Yield Stress (SYS)

Figure 4-1 a and b illustrate the stress-growth test results for the mixtures with increasing amount of VMA (0% ANC) and increasing amount of ANC (0% VMA), respectively. In these plots, the evolution of shear stress with time is plotted as the mean value of the results of three specimens. With the addition of VMA or ANC, shear stress increases rapidly during each test and then remains almost constant. Using the mean shear stress–time curve, the static yield stress (SYS) for each mixture was calculated as described earlier. The SYS of mix 1 is calculated as 86 Pa. Similar to the DYS results, ANC is observed to be more effective on improving the SYS than VMA. Keeping the ANC content at 0% and increasing the VMA content to 0.3% increased the SYS to 641 Pa. On the other hand, the SYS of the mix with 0.6% ANC and 0% VMA was measured as 2175 Pa.

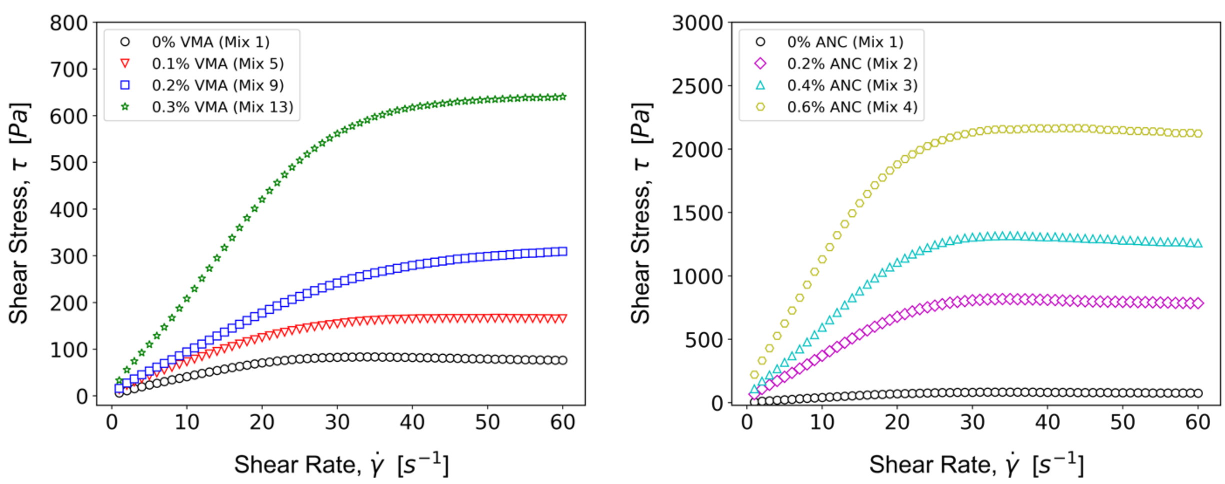

(a) (b)

Figure 4-1: Stress-growth curves for specimens with varying amounts of (a) VMA and (b) ANC

To better visualize the effects of VMA and ANC, the variation of the SYS with respect to VMA and ANC is shown in Figure 4-2. The linear regression model fits with corresponding R^2 are also provided on the plots. It is shown in Figure 4-2a that the SYS generally increases with increasing VMA content for every level of ANC ratio. The most consistent increase is observed for the mixes with 0% ANC and increasing content of VMA, for which an R^2 of 0.91 is calculated. The slopes of the dashed lines in Figure 4-2a indicates that similar improvements are observed for other levels of ANC/b. However, greater variations in static yield stress with VMA ratio are observed when the ANC is also added to the mixtures. In particular, increasing the ANC content from 0% to 0.6% decreased the R2 from 0.91 to 0.41. This suggests that the increased content of ANC in the mixes decreases the significance of VMA on the static yield stress. This phenomenon can be attributed to the higher heats of hydrations due to ANC's role as additional nucleation sites in the matrix [108]. As a result, the hydration process is dominated by the ANC which in return decreases the significance of VMA in the mixtures. The variation of SYS with ANC content is shown in Figure 4-2b. The steeper slopes indicate that the ANC addition increases the SYS more effectively than the VMA addition. In addition, the R^2's in Figure 4-2b suggests that the correlation between the SYS and ANC ratios is considerably high for all levels of VMA content. The smallest R^2 is calculated as 0.97, which suggests a strong correlation between the SYS and ANC ratio.

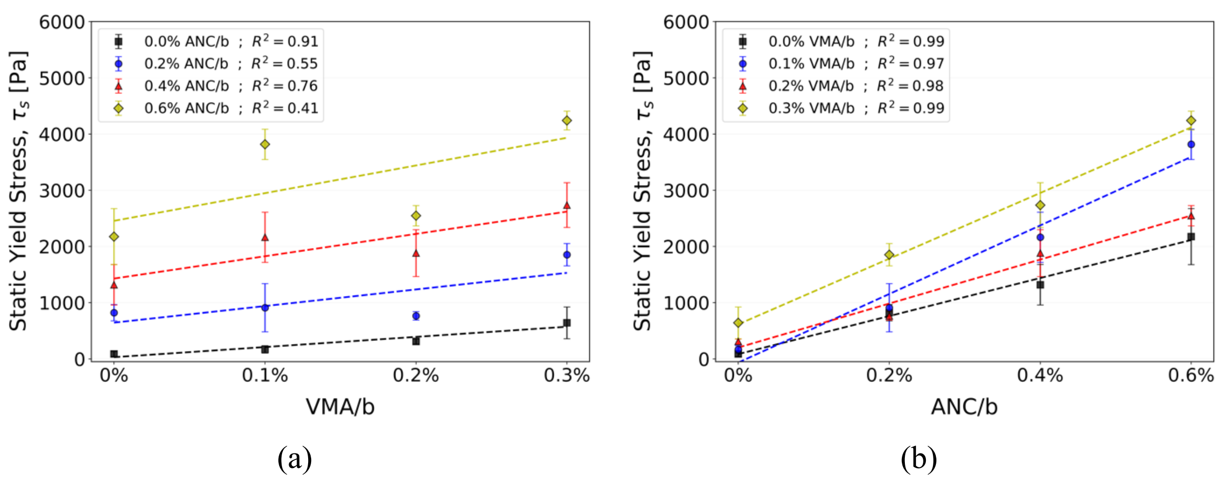

Figure 4-2: Variation of static yield stress with (a) VMA and (b) ANC ratios

4.3.2. Dynamic Yield Stress (DYS) and Plastic Viscosity

The flow curves and Bingham fits obtained from the ramp test are shown in Figure 4-3 for the specimens with 0% ANC and varying percentages of VMA. It is clear from Figure 4-3 that the increasing VMA content increases the DYS since the initial stress readings increase. It also increases the plastic viscosity as the slopes of the Bingham fits increase. The increase in the DYS and viscosity can be attributed to (i) increasing the viscosity of the interstitial fluid, (ii) forming a bridging effect between the cement particles, and (iii) creating a polymer-polymer interaction via entanglement and association [109]. Figure 4-4a shows the flow curves obtained from Bingham model for the specimens with varying amounts of ANC where no VMA is added to the mixtures. Dynamic yield stress considerably increases with increasing amounts of ANC. It increases from 10 MPa to 485 MPa when 0.6% ANC is added to the base mixture.

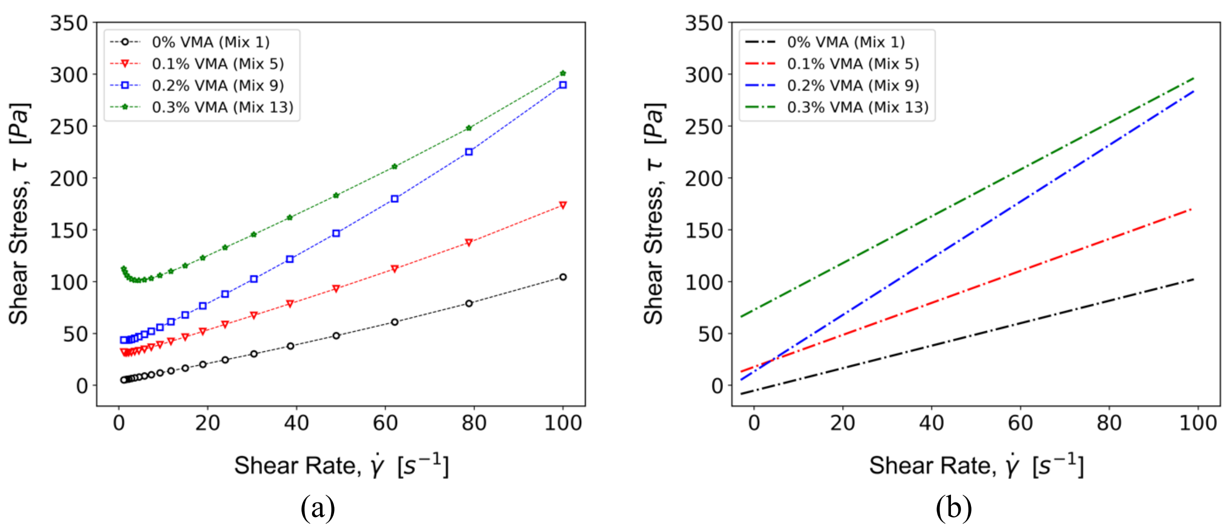

Figure 4-3: (a) Flow curves and (b) Bingham model fits on flow curves for specimens with no ANC and varying percentages of VMA

It has been shown that ANC is effective to produce a denser microstructure in cement pastes and mortars by the electrical attraction forces generated from the oppositely charged edges of the particles [110, 111]. Particularly, ANC particles carry positive charges on the edges and negative charges on the faces [112], and the oppositely charged points of the particles tend to associate with each other, thereby improves the viscosity of the mortar mix. Also, incorporation of ANC forms Vander Waals bonding within the mixture by filling the gaps between binder components. On the other hand, there is no significant change in the slopes of the fitting curves, indicating minimal effect of the ANC on the plastic viscosity of mixtures when no VMA is present. When Figure 4-3a and Figure 4-4a are compared, it can be seen that the addition of VMA both widens and shifts the curves upward, while the ANC mainly causes a strong upward shift in the hysteresis curves due to increase in the flocculation strength with the ANC addition.

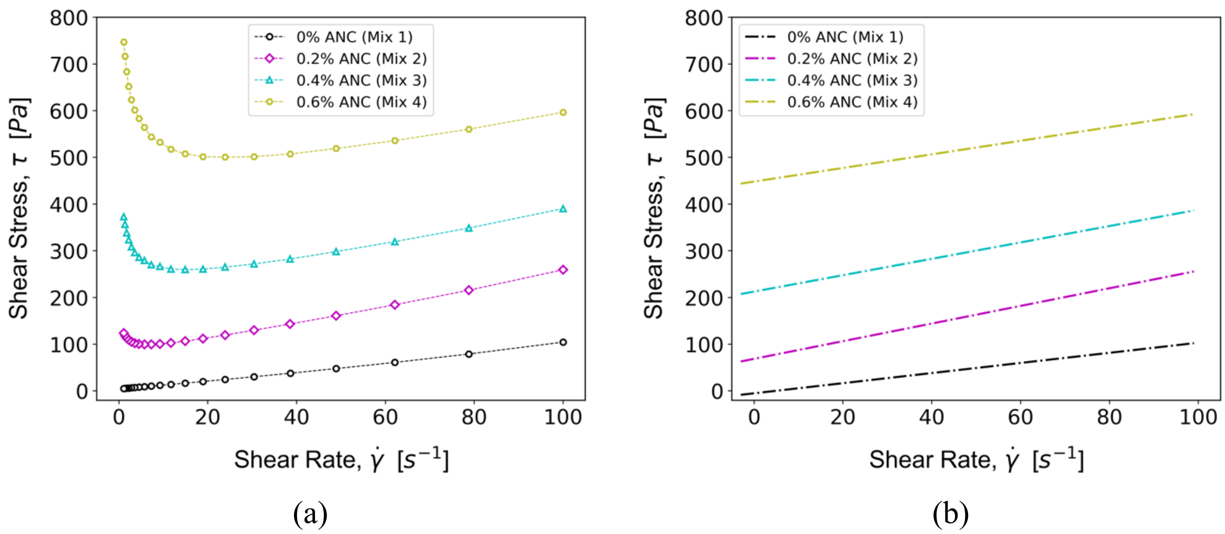

Figure 4-4: (a) Flow curves and (b) Bingham model fits on the flow curves for specimens with no VMA and varying percentages of ANC

Figure 4-5a shows the variation of DYS with respect to the VMA ratio for the specimens for a constant amount of ANC. Similarly, Figure 4-5b shows the same variation with respect to the ANC ratio for specimens with a constant VMA ratio. The coefficient of determination (R^2) is shown in each plot. Although both the VMA and ANC increase the DYS, a higher correlation between DYS and ANC is observed. The addition of ANC to the mixtures with different VMA ratios consistently and almost linearly increases the DYS. It can be also seen from Figure 4-5b that the correlation and rate of this increase are higher when the VMA also exists in the mixtures compared to the mixtures with only ANC.

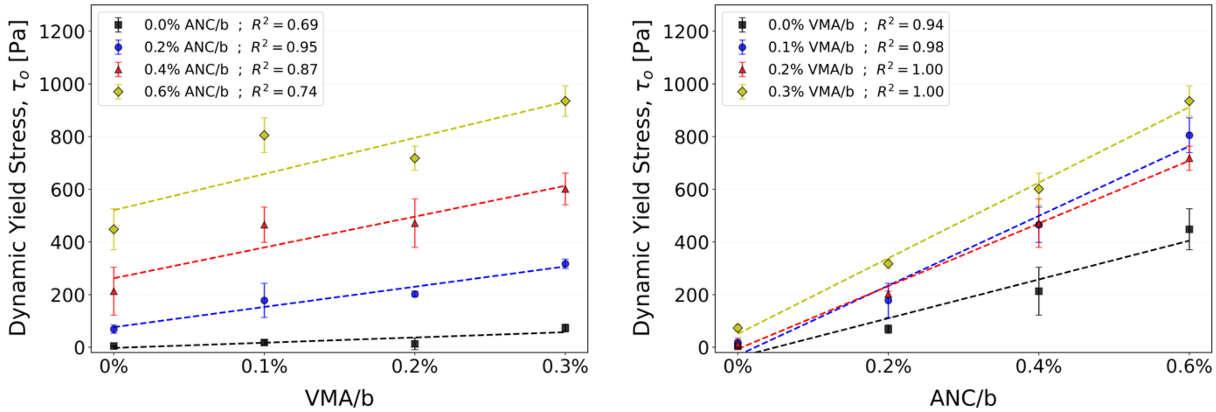

(a) (b)

Figure 4-5: Variation of dynamic yield stress with (a) VMA and (b) ANC ratios

Figure 4-6a and b show the variation of plastic viscosity with respect to the VMA and ANC ratios, respectively. Unlike the DYS, no clear pattern is observed for the effect of the VMA and ANC on plastic viscosity. Therefore, no regression lines are shown in these plots for clarity purposes. Nevertheless, plastic viscosity tends to increase with the addition of VMA, especially when there is no ANC in the mixture. On the other hand, the addition of ANC to the mixtures with relatively high VMA ratios (0.2% and 0.3%) gradually decreases plastic viscosity. The minimum plastic viscosity is measured as 351 kPa.s with 0.6% ANC/b and 0.1% VMA/b, whereas, the maximum plastic viscosity is measured as 2361 kPa.s with 0% ANC/b and 0.2% VMA/b.

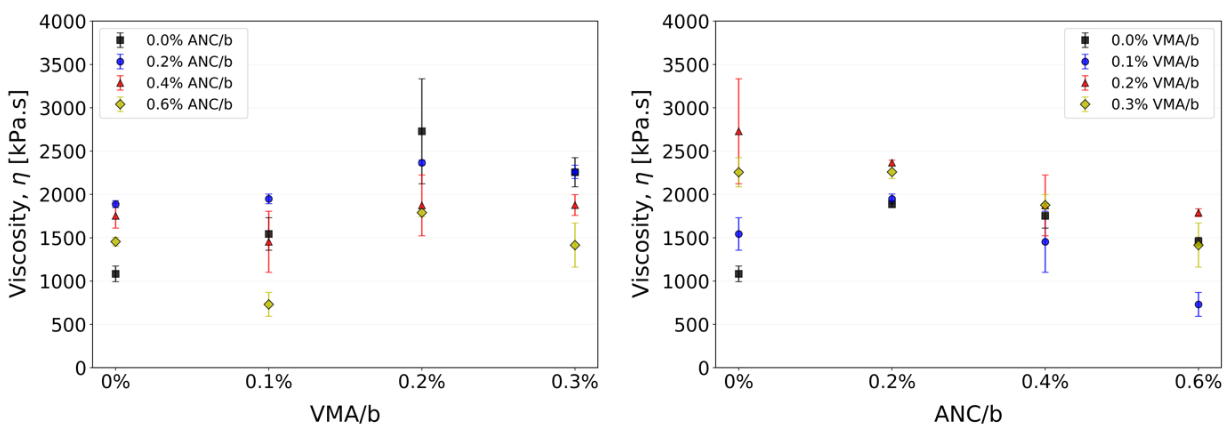

(a) (b)

Figure 4-6: Variation of plastic viscosity with (a) VMA and (b) ANC ratios

4.3.3. Viscoelastic Properties

Figure 4-7 shows the storage modulus (G') and loss modulus (G'') responses of the mixes to the strain amplitude sweep. Amplitude sweep test starts with a very low shear strain rate (0.01%), at which the material is not disturbed and thus the slopes of G' and G'' are expected to be flat. Figure 4-7a illustrates the G' and G'' measurements of the mixes with no ANC but varying VMA concentrations. It can be observed from Figure 4-7a that mix 1 has a concave down curve at the low shear strain amplitudes, which means the modulus increases first, reaches an equilibrium level (approximately 2 mins after start) and then decreases. This behavior can be attributed to the lack of network formation in the first couple of seconds [113]. Roussel et al. [113] studied the storage modulus responses of cement pastes in time. They observed that the storage modulus increases during the first 10 s of the test and then reaches a plateau. This means that, after 10 s, the network is formed and does not evolve anymore. The colloidal percolation characteristic time can therefore be of the order of a few seconds or minutes based on the mix design. This suggests that the mixes represented in Figure 4-7a, where there is no ANC and varying amounts VMA in the mixes, do not form a colloidal percolation in the system in the first couple of minutes. No clear pattern in the variation of G' and G'' is observed when the VMA concentration increases in the mixtures. Both elastic and viscous components of the viscoelastic properties decreases when the VMA ratio is 0.1% or 0.2%; however, both components increases when the VMA ratio is 0.3%.

On the other hand, increasing content of ANC consistently increases the elastic and viscous components of viscoelastic characteristics of the mixes as illustrated in Figure 4-7b. The addition of ANC results in a flat plateau in both G' and G'' response starting from very low shear strain amplitudes. As discussed in section 4.3.2., the bridging effect of ANC improves the modulus characteristics of the mortar mixtures. The amplitude sweep curves for the G' shifts upward with increasing amount of ANC. A similar trend is also observed for the amplitude sweep curves for the G'' but the rate of this shift decreases with increasing amount of ANC.

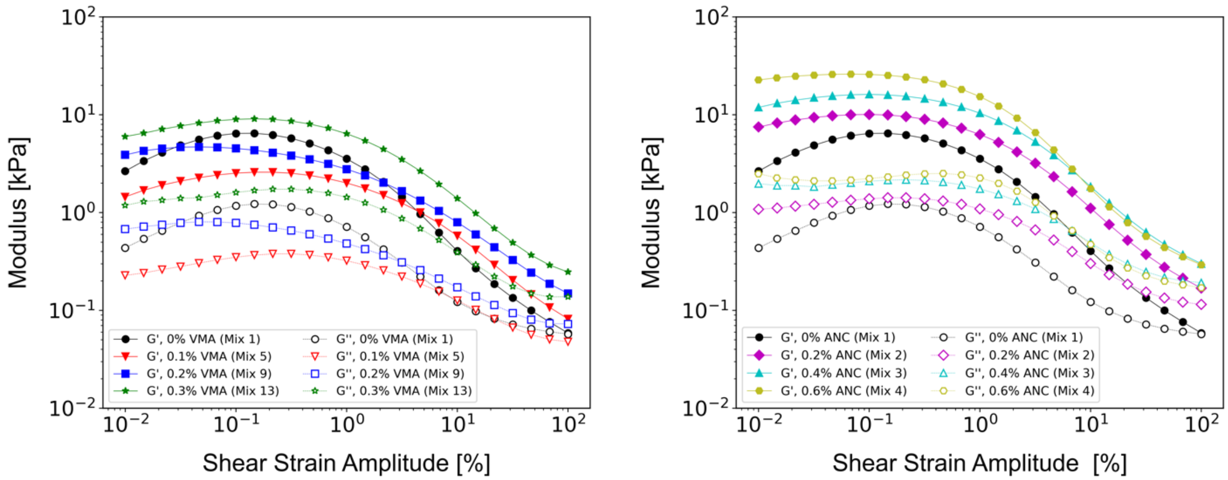

(a) (b)

Figure 4-7: Storage modulus and loss modulus as a function of strain for mortar specimens with (a) no ANC and varying amounts of VMA and (b) no VMA and varying amounts of ANC

The variation of storage modulus (G') measured at the upper limit of LVER with the VMA and ANC content are shown in Figure 4-8a and b. It can be seen from Figure 4-8a that increasing VMA content has almost no effect on G' for all mixtures except the ones with 0.6% ANC. For the mixes with 0.6% ANC, increasing VMA content increases the G' with a strong correlation (R^2 = 0.90). For all mixtures with various VMA concentrations, increasing the ANC content increases the G' as shown in Figure 4-8b. However, it is noted that the rate of this increase is higher when VMA is present in the mixtures. Figure 4-8c and d show the variation of the LVER, or critical strain with varying VMA and ANC concentrations, respectively. The particles in the matrix are closely interacted with each other and the material shows a linear elastic behavior within the LVER [114, 115]. It can be seen that the LVER is not impacted considerably by the addition of VMA or ANC and varies in the range of 0.19% and 0.22% for all sixteen mixtures tested in this study. The lowest value is observed for the control mixture (no VMA or ANC). This could be attributed to the lower amount of hydration products developed in the control mixture compared to the other mixtures as discussed in Section 4.3.2. Figure 4-8e and f show the variation of loss factor with respect to VMA content and ANC content. The loss factor provides information about the stability of the structure, where a lower value indicates that the mixture tends to hold its shape. As can be seen in Figure 4-8e and f the loss factor decreases with the VMA and ANC addition. The loss factor for the control mix is calculated as 0.18. Keeping the ANC content at 0% and increasing the VMA content to 0.3% decreases the loss factor to 0.15. On the other hand, there is a larger decrease in the loss factor with the addition of ANC content. For example, the mixture with no VMA and 0.6% ANC has a loss factor to 0.11.

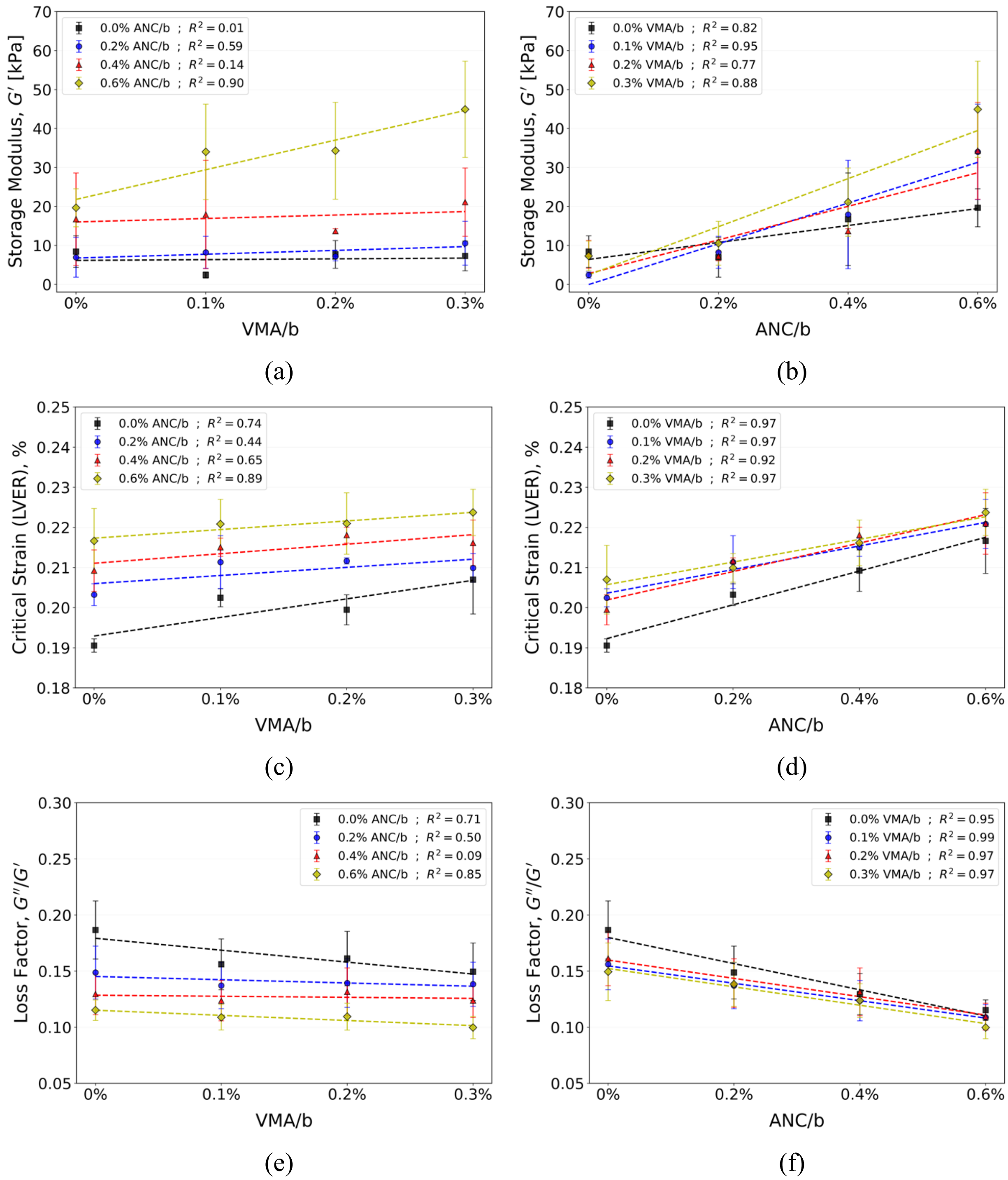

Figure 4-8: Variation of storage modulus with (a) VMA and (b) ANC ratios; variation of critical strain (LVER) with (c) VMA and (d) ANC ratios; and variation of loss modulus with (e) VMA and (f) ANC ratios

4.4. ANOVA Analysis

To statistically assess the effects of ANC and VMA on the response variables, such as DYS, SYS, storage modulus, Analysis of Variance (ANOVA) test is performed. In particular, a two-factor ANOVA test is conducted to quantify the effect of two independent variables, i.e., ANC and VMA, and their interaction effect, i.e., ANC*VMA on the dependent variables, i.e., rheological properties. The significance level of the ANOVA test is set to 0.05 (5%) and the corresponding p-values are summarized in Table 4-5.

There is no significant interaction effect between ANC and VMA since the p-values for all rheological properties are higher than 0.05 for the ANC*VMA. This indicates that the joint effect of ANC and VMA is not statistically higher than the sum of both effects individually. Regarding the individual effect of VMA, the p-values suggest that VMA is not statistically significant for the rheological properties except for plastic viscosity, LVER and loss factor. On the other hand, the effect of ANC is statistically significant for all the rheological properties but for plastic viscosity. Similar observations was reported in previous studies [110, 116, 117]. The oppositely charged edges of ANC particles tent to interact with each other to produce a denser microstructure, which leads to higher SYS and storage modulus. However, once the flow initiated, the particles tend to separate from each other and align in the direction of the flow. At this moment, the system loses the interaction between the ANC particles and to this end, possible electrical repulsion can cause further imbalance in the microstructure. Thus, ANC loses its significance on the plastic viscosity.

Table 4-5: Summary of the p-values from the two-factor ANOVA test to assess the statistical significance of ANC, VMA and ANC*VMA on the rheological properties

Rheological Property	ANC	VMA	ANC * VMA
DYS	0.001	0.31	0.06
Plastic viscosity	0.87	0.02	0.14
SYS	0.001	0.30	0.28
Storage modulus	0.01	0.65	0.06
LVER	0.001	0.01	0.25
Loss factor	0.001	0.01	0.16

4.5. Thermogravimetric Analysis (TGA)

Thermogravimetric analysis is used to analyze the thermal and hydration behavior of the mortar samples. The samples to be tested are collected from the core of the cubic specimens after the curing periods (7 days and 28 days), and then dried in the oven at 105 °C to stop hydration. Powdered samples are prepared by grounding the sample surfaces and then sieving through a 53 μm sieve. The powdered samples are then heated to 1000 °C at 10 °C /min under nitrogen flow. In order to quantify the total degree of hydration, the mass loss of the mortar samples is measured by TGA as a consequence of decomposition of cement hydrates [118]. The measurements are performed according to the following thresholds [119]:

- Water loss due to C-S-H decomposition that occurs between 25 °C and 350 °C
- Water loss due to the dihydroxylation of calcium hydroxide ($Ca(OH)_2$ or CH) that occurs approximately between 400 °C and 500 °C
- Carbon dioxide loss due to the decarbonization of $CaCO_3$ that occurs at temperatures from 500°C to 800°C

First, the residual weights are calculated at the temperatures where the dihydroxylation of calcium hydroxide (CH) peaked. Then, the CH content (%) is calculated by equation (3);

$$CH\ Content = W \times 74.1 \tag{3}$$

where W is the mass loss during dehydration of calcium hydroxide (CH), that occurs $% approximately between 400 °C and 500 °C. W is calculated as the percentage of the ratio of $% mass loss during dehydration of CH and the initial mass (%), where 74.1/18.0 is the molar weight ratio of CH to H_2O.

The thermogravimetric (TG) curves and the first derivative of TG (DTG) curves for the control mixture (mix 1), mixture with 0.6% ANC and no VMA (mix 4), mixture with 0.3% VMA and no ANC (mix 13), and mixture with 0.6% ANC and 0.3% VMA (mix 16) at 1 day and 7 days after casting are illustrated in Figure 4-9. The peaks in the DTG curves represent the decomposition of C-S-H and ettringites, calcium hydroxide (CH), and calcium carbonate ($CaCO_3$) as indicated in the plots. In addition, the residual weights at the CH decomposition and CH content in the temperature range between 400 °C and 500 °C for these mixtures at 1 day and 7 days are provided in Figure 4-10.

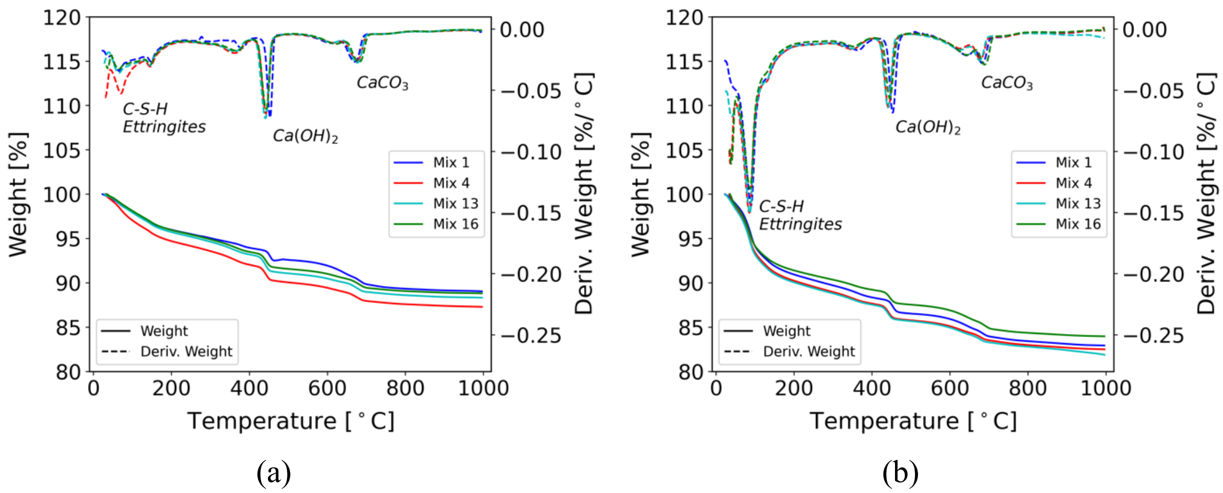

Figure 4-9: Thermogravimetric (TG) and first derivative of TG (DTG) curves of mixes 1, 4, 13, 16 at (a) 1 day and (b) 7 days after casting

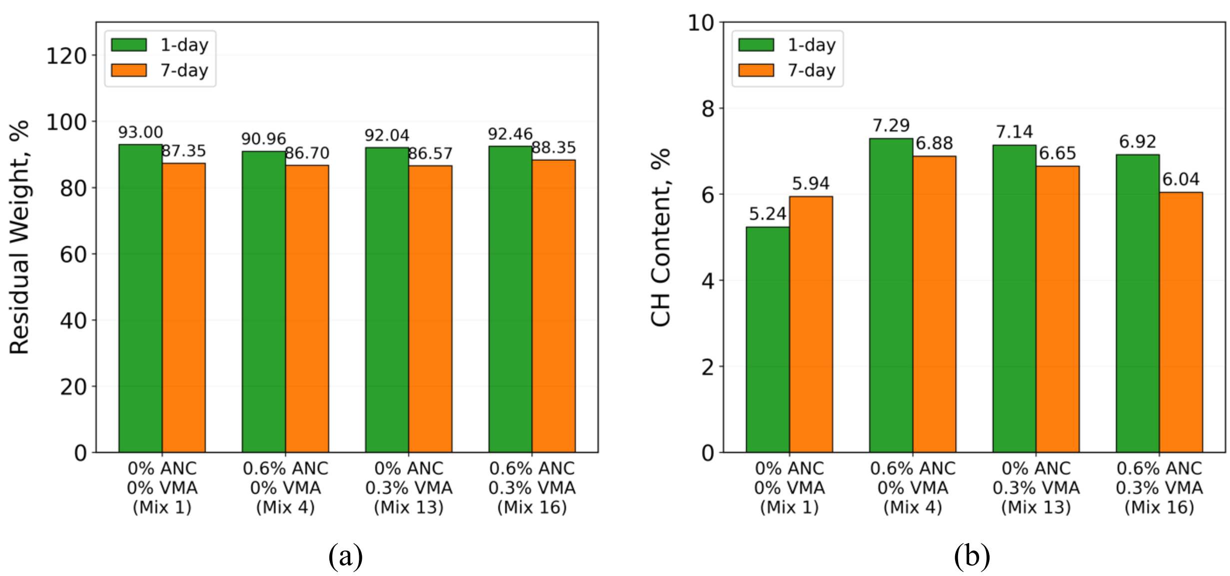

Figure 4-10: (a) Residual weights and (b) CH content of mixes 1, 4, 13, 16

The residual weight at 1-day decreased from 93.00% to 90.96% when 0.6% ANC is added (mix 4) in the base mix (mix 1). This indicates that more hydration products formed in the mix with the addition of ANC, 55.2% of which consists of SiO_2. This result can be attributed to the enhanced pozzolanic activity, and thus, enhanced hydration process due to the increased amount of SiO_2 in the mix [120]. On the other hand, the VMA affects the course of hydration less significantly compared with the addition of ANC. Compared to the base mix, addition of 0.3% VMA decreased the residual weight at 1-day to 92.04% from 93.00%. In addition, less effect on the hydration is observed when both ANC and VMA are present in the mix, where the residual weight is measured as 92.46%. It is also observed that the CH content at 1-day is increased from 5.24% to 7.29% when 0.6% ANC is incorporated in the mix. Adding 0.3% VMA increased the CH content at 1-day to 7.14%, whereas the CH content is measured to be 6.92% when ANC is also added in the mix. These results indicate that both ANC and VMA accelerates the hydration reaction of cement at early ages, while the ANC has the greater effect. This might be attributed to the increased speed of hydration due to the increased amount of SiO_2 that comes from ANC incorporation [121]. The effect of ANC on hydration is more pronounced in 1-day compared to the 7-day. It is also worth mentioning that the CH content is increased from 1-day to 7-day only for mix 1 where no ANC and no VMA is incorporated in the mixes. For all other mixes, the CH content decreases at 7-day compared to 1-day. This could be attributed to the consumption of CH and extra formation of C-S-H in the presence of SiO_2 when ANC is incorporated in the mixes.

4.6. Selection of Mixtures for Printability Characterization

The storage modulus and SYS are important material properties in quantifying the buildability and shape stability of the 3D printed concrete structures [79, 122]. The higher the storage modulus the more rigid the structure, as well as the higher the SYS the stronger the structure. In this study, the storage modulus and SYS are used to quantify the buildability and shape stability of the printable mixtures. Figure 4-11a shows the scatter plot of the storage modulus versus static yield stress for all the tested mixes. It can be seen from the scatter plot that storage modulus and static yield stress are considerably related to each other ($R^2 = 0.7$), i.e, higher the storage modulus higher the SYS. In order to study the buildability of the mixes experimentally, an unsupervised machine learning algorithm is used to select mixtures for the experiments. In particular, K-means clustering algorithm is used to cluster the mixes in subgroups where the mixes in each subgroup behave similar to each other according to the similarity measure, Euclidean-distance. To find the optimal number of clusters, the elbow method is used which suggests that 3 clusters (Figure 4-11b) for these 16 mixes gives the best model fitting of K-means algorithm.

Based on the K-means clustering algorithm, 16 mixes are clustered in 3 subgroups and these subgroups are named as cluster 1, cluster 2, and cluster 3, as shown in Figure 4-11a. The sign "×" in each cluster represent the centroids of that cluster. The variation of the data points in cluster 1 is observed to be relatively low. Considering the low storage modulus and static yield stress values of the mixtures in this cluster, one typical mix is considered to be adequate to assess the buildability mixtures in cluster 1. Mix 13 is selected from cluster 1 since it is the closest to the centroid of this cluster. Similarly, from cluster 2, mix 4 is selected since it is very close to the centroid of the cluster. Also, considering the large variation in the storage modulus, mix 14 and mix 15 are selected which have the lowest and highest storage modulus values, respectively, in cluster 2. From cluster 3, all the mixes (mix 8, mix 12 and mix 16) are selected for buildability assessment. Table 4-6 shows the summary of the rheological results of the selected mixes.

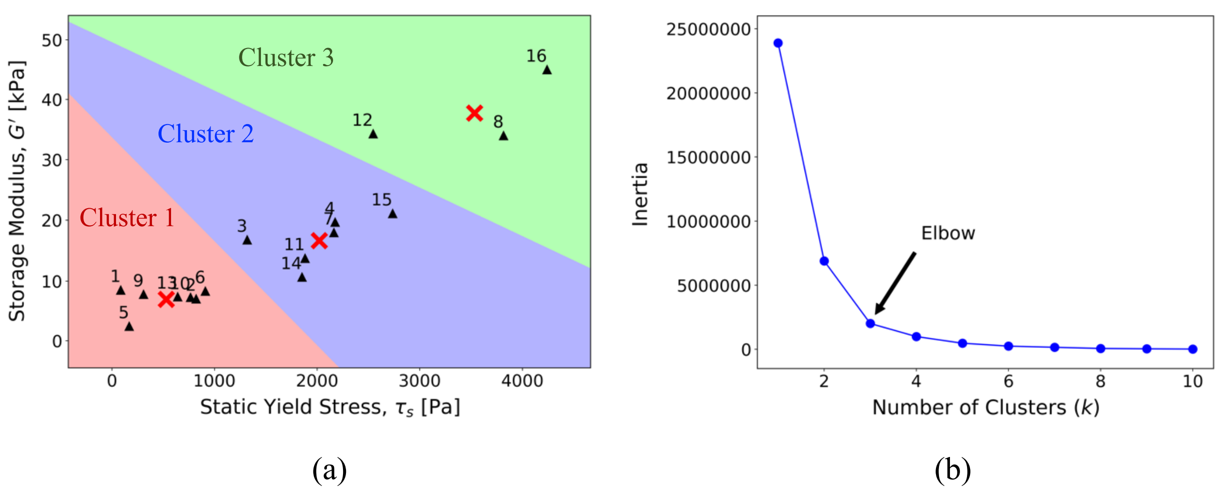

Figure 4-11: (a) Storage modulus and static yield stress of all the mixes, and (b) elbow method to determine the optimal value of clusters in K-Means algorithm.

Table 4-6: Summary of the rheological results of the selected mixes

Mix	VMA/b [%]	ANC/b [%]	DYS [Pa]	Viscosity [kPa.s]	SYS [Pa]	G' [kPa]	LVER [%]	Loss Factor
4	0	0.6	448	1455	2175	19.65	0.217	0.125
8	0.1	0.6	805	730	3816	34.01	0.221	0.108
12	0.2	0.6	718	1789	2546	34.29	0.221	0.109
13	0.3	0	73	2256	641	7.30	0.206	0.149
14	0.3	0.2	317	2260	1853	10.54	0.210	0.138
15	0.3	0.4	601	1877	2735	21.10	0.216	0.124
16	0.3	0.6	935	1415	4240	44.93	0.224	0.099

4.7. Buildability Assessment

A direct printing test is performed to assess the buildability of the select mixtures. The results for mixture 13 from cluster 1 is shown in Figure 4-12. Due to the low DYS value (73 Pa), the extrusion of mix 13 is observed to be smooth and continues. However, no layer formation is observed including the first layer. The SYS of mix 13 is measured as 641 Pa and this level of yield stress is not enough to withstand the gravitational induced strength of the mix. The breadth of the first layer is approximated about 55 mm while the nozzle size is 15 mm. After five layers of the mix 13 is extruded, the breadth of the initial layer is measured as 108 mm as shown in Figure 4-12. From these results, it is suggested that mix 13 is not printable. Assuming the other mixes in this cluster behave similarly, it can be concluded that cluster 1, where the static yield stress and the storage modulus of the mixes are; $SYS < 910\ Pa$ and $G' < 8.4\ kPa$, is not printable.

Mix 13

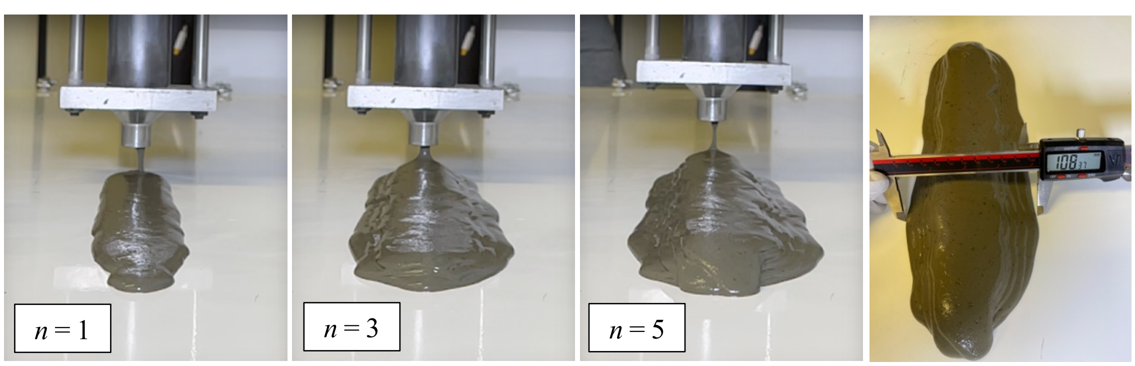

Figure 4-12: Print result of mix 13 from cluster 1

Figure 4-13 shows the print result of the mixes 14, 4 and 15 from cluster 2. The DYS values range from 317 Pa and 601 Pa for these mixtures. Initial printed layers of all the mixtures in cluster 2 suggest that the DYS range is adequate for these mixes since smooth and continuous extrusion is performed. The mixes in Figure 4-13 are ordered in ascending number of maximum printable layers before failure (n_{max}). In particular, the maximum number of printable layers for the mixes 14, 4 and 15 are 8, 10 and 14, respectively. It can be seen from Figure 4-11a that the mixes 14, 4 and 15 are also in ascending order in terms of storage modulus and SYS. This suggests that n_{max} increases with the increase in the storage modulus and the SYS. Pearson correlation coefficient, which is a measure of linear correlation between two sets of data, between n_{max} and storage modulus is calculated as 0.93, whereas the correlation coefficient between n_{max} and SYS is calculated as 0.88. Therefore, it can be said that n_{max} is more correlated with storage modulus.

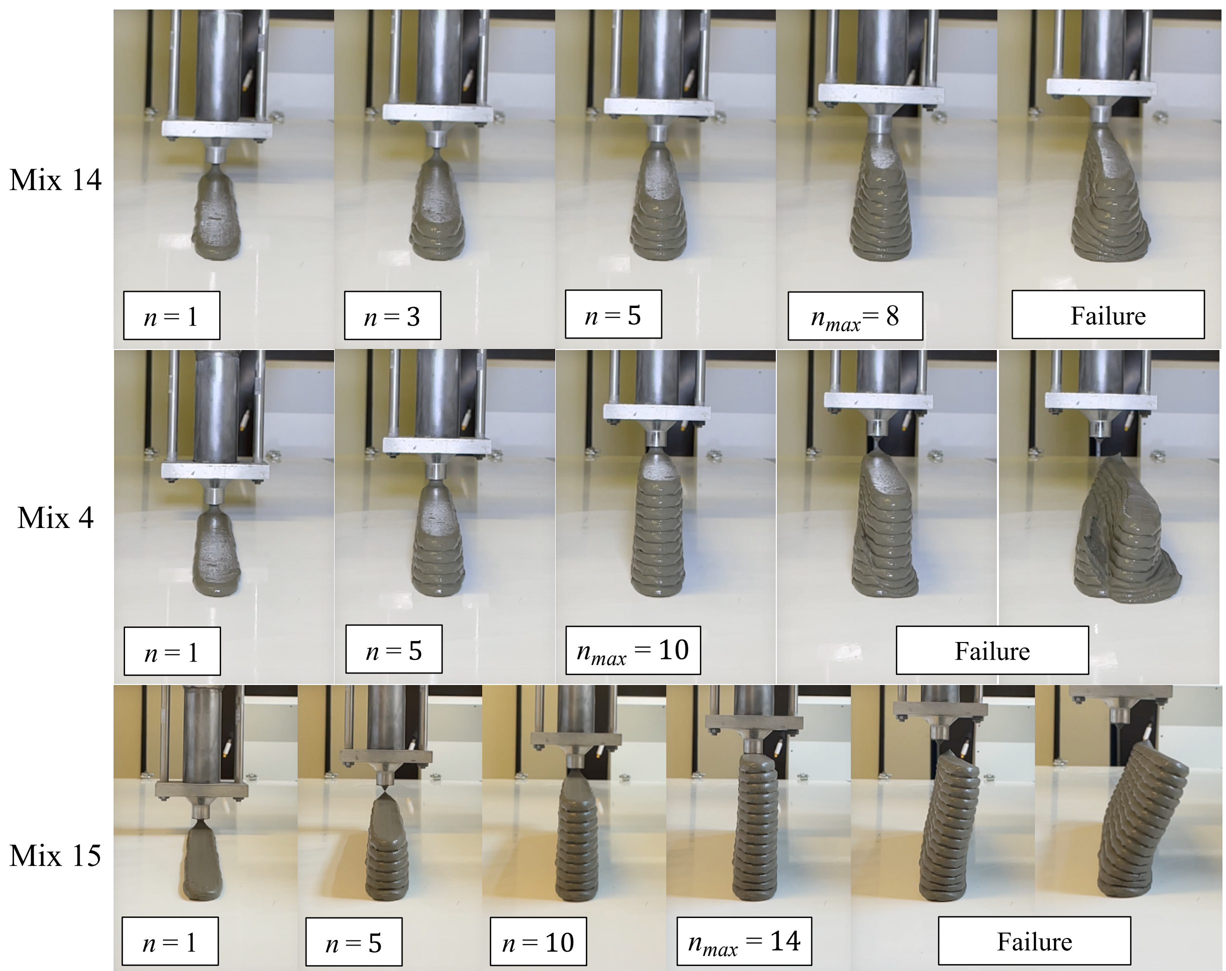

Figure 4-13: Print results of mix 14, mix 4 and mix 15 from cluster 2

Cluster 3 contains mix 12, mix 8 and mix 16 which have the largest values of storage modulus and SYS. Figure 4-14 shows the print results for the mixes in cluster 3. Mix 16 has the maximum DYS as 935 Pa among all the mixes and no voids or breaks are observed in the extrusion of this mix. From here, it can be concluded that all the mixes can be extruded smoothly and continuously without any observable failures in the filament during extrusion. It can be concluded that these three mixes have sufficient SYS to carry their own weight since no spread of the material initiated the plastic collapse. The maximum number of printable layers for mix 12, mix 8 and mix 16 are 22, 24 layers and 50 layers, respectively.

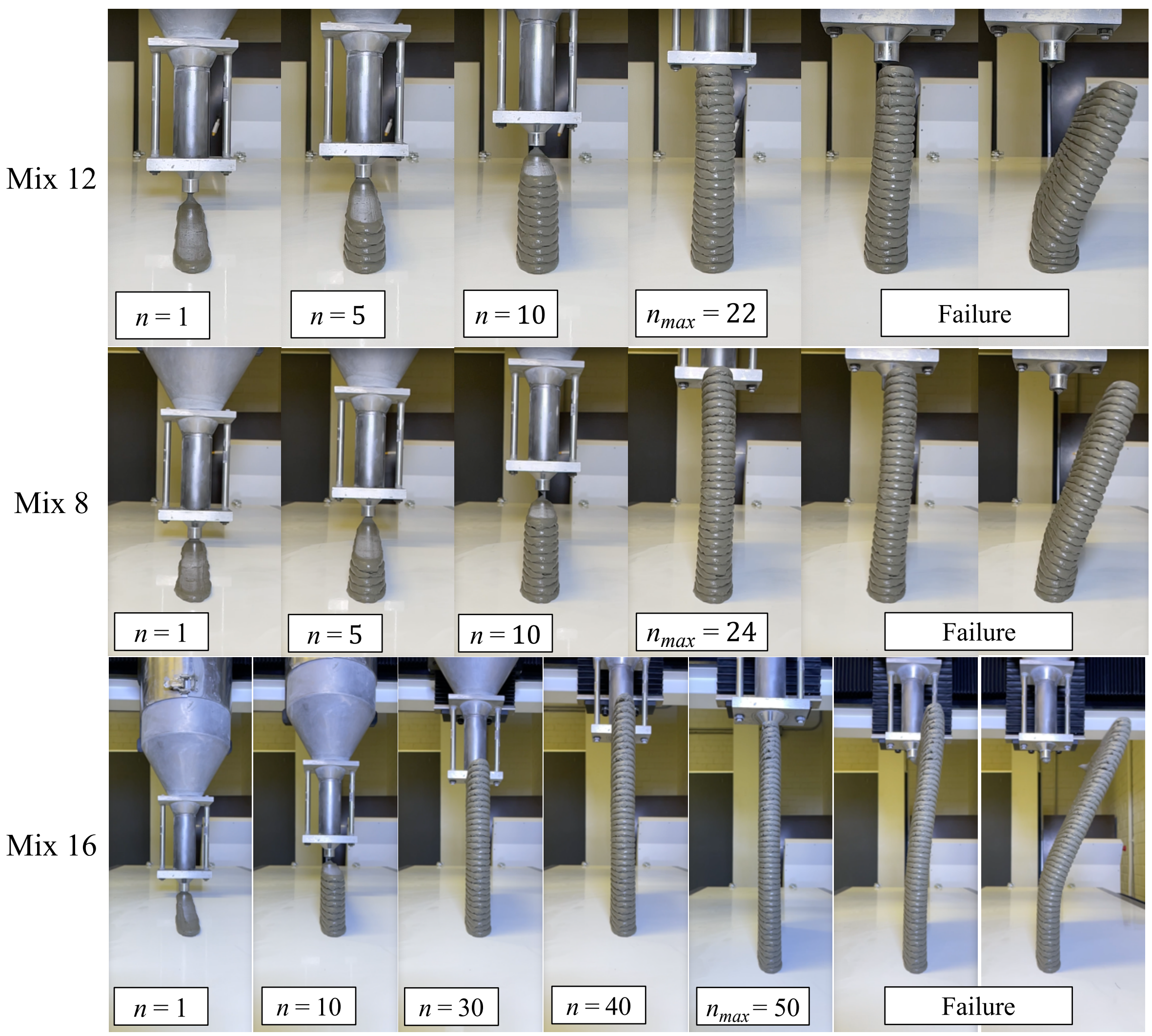

Figure 4-14. Print results of mix 12, 8 and mix 16 from cluster 3.

The printed filament is expected to withstand its own weight caused by the gravitational force, and the weight of the subsequent layers. In Figure 4-14, the first 10 layers of each mix in cluster 2 suggests that the static yield stress of each mix is enough to carry its own weight since no visible spread of the material is observed in the initial layers. Figure 4-15 shows the filament breadth and height of mix 12 from cluster 3. Due to the viscoelastic behavior of the mortar, the experimental breadth is measured as 30 mm for each layer ($b_{exp} = 30\ mm$) while the mortar was extruded from a 15 mm nozzle. Since b_{exp} is measured as 30 mm for the first layer of all the mixes in clusters 2 and 3, and since no additional spread of the material is observed after printing the initial layer, it is suggested that the minimum SYS in both of these clusters (1318 Pa) is enough for a layer to carry its own weight. However, additional deposition of layers cause deformation in the initial layers as mix 14 exemplifies this. Mix 14 has the lowest storage modulus in cluster 2 and it is observed that further layer deposition after the first layer results in filament spread in the initial layers. The breadth of the first layer is measured as 50 mm when 8 layers are printed right before failure. No clear spread in the initial layers is observed for mixes in cluster 3, where the mixtures have the largest SYS values. Thus, it can be said that the initial layers can keep their shape and no spread occurs when the SYS is over 2546 Pa. Considering the breadth of the mixes (30 mm) and the aspect ratio of the target wall (10), a total print height of 300 mm is aimed for this study. Taking into account the height of each layer (7.5 mm), the expected number of printable layers (n_{theo}) is calculated as 40 layers (300 mm / 7.5 mm). Only mix 16 is ensured this requirement with 50 layers that exceeds $n_{theo} = 40$.

Figure 4-15. Layer breadth and layer height of mix 12 from cluster 3

In order to better understand the effects of VMA and ANC on the buildability and failure mechanisms of the printed sample, the SYS, storage modulus and maximum number of printed layers are shown in Figure 4-16 and Figure 4-17 together with the failure images of the samples. Figure 4-16 shows the results for mixes 13, 14, 15, and 16 where the VMA content is fixed at 0.3% and the ANC content is varied from 0% to 0.6%. Mix 13 is noted as not printable since the SYS of the mix is not enough to form the initial layer. This mix has the maximum level of VMA content (level 4) but no ANC (level 1), which suggests that VMA do not have significant effect on shape retention. Increasing the ANC content to 0.2% (mix 14) yields a successful initial layer formation, however, the increased stress due to the weight of subsequent layers lead to high deformations in the initial layers and hence plastic collapse is observed for mix 14 after printing 8 layers. Increasing the ANC content to 0.4% considerably improves the buildability and shape stability. Mix 15 is observed to keep the shape of the initial layers until 13th layer is printed. After printing the 14th layer, a slight spread on the initial layers is observed as indicated in a red circle in Figure 4-16 which can be described as a local plastic deformation. Also, an inclination to the right is observed after printing the 14th layer. Therefore, it is suggested that the failure mechanism is a combination of elastic buckling and plastic deformation for mix 15. On the other hand, no visible spread and layer deformation is observed for mix 16. As it is clear from Figure 4-17 that the failure mechanism for mix 16 is purely elastic buckling. After printing the 50th layer, the buckling is observed in the middle of the structure following the failure.

Similarly, Figure 4-17 shows the results for mixes 4, 8, 12 and 16 where the ANC content is 0.6% for all mixes and the VMA content of each mix is 0%, 0.1%, 0.2% and 0.3%, respectively. The plastic collapse of the structure is observed for mix 4 after successfully printing 10 layers. When compared to mix 14 from the same cluster, less spread of the initial filaments is observed for mix 4 and a sudden plastic collapse is occurred. Mix 8 and mix 12 have similar storage modulus values (34.0 kPa and 34.3 kPa, respectively) and hence similar number maximum layers (24 and 22, respectively). They also demonstrate similar failure mechanism where slight deformations in the initial layers are observed for both of the mixes followed by elastic buckling. It can be said that mix 8 and mix 12 have elastic buckling failure where the failure is started at the bottom of the structure due to plastic deformation.

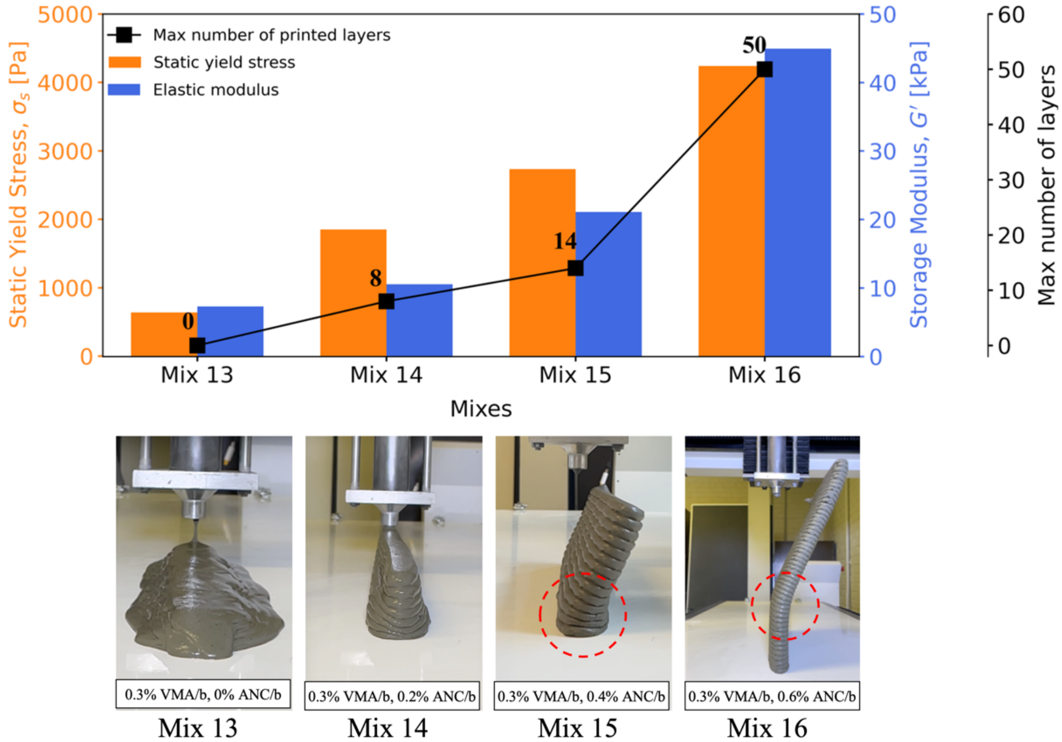

Figure 4-16. Static yield stress, storage modulus, maximum number of layers and the failure mechanism of the mixes 13, 14, 15 and 16

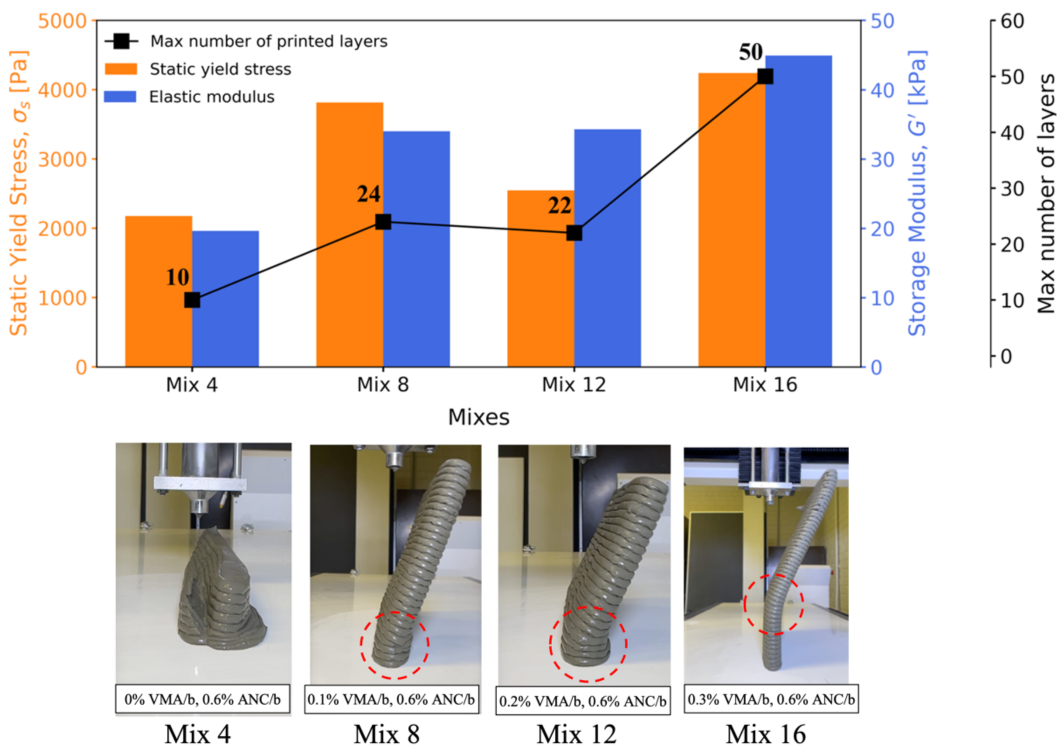

Figure 4-17. Static yield stress, storage modulus, maximum number of layers and the failure mechanism of the mixes 4, 8, 12 and 16

To predict the failure criteria based on storage modulus and SYS, the support vector classifier (SVM), a supervised machine learning algorithm, is used to classify the mixes and find the decision boundaries. Figure 4-18 summarizes the printability regions and the failure mechanisms of the mixes based on the SVM algorithm. Mix 13 of cluster 1 is found to be not printable and considering the other mixes in cluster 1 behave similarly according to the SVM model, it can be concluded that the mixes in cluster 1 is not printable (shown as "NP" in Figure 4-18). The storage modulus and the SYS of the mixes in this region are less than 8.4 kPa and approximately 1000 Pa, respectively, which means that 8.4 kPa of storage modulus and 1000 Pa of SYS are not adequate for a mix to be printable. Other than this cluster 1, all the mixes are printable with different failure criteria. Mix 4 and Mix 14 are located at the bottom-left part of cluster 2 and plastic collapse (PC) failure is observed for these mixes. Therefore, it is predicted with SVM that the mixes, having storage modulus values in the range of 10.5 kPa and 19.6 kPa, and SYS values in the range of 1853 Pa and 2175 Pa, are printable but will experience a failure mechanism of plastic collapse. The upper-left portion of cluster 2 and lower region of cluster 3 showed slight plastic deformations on the initial layers, however, the main failure criteria is considered to be elastic buckling (EB). Mix 12, mix 15 and mix 8 are observed to be located in this region with storage modulus values from 21.1 kPa to 34.3 kPa, and SYS from 2546 Pa to 3816 Pa. Only mix 16 showed a pure elastic buckling (Pure EB) failure since no visible plastic deformation is observed on the initial layers. This suggests that a storage modulus value of >45 kPa and a SYS value of >4200 Pa are required for a print that no spread and plastic deformation occurs on the initial layers.

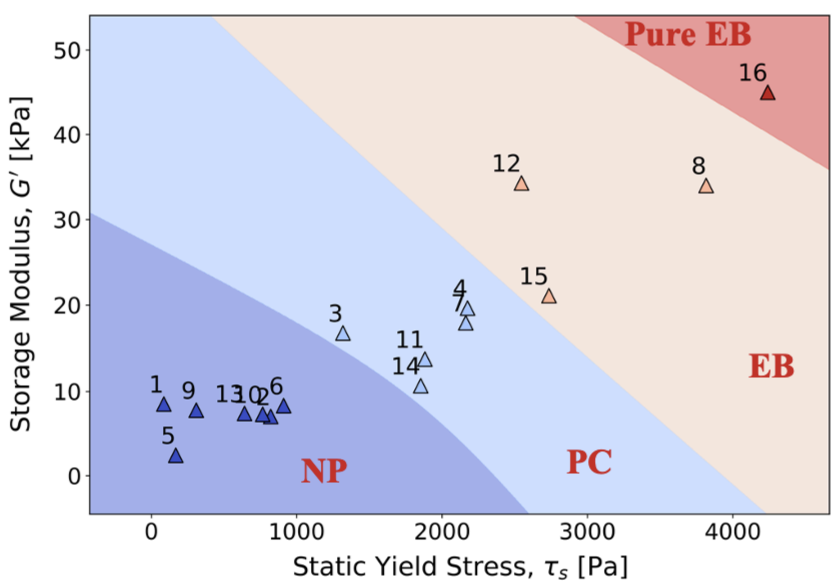

Figure 4-18. Printability diagram of the mixes based on storage modulus and static yield stress

4.8. Summary

In this section, the rheological and viscoelastic properties of cementitious mixtures that contain different levels of VMA and ANC are investigated. The rheological properties are obtained from ramp and stress growth tests and analyzed in terms of dynamic yield stress (DYS), plastic viscosity, and static yield stress (SYS). An amplitude sweep test is conducted to evaluate the viscoelastic properties such as storage modulus, loss modulus and linear viscoelastic range (LVER). Based on the results of the rheological testing, a K-means clustering algorithm is used to cluster the sixteen mixtures evaluated in this study into three clusters. The direct printing tests using mixtures from each cluster are conducted to evaluate the extrudability and buildability of the selected mixtures. The findings of this study can be summarized as follows:

- There is almost a linear increase in the SYS and DYS values of mortar mixtures with the addition of ANC. The rate of this increase is slightly higher when VMA is also exists in the mixture. On the other hand, the SYS and DYS experience a more modest increase with the addition of VMA. Also, the correlation coefficient is smaller for the VMA.
- No clear pattern is observed on the variation of plastic viscosity with the addition of VMA or ANC. Nevertheless, the addition of ANC generally decreases the plastic viscosity while the addition of VMA generally increases the plastic viscosity.
- The addition of VMA has almost no effect on the storage modulus for the mixtures with or without ANC except the mixtures with the highest amount of ANC. It also has no significant influence on the loss factor, but it generally leads to a slight decrease in the loss factor.
- On the other hand, the addition of ANC considerably increases storage modulus while results in a decrease in loss factor. The correlation between the ANC ratio and storage modulus is not as strong as the one between ANC ratio and SYS but the coefficient of determination is still above 0.76 for the mixtures with constant VMA ratio and varying ANC content.
- The ANOVA results also indicates that the ANC has statistically significant effect on the SYS and viscoelastic properties of mortar mixtures, while the major influence of VMA is on the plastic viscosity of the mixtures.

- The mortar mixtures with a SYS less than 1000 Pa and a storage modulus less than 8.4 kPa cannot retain their shape after being extruded.
- The mixtures with a SYS ranging from 1000 to 2200 Pa and a storage modulus ranging from than 8.4 kPa to 20 kPa experience plastic collapse. A mix of plastic collapse and elastic buckling failures are observed for the mixtures with a SYS between 2200 Pa and 4200 Pa and storage modulus between 20 kPa and 45 kPa.
- A mixture with a SYS over 4200 Pa with a storage modulus of over 45 kPa is found to be capable of retaining its shape and carry the deposited layers without any plastic deformation. For such a mixture, the failure mode is observed to be pure elastic buckling.

5. Effects of CNF on Rheo-viscoelastic, Printability and Mechanical Characteristics of Cementitious Composites

5.1. Overview

This study explores the effects of cellulose nanofibers (CNF), a relatively new type of nanocellulose material, on the printability characteristics such as extrudability and buildability of cementitious mixtures. First, mortar mixtures with varying ratios of CNF are prepared. The rheology of the mixtures containing CNF is thoroughly assessed using a shear rheometer. Two testing protocol are followed: ramp test and stress growth test. A ramp test is conducted to determine dynamic yield stress and plastic viscosity using Bingham visco-plastic material model. Stress growth tests are carried out at varying resting periods to quantify static yield stress and thixotropy of the cementitious mixtures. Amplitude sweep test is carried out to determine viscoelastic properties of the mortar mixes, including storage modulus that is found to be critical for buildability. Thermogravimetric analysis is conducted to assess the effects of CNF on hydration characteristics of the mixtures. Compressive strength and flexural strength tests are conducted to assess the mechanical properties. Finally, the printability of the mortar mixtures incorporating CNF is assessed using a 3D concrete printer equipped with a 15 mm diameter nozzle and screw pump.

5.2. Materials and Mixture Preparation

The CNFs used in this study are in the form of fibrous rods sourced from wood pulp and readily biodegradable according to the manufacturer. CNFs are manufactured by mechanical fibrillation followed by processing dilute slurries of cellulose fibers through grinding or high-pressure homogenizing action [123]. After manufacturing, an evenly dispersed CNF aqueous suspension occurs as a colloidal system as a 3% slurry which consists of 3% dry CNF and 97% water. CNFs have a noticeably high aspect ratio with dimensions of 20-50 nm in diameter and lengths of up to several hundred microns. CNFs have the ability to interact with matrix of a composite material both physically through its extreme surface area and chemically through hydrogen bonding. To study the effect of CNF on the mortar mixtures, mortar mixtures with varying CNF ratios (0%, 0.1%, 0.2%, 0.3%, 0.4%, 0.5%) are prepared. The binder for the mortar composite includes type I/II Portland cement, calcium sulfoaluminate (CSA) cement, non-crystalline silica fume (SF), and class F fly ash (FA). An industrial quartzite sand with a particle size distribution ranging from 0.15 mm to 0.60 mm is used as fine aggregate. In order to mitigate the risk of cracking due to drying shrinkage, an expansive agent (EA) is incorporated in the mixes. A high efficiency polycarboxylate based superplasticizer (SP) is added to enhance the workability of the mortar mix without any segregation, and the water to binder ratio (w/b) is maintained at 0.37. The control mix proportions are presented in Table 5-1, and the mix design used in the present study is shown in Table 5-2.

Table 5-1: Material proportions of the control mix (by weight percentage of binder)

Binder				EA	Sand	Water	SP
OPC	CSA	SF	FA				
0.68	0.05	0.05	0.22	0.03	0.52	0.37	0.012

Table 5-2: Mix design

	Mix 1	Mix 2	Mix 3	Mix 4	Mix 5	Mix 6
Cellulose Filaments (CF) (*wt.% of cement*)	0	0.1	0.2	0.3	0.4	0.5

To prepare each batch of mixtures, the required amount of CNF slurry is first mixed with the half of the total mixing water using a high shear mixing for 10 mins at 5000 rpm. All the dry materials are mixed for 5 mins at 50 rpm using a 20 qt Hobart mixer. After achieving a homogenous dry mixture, the CNF solution and rest of the water with dissolved SP are added to the dry system and mixed for 3 mins at 100 rpm. Then, the mixture is mixed for an additional 3 minutes at a speed of 200 rpm to achieve a homogenous mixture. Once the final mixing is complete, samples are taken for rheological, printability and mechanical assessments.

5.3. Printing Specimens for Mechanical Tests

The mortar mixtures with added CNF at different ratios were printed to prepare specimens for mechanical tests. A rectangular nozzle with a breadth of 20 mm and height of 10 mm was used for printing. All the mechanical tests were performed after 28 days of curing using a 100 kN capacity MTS machine.

To characterize the tensile behavior of the printed mortars, uniaxial tensile tests were conducted on dog-bone shaped specimens based on the recommendations of the Japan Society of Civil Engineers [106]. Two loading directions were considered; one is perpendicular to the printing direction (T1), and the other is parallel to the printing direction (T2) as shown in Figure 5-1. For loading direction T1, a single-line wall was printed with dimensions of 270 × 20 × 330 mm, and three dog-bone shaped specimens were precisely cut using a water jet. For T2 loading direction, two layers of three side-by-side filaments were printed in 1000 mm long, and similarly three dog-bone shaped specimens were cut.

Four-point bending tests were performed using 40 × 40 × 160 mm test prisms according to ASTM C348. To prepare the tests specimens, first a long prism with dimensions of 40 × 40 × 1000 was printed and then samples with the desired dimensions were cut using a water jet. The samples were tested in F1 and F2 loading directions (Figure 5-1) to analyze the anisotropic behavior of the printed samples.

The compressive strength of the specimens was evaluated using 50 × 50 × 50 cubic specimens according to ASTM C109. Two loading directions (C1 and C2) were considered as shown in Figure 5-1 to study the anisotropy in the printed samples. A 350 mm-long prism with five vertical layers and three lateral filaments was printed and six cubic specimens were cut using a water jet, where three of them were tested in C1 direction and the other three were tested in C2.

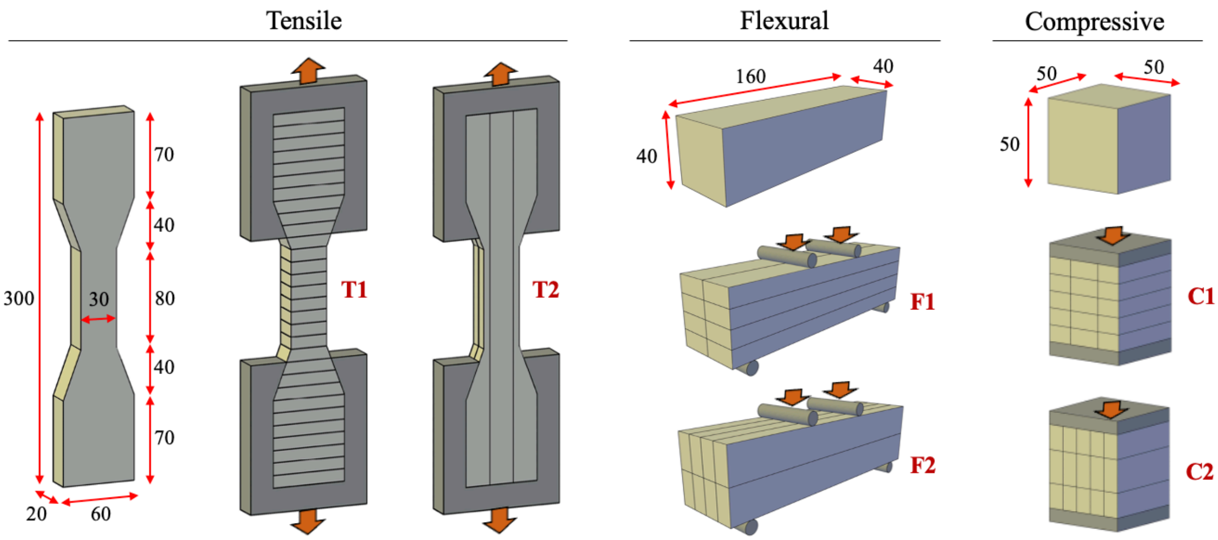

Figure 5-1: Schematic illustration of the loading directions and dimensions of the 3D printed samples for uniaxial tensile, flexural and compressive testing (*all dimensions are in mm*).

5.4. Rheo-viscoelastic Properties

5.4.1. Static Yield Stress (SYS)

Figure 5-2a shows the flow curves of the mixes from each stress growth tests, and Figure 5-2b shows the average value of SYS for mixtures with different CNF concentration. The results of the stress growth tests showed that the addition of CNF led to a significant increase in the SYS of the cementitious composites. Specifically, the SYS increased from 86 Pa for the 0% CNF to 1220 Pa for the 0.1% CNF content. This suggests that the addition of CNF can significantly improve the resistance of the mixtures to deformation and failure under static loads. Further increase in the CNF concentration increased the SYS to a maximum level of 10313 Pa when 0.5% CNF is incorporated in the mixture. The results of SYS for different CNF concentration are also analyzed by fitting polynomial models to the data. The best fitting model was found to be quadratic, with a coefficient of determination (R^2) of 0.996, indicating a strong correlation between the CNF concentration and the flow behavior of the mixtures.

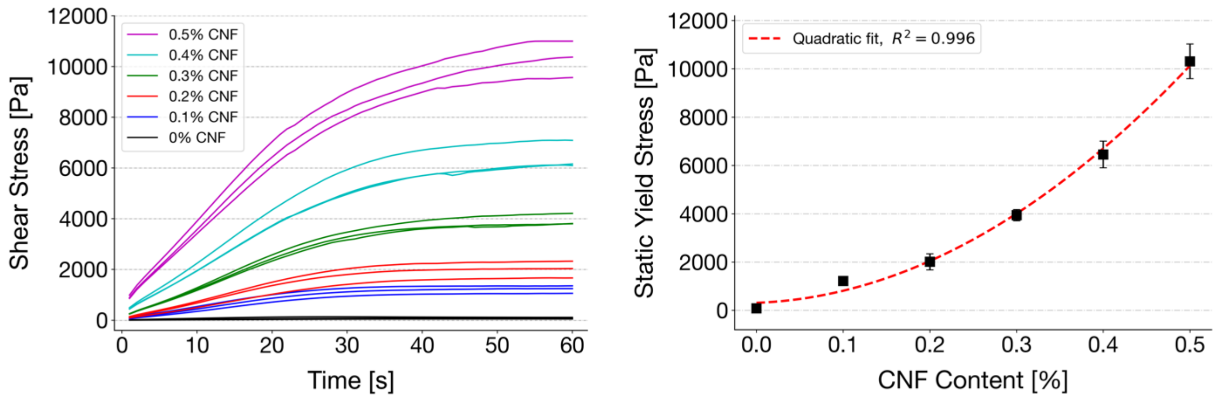

(a) (b)

Figure 5-2: (a) Flow curves, and (b) static yield stress of the mixes with increasing CNF content

5.4.2. Dynamic Yield Stress (DYS) and Plastic Viscosity

Increasing the CNF concentration constantly increased DYS as shown in Figure 5-3a. However, the rate of this increase initially remains small and becomes large when the CNF ratio is over 0.3%. The DYS of the base mix (0% CNF) was measured as 60 Pa and increasing the CNF concentration to 0.5% increased the DYS up to 4099 Pa. Similarly, the plastic viscosity of the mixtures also increases with the addition of CNF (Figure 5-3b) but with a decreasing rate. The plastic viscosity increased by a factor of 6.8 from 1237 kPa.s to 8064 kPa.s when the CNF content is increased from 0% to 0.4%. Note that further increasing the CNF concentration to 0.5% causes a slight decrease in the viscosity. High R^2 values (> 0.98) for quadratic fits also supports the presence of strong correlations between CNF and DYS and viscosity.

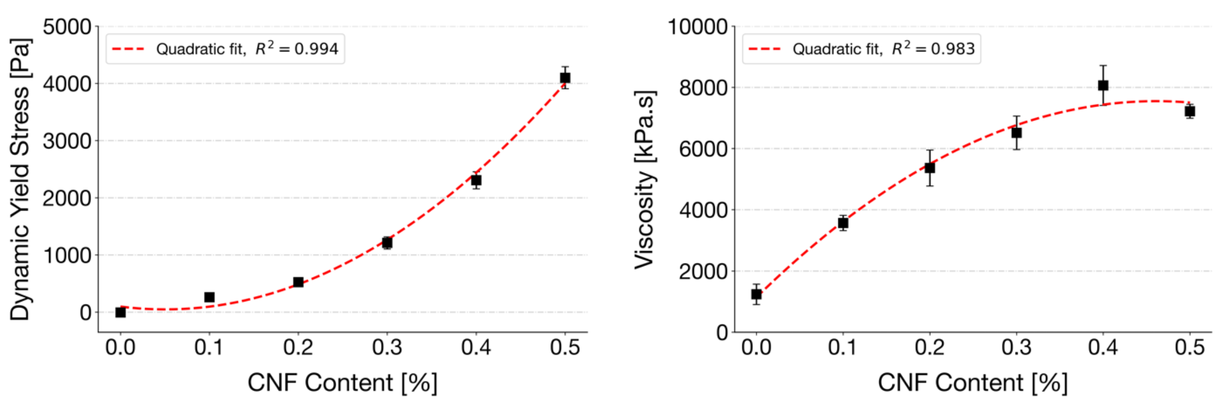

(a) (b)

Figure 5-3: (a) Dynamic yield stress, and (b) viscosity values of the mixes with increasing CNF concentration

5.4.3. Viscoelastic Properties

The storage modulus and critical strain of the mixtures were evaluated from the amplitude sweep tests. Similar to the other rheological properties, the storage modulus increased significantly with increasing CNF concentration as shown in Figure 5-4a. The mixture with the 0.5% CNF mixture exhibited the highest storage modulus of 117.6 kPa, while the storage modulus of the base mix was measured as 8.4 kPa. The critical strain also increased with increasing CNF concentration, especially for higher CNF ratios (Figure 5-4b). While the critical strain of the base mixture was measured as 0.19, the mixture with 0.5% CNF had a critical strain of 0.34%. These increases in storage modulus and critical strain suggest that the addition of CNF can effectively enhance the stiffness and elastic response of the mixtures. The mixtures with higher CNF contents will have greater resistance to deformation and failure under applied loads and can better withstand the applied stress or strain without going through plastic deformation.

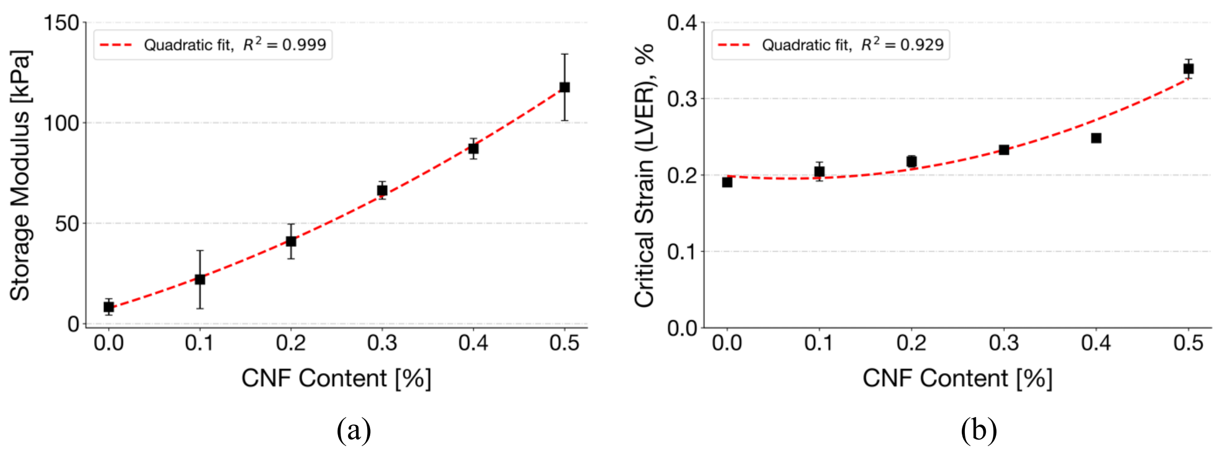

Figure 5-4: (a) Storage modulus, and (b) critical strain values of the mixes with increasing CNF concentration

These significant increases in the rheological properties when the mortar mixes are reinforced with CNF could be attributed to several factors. Firstly, CNF has a high aspect ratio and high surface area, which can facilitate the formation of a strong interfacial bond between the CNF and the cement matrix [124]. This can result in a reinforcement effect that improves the internal coherency of the matrix. Also, the higher intrinsic strength and stiffness of the nanofibrils [125] are likely to result in the formation of strong bonds between the cellulose fibers and the cementitious matrix. This is due to the presence of free hydroxyl groups that can be chemically bound with hydration products [126]. As a result, it is expected that the bonding between the cellulose fibers and the matrix will be strong. Secondly, the CNF not only act as a filler in the matrix to enhance the microstructure but also has the potential to act as an activator to stimulate the hydration reaction [127]. In particular, they serve as nucleation sites, which promote the precipitation and accumulation of hydrated products in the initially water-filled open pores. This process leads to the development of a more uniform, dense, and compact microstructure in the cementitious mixture containing CNF when compared to the mixture without CNF. Lastly, CNF can improve the microstructure of the matrix, reducing porosity and enhancing the interparticle packing density. As the dosage of CNFs increases, the peak also increases, suggesting a greater reduction in the volume of small pores in the pure cement paste compared to other materials [128]. This can improve the load transfer between the particles and increase the strength of the matrix.

5.5. Thermogravimetric Analysis (TGA)

The thermogravimetric (TG) curves and the first derivative of TG (DTG) curves are illustrated in Figure 5-5 where the CNF content was varied from 0% to 0.5% by weight. In addition, CH content in the temperature range between 400 °C and 500 °C and the hydration percentage for these mixtures at 1 day and 7 days are provided in Figure 5-6. The results indicate a notable effect of CNF addition on the CH content and hydration percentage of the cementitious mixtures at both 1 day and 7 days. With a 0.1% addition of CNF, the CH content at 1 day increased from 4.5 to 5.1, while the hydration percentage slightly rose from 27.0 to 27.2. As the CNF content was further increased to 0.2%, a more significant increase was observed in both CH content (5.5) and hydration percentage (29.7) at 1 day. Notably, the 0.3% CNF addition led to a decrease in the CH content to 4.3 at 1 day, but still showed an increase in hydration percentage to 28.4 as compared to control mix (27.0). A similar trend was observed for the mixtures with 0.4% and 0.5% CNF, where the CH content increased to 5.4 and 5.0, and the hydration percentages reached 28.3 and 29.9, respectively, at 1 day. After 7 days, the CH content and hydration percentage demonstrated a general upward trend with increasing CNF content, with the highest values observed for the mixture containing 0.5% CNF (CH content of 6.4 and hydration percentage of 35.6). These findings suggest that CNF addition has a significant impact on cement hydration, with higher CNF content generally leading to increased CH content and hydration percentage at both early and later stages. The results are in line with previous studies that have reported the impact of cellulose fibers on cement hydration [129, 130].

One possible explanation for the observed trend in CH content and hydration percentage is the water retention capacity of cellulose nanofibrils, which ensures adequate moisture for the cement hydration process [131]. As the cellulose content increased, the water retention capacity of the mixtures might have increased, leading to a higher degree of cement hydration. Additionally, the presence of cellulose fibers could have provided nucleation sites for the formation of hydration products such as calcium silicate hydrate (C-S-H) and calcium hydroxide (CH) [132]. This may have contributed to the observed increase in CH content and hydration percentage with higher cellulose content. Nevertheless, the decrease in CH content at 1 day for the mixture with 0.3% cellulose could be due to the intricate interplay between cellulose fibers and cement particles, which might potentially postpone the cement hydration process [133]. Despite this observation, the hydration percentage exhibited an overall increase, implying that the net effect of cellulose on hydration was favorable. Further research is required to gain a deeper understanding of these interactions and optimize cellulose content for the desired properties in cementitious materials. impact of cellulose on hydration remained positive.

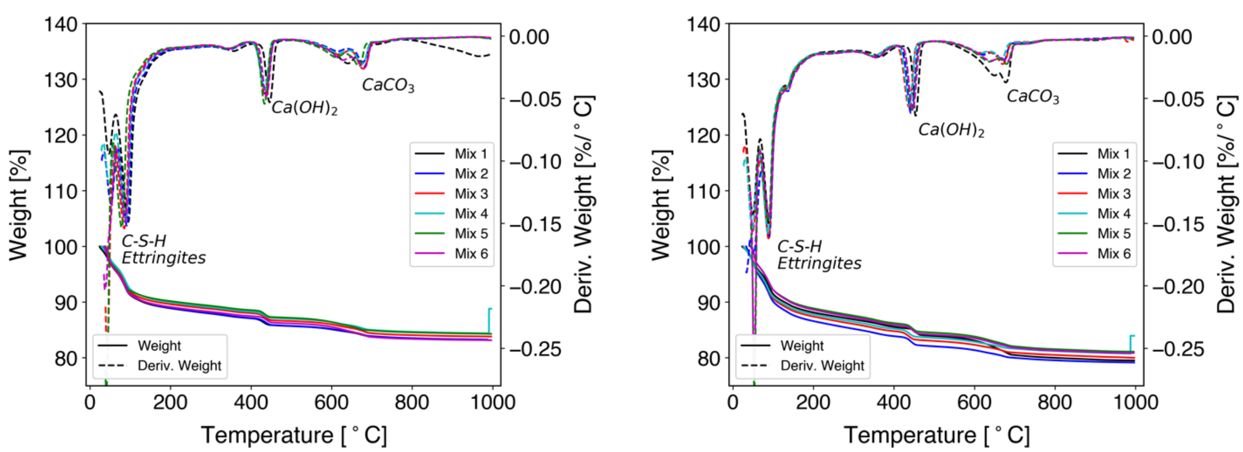

Figure 5-5: Thermogravimetric (TG) and first derivative of TG (DTG) curves for varying CNF concentrations at (a) 1 day and (b) 7 days after casting

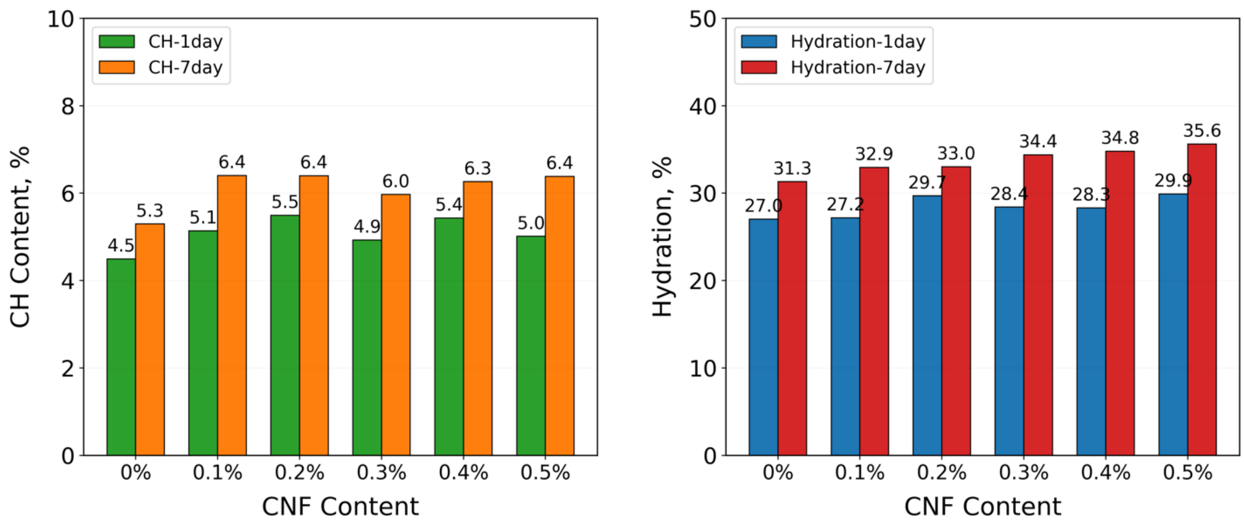

Figure 5-6: (a) CH content in the temperature range between 400 °C and 500 °C and (b) the hydration percentage for the mixtures with varying CNF concentrations at 1 day and 7 days

5.6. Buildability Assessment

To assess buildability, first, a single filament was printed for each mix to characterize the shape retention of the filaments. The printed filaments could not retain their shape for the mixes with no CNF and 0.1% CNF as shown in Figure 5-7a. The large spread of the mixtures suggests that the mixes are not buildable up to 0.1% CNF concentration. The layer breaths were measured as 58 mm and 50 mm, and the layer thicknesses were measured as 3.8 mm and 4.4 mm for the mixes with 0% and 0.1% CNF, respectively (Figure 5-7b). Increasing the CNF concentration to 0.2% provides considerable improvement in shape retention. The layer breadth and thickness are measured as 32 mm 7 mm, respectively. Note that the layer height is set to 7.5 mm, which indicates that the printed filament shows 7% reduction in height compared to the set layer height. The layer thickness is measured as 7.4 mm for the mortar mixture with 0.3% CNF, providing 99% shape retention. Further increasing CNF concentration enables full shape retention in layer height, as the layer heights for 0.4% and 0.5% CNF concentrations are measured as 7.5 mm. Note that the SYS of the mix with 0.3% CNF is measured as 3942 Pa, which suggests that about 4000 Pa of SYS is necessary for a proper shape retention of printed filament. Since the mixes with 0% and 0.1% CNF are not buildable, they are not further considered in the buildability assessment. The mixture with 0.2% CNF lost 7% of the set layer height but is still being further considered together with the mixes with 0.3%, 0.4%, and 0.5% CNF to fully reveal its buildability performance. These four mixes are used to print a single-line wall with multiple layers until failure.

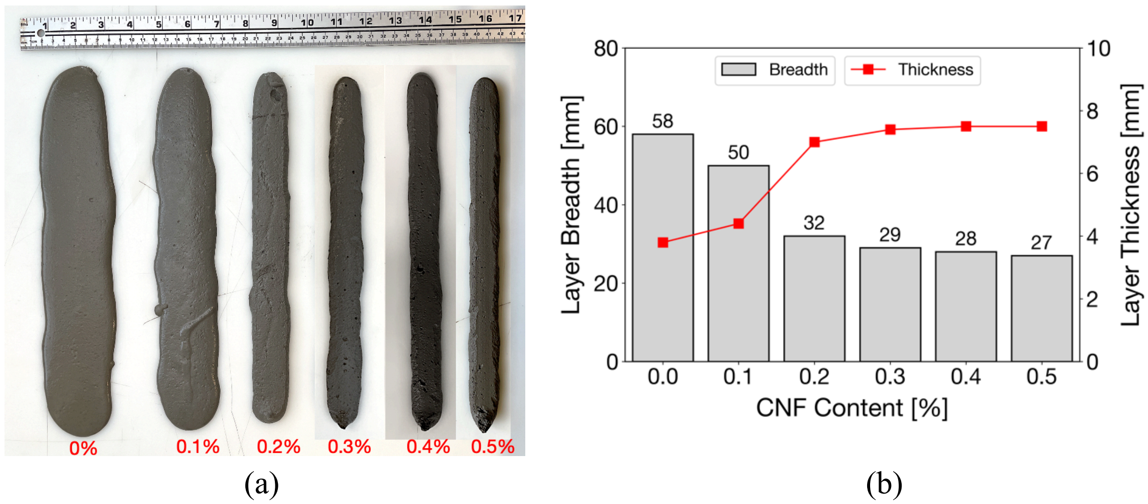

Figure 5-7: (a) Images of single printed filaments of various CNF concentrations, and (b) layer breadth and layer thickness measurements of each filament

Figure 5-8 shows the buildability results for the selected mixes, where the number of printed layers is noted at the bottom of each image. For the mixture with 0.2% CNF, printing the second filament causes considerable spread of the initial filament, which confirms that the SYS of this mixture is not sufficient to hold the weight of the second filament. The more the layers are printed, the more the initial filaments spread. The gradual plastic deformation is observed in the initial layers and complete plastic collapse is observed while printing the 10th layer.

When the CNF concentration is increased to 0.3%, the filaments are observed to retain their shape up to 14th layer. No plastic deformation is observed in the initial layers up to 14th layer as can be visualized from Figure 5-8. However, printing additional layer leads to the failure of the structure. In particular, the printed wall collapses while printing the 15th layer due to buckling induced by the plastic deformation in the initial layer as illustrated in blue circle in Figure 5-8. The mixes with 0.4% and 0.5% CNF show full shape retention where no plastic yielding occur in the initial layers until failure. The printed structures are failed due to pure buckling while printing 24th and 34th layers, for the mixes with 0.4% and 0.5% CNF, respectively. The absence of plastic yielding in the initial layers until failure suggests that with 6457 Pa of SYS (for mix with 0.4% CNF) the printed filaments can withstand the stress from the subsequent layers. It is also worth noting that the maximum number of printed layers are highly correlated with the storage modulus of the mixes. For mixes with 0.4% and 0.5% CNF concentrations, the maximum numbers of printable layers before failure are 23, and 33, and the storage modulus of the mixes are 87 kPa and 117 kPa, respectively. The higher the storage modulus, the more layers can be printed before the structure fails as the failure mode transitions from plastic yielding to pure buckling.

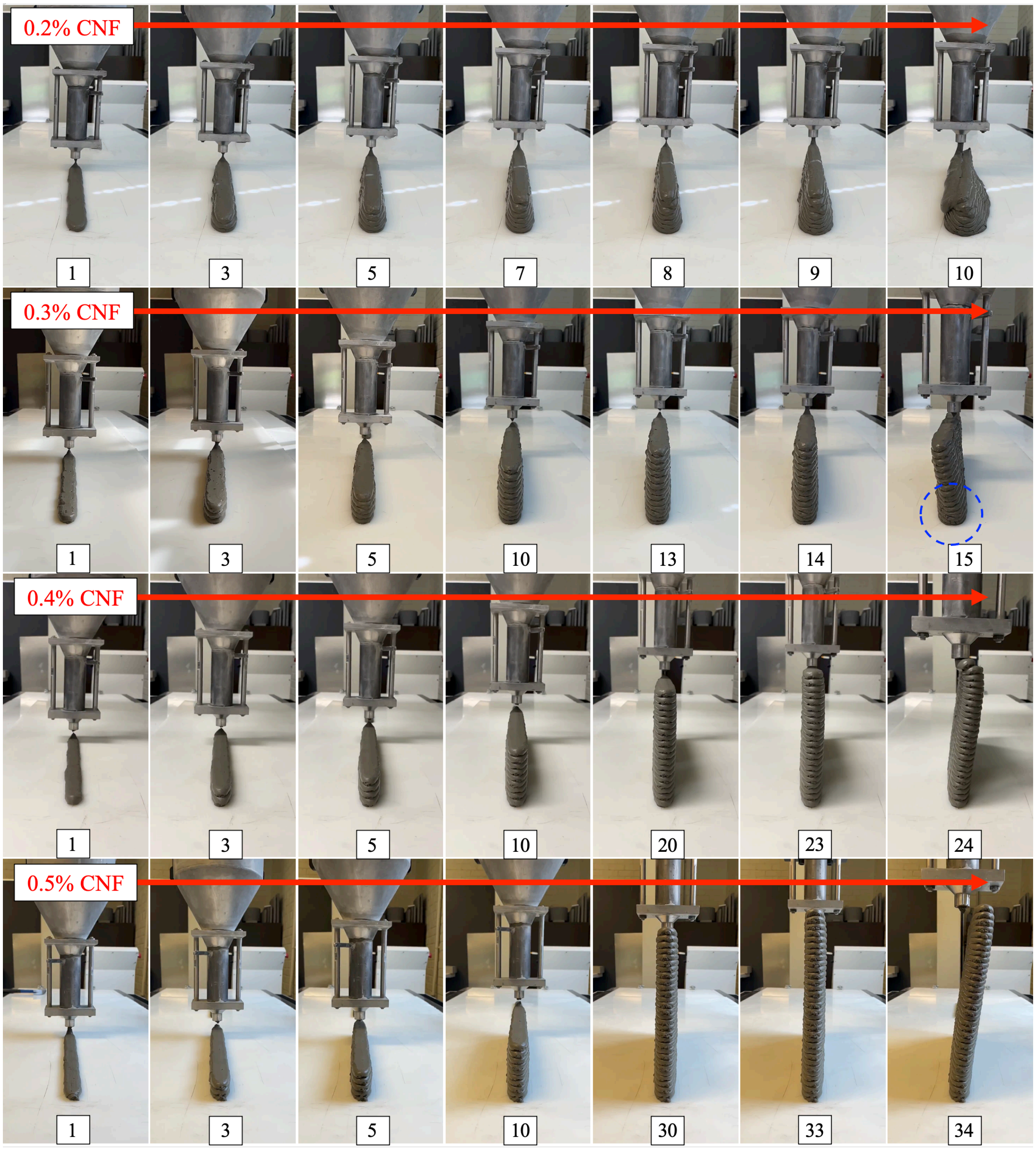

Figure 5-8: Buildability assessment of the mixes with 0.2%, 0.3%, 0.4% and 0.5% CNF concentration

5.7. Mechanical Properties

Since the mixtures with CNF at a ratio of 0.2% or less were not printable, the mechanical assessments were performed on the printable mixtures, i.e., mixtures with CNF ratios of 0.3%, 0.4% and 0.5%. Figure 5-9 shows the tensile strength variation of 3D printed mortar mixtures with CNF at varying concentrations (0.3%, 0.4%, and 0.5%) and under two different loading directions (T1 and T2). Note that T1 loading direction is perpendicular to the printing direction, while the T2 loading direction is parallel to the printing direction. For both test direction, increasing CNF ratio from 0.3% to 0.4% leads to an increase tensile strength. These increases were 14% and 34% for the T1 and T2 loading directions, respectively. However, further increasing the CNF ratio to 0.5% causes a decrease in tensile strength for both directions. For the mixtures with 0.3% CNF and 0.4% CNF, the tensile strength was higher in the T2 loading direction compared to the T1 direction. Note that the specimens for the T1 direction test include multiple depositional interfaces, while the specimens used for the T2 direction testing includes both less interfaces. As the interfaces lead to porosity and defects in the printed specimens, they are more vulnerable to experience failure. The lower tensile strength along T1 direction can be attributed to higher number of interfaces in this specimen compared to those in the specimens for T2 direction.

The initial enhancement in tensile strength with increasing CNF ratio can be attributed to a more compact microstructure and improved crack resistance at the nanoscale [134]. Furthermore, CNF contributes to the bridging of cracks, which helps inhibit the propagation of cracks at the nanoscale. Additionally, the nucleation effect promotes the formation of more C-S-H, resulting in a denser microstructure and overall improvement in mechanical properties for CNF-reinforced mortar. On the other hand, the decrease in tensile strength observed at 0.5% CNF concentration could be attributed to several factors, including fiber agglomeration, increased porosity, and reduced workability of the mortar mix. At higher CNF concentrations, agglomerated fibers, as illustrated in next sub-section with SEM images, form bundles or clusters, which reduce the reinforcing effect of individual fibers in the composite [135]. This weakens the fiber-matrix bond, leading to a decrease in tensile strength.

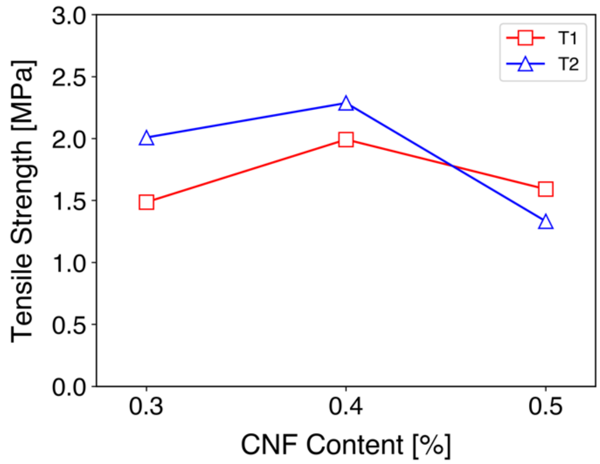

Figure 5-9: Tensile strength of mortar mixtures with varying CNF content

The flexural strength results of CNF reinforced mixtures are presented in Figure 5-10. A trend similar to the one observed in tensile test results is present for the variation of the tensile strength with the CNF ratio. In particular, the mixture with 0.4% CNF demonstrates the highest flexural strength in both loading directions. The flexural strength in the F1 direction increased from 5.92 MPa at 0.3% CNF to 7.45 MPa at 0.4% CNF, indicating a 26% improvement. For the F2 direction, the flexural strength increased from 5.54 MPa at 0.3% CNF to 6.53 MPa at 0.4% CNF, reporting 18% increase. The improvement in flexural strength could be attributed to the flexible cellulose's ability to prevent stress concentration by dispersing energy throughout the bulk material while still allowing micro-cracks to propagate. However, similar to the tensile behavior, the flexural strength decreases at 0.5% CNF concentration. This decrease after 0.4% CNF ratio could again be attributed to the CNF agglomerates present at the higher concentrations.

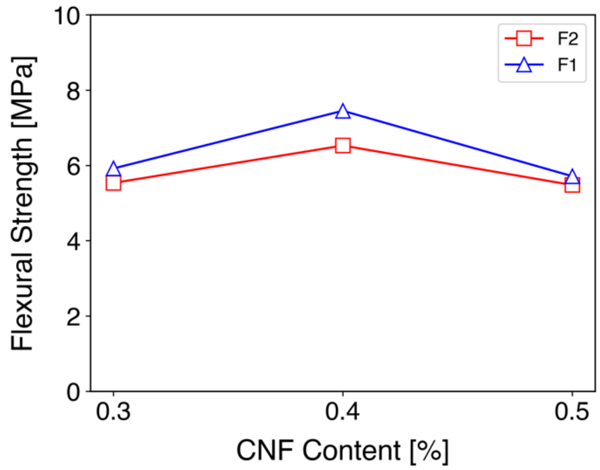

Figure 5-10: Flexural strength of mortar mixtures with varying CNF content

Figure 5-11 shows the compressive strength results of 3D printed mortar mixtures reinforced with varying CNF concentrations. Unlike the tensile and flexural strengths, the 0.3% CNF mixture exhibits the highest compressive strength in both loading directions, with values of 28.9 MPa for C1 and 34.8 MPa for C2. The compressive strength decreases as the CNF concentration increases to 0.4%. In particular, the compressive strengths at 0.4% CNF loading were recorded as 25.7 MPa and 25 MPa, for C1 and C2 loading directions, respectively. Note that as opposed to their beneficial role in tensile and flexural behavior, bridging effects of the fibers is not crticical for compressive response. On the other hand, fiber agglomeration can lead to the formation of weak points in the composite, reducing the overall compressive strength [136].

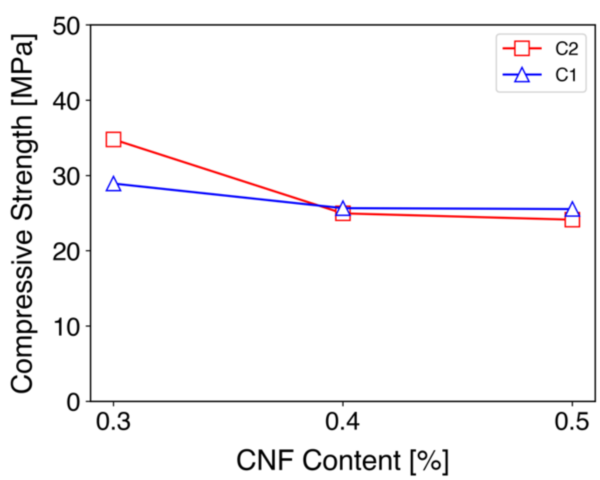

Figure 5-11: Compressive strength of mortar mixtures with varying CNF content

5.8. Microstructural Analysis

The SEM images in **Figure 5-12**a, b, and c reveal the presence of CNF fibers bridging the cement matrix, contributing to improved mechanical properties by providing additional reinforcement and suppressing crack propagation. Notably, even thick and fractured (or cut) CNF fibers, as shown in **Figure 5-12**c and 5-12d, continue to play an important role in maintaining the integrity of the cementitious matrix. However, **Figure 5-12**f, an enlarged image of **Figure 5-12**e, displays clear CNF agglomerations or entanglements in 0.5% CNF reinforced samples, which may explain the decrease in strength observed at higher CNF concentrations. These agglomerations can lead to increased porosity and a less uniform distribution of fibers within the matrix, potentially hindering the mechanical performance. The more porous network created by CNF entanglements reduces the overall load-bearing capacity of the material, emphasizing the need for optimal fiber dispersion to maximize the benefits of CNF reinforcement.

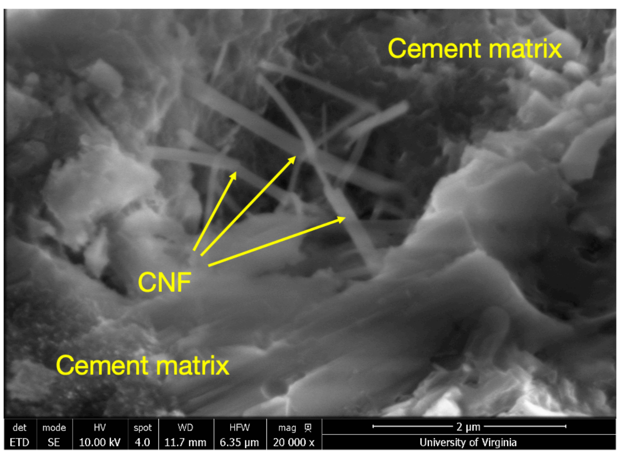

(a)

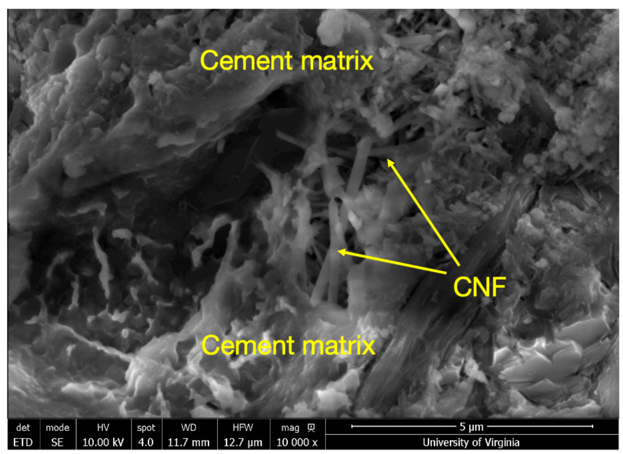

(b)

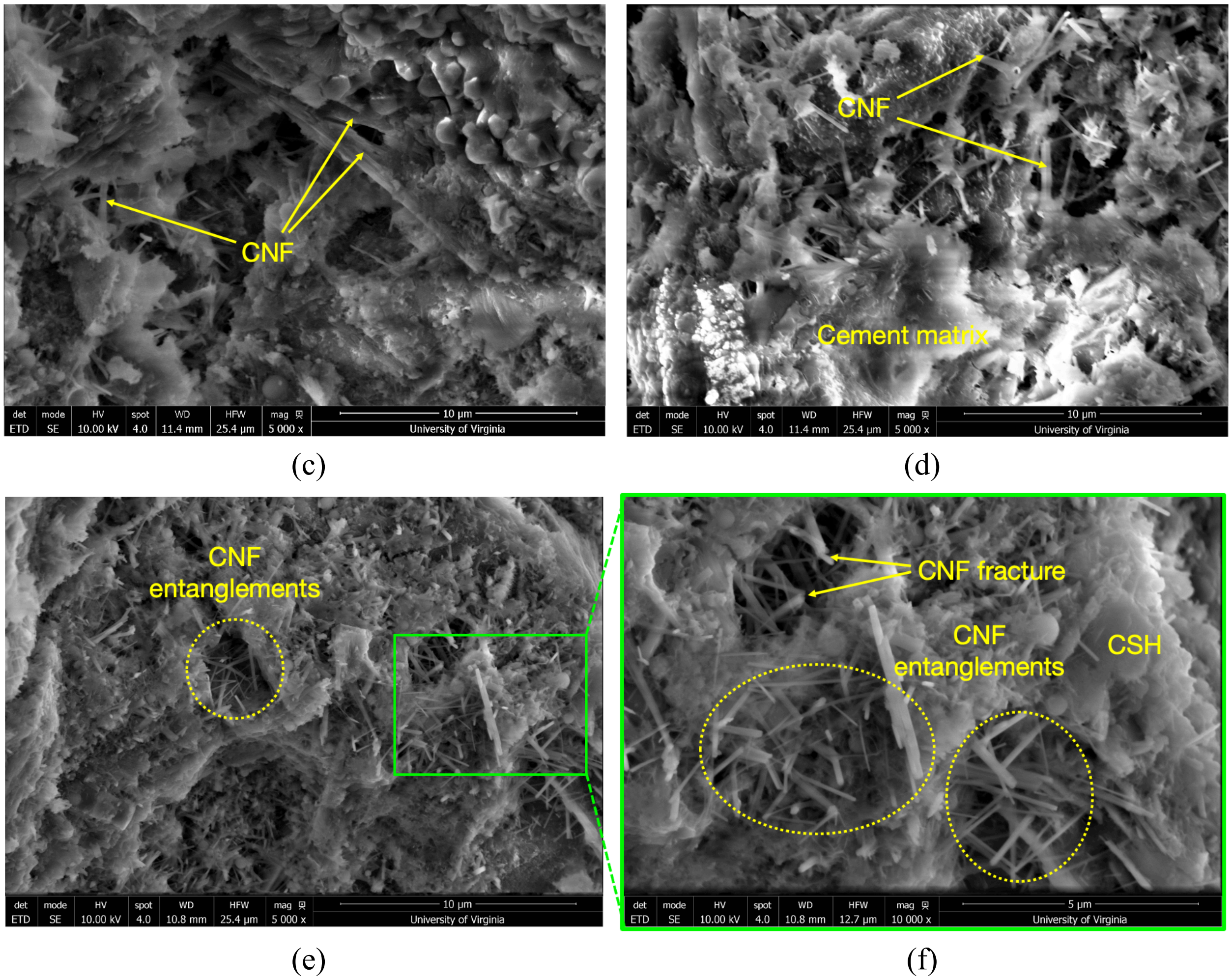

Figure 5-12: SEM images of specimens with; (a) 0.3% CNF that tested on T2, (b) 0.4% CNF that tested on T2, (c) 0.4% CNF that tested on F1, (d) 0.4% CNF that tested on F2, (e) and (f) 0.5% CNF that tested on C1

5.9. Summary

This section investigates the effect of cellulose nanofibers (CNF) on the rheological, printability and mechanical characteristics of cementitious mixtures. The mortar mixtures are prepared with varying CNF ratios as 0%, 0.1%, 0.2%, 0.3%, 0.4% and 0.5%. Rheological properties are assessed using a shear rheometer, and conducting ramp tests, stress growth tests, and amplitude sweep tests. The mixtures were also subjected to thermogravimetric analysis to observe the effect of CNF on hydration characteristics. Mechanical assessment is performed on the printed samples with tensile, flexural and compressive tests. The results can be summarized as follows;

- The static yield stress (SYS) increases significantly with the addition of CNF in the cementitious composites. It increases from 86 Pa for 0% CNF to a maximum level of 10313 Pa for 0.5% CNF. A strong correlation ($R^2 = 0.996$) between CNF concentration and flow behavior is observed with a quadratic best-fitting model.
- The dynamic yield stress (DYS) consistently increases with higher CNF concentrations, with a more rapid increase observed when the CNF ratio is over 0.3%. The plastic viscosity of the mixtures also increases with the addition of CNF, although the rate of increase decreases. The plastic viscosity increases by a factor of 6.8 when the CNF content is increased from 0% to 0.4%. However, further increasing the CNF concentration to 0.5% results in a slight decrease in viscosity. High R^2 values (> 0.98) for quadratic fits indicate strong correlations between CNF concentration and both DYS and plastic viscosity.
- CNF addition significantly impacts cement hydration, generally leading to increased CH content and hydration percentage at both early and later stages, likely due to water retention capacity and the provision of nucleation sites for hydration products. The buildability assessment of cementitious mixtures with varying CNF concentrations reveals that proper shape retention of printed filaments requires around 4000 Pa of static yield stress, with mixes containing 0.3% to 0.5% CNF demonstrating better buildability performance. The maximum number of printable layers before failure is highly correlated with the storage modulus of the mixtures, with a transition in failure mode from plastic yielding to pure buckling as CNF concentration and storage modulus increase.
- Mechanical assessments on printable mixtures (0.3%, 0.4%, and 0.5% CNF) showed that tensile and flexural strengths increased with CNF concentration up to 0.4%, while compressive strength decreased as the CNF concentration increased. The decrease in tensile, flexural, and compressive strengths beyond 0.4% CNF could be attributed to fiber agglomeration, increased porosity, and reduced workability of the mortar mix.

6. Effects of GNP on Rheo-viscoelastic and Mechanical Characteristics of Cementitious Composites

6.1. Overview

This section investigates the effects of graphene nanoplatelets (GNPs) on the rheological and mechanical properties of 3D printable cement-based composites. A bio-based GNP is used to prepare GNP composites with GNP contents at 0%, 0.025%, 0.05%, 0.1%, 0.15%, and 0.2%, where an ultrasonic processor is utilized to disperse GNPs in water with help of superplasticizer (SP). The rheology of the GNP-reinforced mortar mixtures is thoroughly evaluated using a shear rheometer. A ramp test, consisting of a ramp-up and a ramp-down cycles, is conducted to determine the dynamic yield stress and plastic viscosity. A stress growth test is carried out to quantify the static yield stress of the cementitious mixtures. The viscoelastic properties of the mortar mixes, including storage modulus, are determined through amplitude sweep tests. Tensile, flexural and compressive test specimens are fabricated for cast and printed cementitious composites. The mechanical tests are conducted in two directions, which are parallel and perpendicular to the printing direction, to evaluate the effects of process-induced anisotropy in 3D printed specimens. Morphology of GNPs on the fractured surfaces of the composites are also investigated using SEM to help assess the effects of GNPs in the cement matrix.

6.2. Materials and Mixture Preparation

The binder used in this study consists of cement (42%) and supplementary cementitious materials (58%). Type IL Portland limestone cement and calcium sulfoaluminate (CSA) cement are used as cement in this study. Non-crystalline silica fume (SF) and class F fly ash (FA) are utilized as supplementary cementitious materials in the mortar mixes. As fine aggregate, an industrial quartzite sand with a particle size distribution ranging from 0.15 mm to 0.60 mm is used in the cementitious mixtures. A high efficiency polycarboxylate based superplasticizer (SP) is used to enhance workability of the mortar mixes without any segregation. The water to binder ratio (w/b) is kept at 0.25. Table 6-1 shows the proportions of the control mix by percentage of total binder (Portland cement, CSA cement, silica fume, and fly ash).

Table 6-1: Mix proportions of control mix

Materials	Proportions (wt. % of binder)
Portland cement	37.0
CSA cement	5.0
Silica fume	5.0
Fly ash	53.0
Sand	35.0
Water	25
Superplasticizer	1.0

The GNPs used in this study are produced from biomass waste and supplied from GrapheneCR. The GNPs consist of a multi-layer graphene sheet with an average thickness of 6–8 nm and particle diameter ranging between 10 μm and 30 μm. The GNPs are used at ratios of 0.025%, 0.05%, 0.10%, 0.15%, and 0.20% by weight of the binder. The dispersion of GNPs in the water media is usually rather poor, due to their hydrophobic nature that leads to a tendency to form large agglomerates [16, 137]. To improve the dispersion of GNPs, the surfactant-aided sonication method is used in this study. In particular, GNPs are dispersed using a probe sonicator in water where the polycarboxylate-based SP is used as surfactant to improve the stability and dispersion of GNPs.

To prepare GNP-reinforced mortar mixtures, the GNP suspension were prepared first. Around 40% of mixing water was used to sonicate GNPs where the GNP concentrations ranged between 3 and 23 g/L for different mixes as shown in Table 6-2. For all mixes, the SP to GNP ratio was set to be 5. The solution was sonicated such that the total delivered energy was set to 1000 J/ml for all the mixes.

Table 6-2: GNP concentrations for sonication

Mix	GNP Concentration (g/L)
Control	-
GNP-0.025	3
GNP-0.05	6
GNP-0.1	11
GNP-0.15	17
GNP-0.2	23

Once GNP suspension was ready, all the dry mixes were placed into a 20 qt Hobart mixer and mixed for 5 mins at 50 rpm until a homogenous mixture was established. The sonicated GNP solution together with the rest of the mix water and SP was added and the mortar mixture was mixed for 2 mins at 100 rpm. A final mixing at 200 rpm was applied for 3 mins and then the mortar was used to prepare samples for the rheological and mechanical tests.

6.3. Printing Samples for Mechanical Tests

The prepared GNP-reinforced mortar mixtures were printed to prepare specimens for mechanical tests. A rectangular nozzle with a breadth of 20 mm and height of 10 mm was used for printing. The cast specimens were also fabricated to compare their mechanical behavior with the printed specimens. All the mechanical tests were performed after 28 days of curing using a 100 kN capacity MTS machine.

To characterize the tensile behavior of the printed mortars, uniaxial tensile tests were conducted on dog-bone shaped specimens based on the recommendations of the Japan Society of Civil Engineers [106]. Two loading directions were considered; one is perpendicular to the printing direction (T1), and the other is parallel to the printing direction (T2) as shown in Figure 6-1. For loading direction T1, a single-line wall was printed with dimensions of 270 × 20 × 330 mm, and three dog-bone shaped specimens were precisely cut using a water jet. For T2 loading direction, two layers of three side-by-side filaments were printed in 1000 mm long, and similarly three dog-bone shaped specimens were cut.

Four-point bending tests were performed, where 40 × 40 × 160 mm test prisms were utilized according to ASTM C348. To prepare the tests specimens, first a long prism with dimensions of 40 × 40 × 1000 was printed and then samples with the desired dimensions were cut using a water jet. The samples were tested in F1 and F2 loading directions (Figure 6-1) to analyze the anisotropic behavior of the printed samples.

The compressive strength of the specimens was evaluated using 50 × 50 × 50 cubic specimens according to ASTM C109. Two loading directions (C1 and C2) were considered as shown in Figure 6-1 to study the anisotropy in the printed samples. A 350 mm-long prism with five vertical layers and three lateral filaments was printed and six cubic specimens were cut using a water jet, where three of them were tested in C1 direction and the other three were tested in C2.

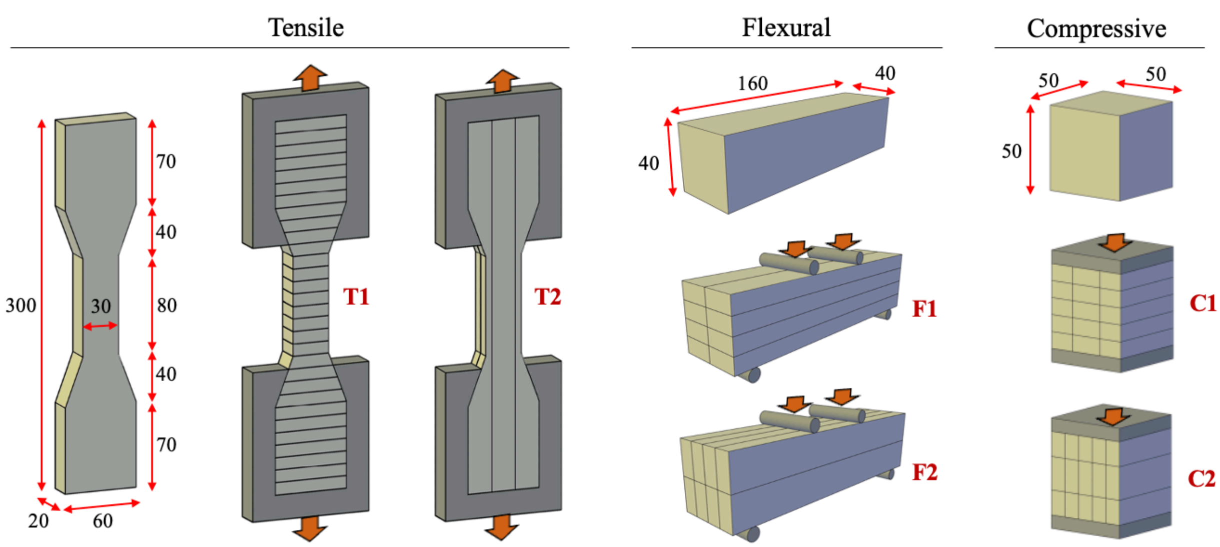

Figure 6-1: Schematic illustration of the loading directions and dimensions of the 3D printed samples for uniaxial tensile, flexural and compressive testing (*all dimensions are in mm*).

6.4. Rheo-viscoelastic Properties

6.4.1. Static Yield Stress (SYS)

The static yield stresses of mortar mixtures were obtained from the stress-growth tests. Figure 6-2 shows the effects of incorporating GNPs at different ratios into mortar mixtures on the SYS. The results indicated that increasing the GNP concentration consistently increased the SYS. A 21%

and 54% increase in the SYS was observed in the mortar mixtures with 0.1% and 0.2% GNPs compared to the control mixture. A high correlation between the GNP concentration and SYS was found with an R^2 value of 0.963, indicating a strong linear relationship between the two variables.

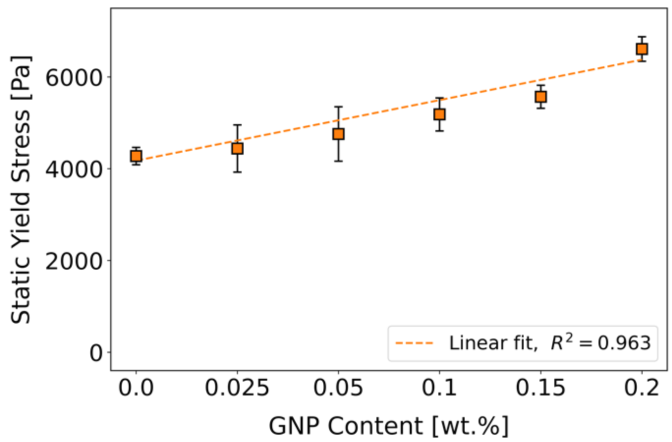

Figure 6-2: Variation of static yield stress (SYS) with increasing GNP concentration

6.4.2. Dynamic Yield Stress (DYS) and Plastic Viscosity

The variation of dynamic yield stress (DYS) and viscosity of the mortar mixtures with GNP content are shown in Figure 6-3. The DYS generally increases with the increasing GNP content, where the measured values range from 682 Pa to 842 Pa. The highest DYS is observed for 0.15% GNP content, which is 24% higher compared to the control mix. Yet, the R^2 for a linear regression fit for the DYS is only 0.59, indicating a moderate correlation between GNP content and dynamic yield stress. On the other hand, the viscosity shows a strong correlation with GNP content with an R^2 value of 0.95 for a linear fit. The addition of GNPs increases the plastic viscosity at a very slow rate. A 10% increase in plastic viscosity is observed when 0.2% GNP content is added.

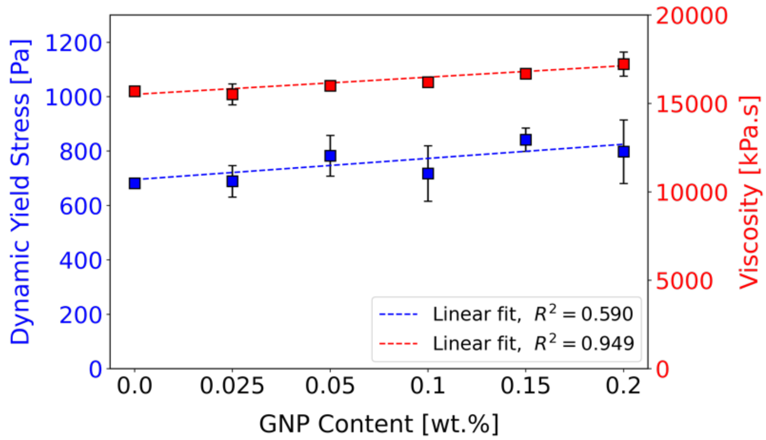

Figure 6-3: Variation of dynamic yield stress (DYS) and plastic viscosity with increasing GNP concentration

6.4.3. Viscoelastic Properties

The storage modulus is an important rheological property that determines the stiffness of a material, and it is an indicator of the material's ability to resist deformation under load. The results of the storage modulus for the 3D printable mortar mixtures incorporating different GNP ratios are shown in Figure 6-4. The storage modulus increases almost linearly with the GNP addition. However, the maximum increase in storage modulus, observed for the mixture with 0.2% GNP, is only 4%. This slight increase in storage modulus can be attributed to the reinforcement provided by the GNP, which enhances the stiffness and rigidity of the matrix. On the other hand, the critical strain slightly decreases with increasing GNP ratios. This can be attributed to the stiffening effect of GNPs, which decreases the linear viscoelastic range of the mixtures.

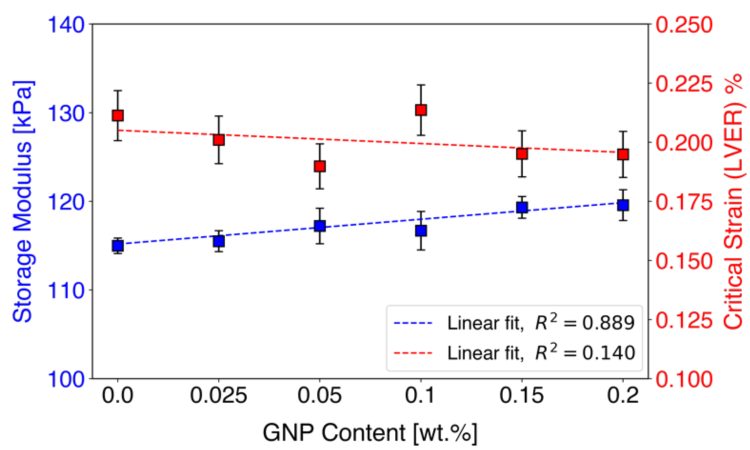

Figure 6-4: Variation of storage modulus, and critical strain with increasing GNP concentration

6.5. Mechanical Properties

6.5.1. Tensile Strength

Figure 6-5a shows the tensile strength of control cast specimen and 3D printed specimens for two different loading directions. The control cast specimen possessed a tensile strength of 2.42 MPa. When the same mixture was printed and specimens were tested in two different directions, the tensile strength decreased considerably. In particular, the printed samples without GNPs showed tensile strength values of 1.03 and 1.67 MPa, respectively in T1 and T2 loading directions. Note that printed specimens consistently have lower tensile strength in the T1 direction compared to the T2 direction. This is because the loading in T1 direction create tensile stresses along the normal direction of bonded interface of the printed layers, which can easily cause interfacial failure. On the other hand, the loading in T2 direction leads shear stresses on the translation interface of printed layers. No significant effect of GNPs was observed in tensile behavior of the printed composites at low concentration levels. At 0.1% GNP concentration, tensile strength increases by 24% and 23% for the loading directions T1 and T2, respectively, compared to the control printed specimen (i.e., printed specimens without GNPs) in the corresponding loading directions. Further increasing the GNP content to 0.15% and 0.2% increases the tensile strength for both T1 and T2 loading directions. The specimen with a GNP concentration of 0.2% attained the highest tensile strength value of 2.68 MPa when it is loaded in T2 direction. Notice that this value was 11% higher than the tensile strength of cast specimen. With the addition of 0.2% GNPs, the tensile strength increases by 55% and 60% for T1 and T2 loading directions, respectively, compared with control cast specimen tested in the same directions.

Figure 6-5b shows the percent changes in the tensile strength when compared to cast and printed specimens without GNP. While there are some initial losses in tensile strength when comparing the printed specimens to the cast specimen, the addition of GNP appears to mitigate these losses and even improve the tensile strength beyond the cast specimen. In particular, as the GNP ratio increased from 0 to 0.2%, a general trend of improving tensile strength can be observed when compared to the cast specimen as seen in Figure 6-5b. It is also worth noting that, the improvements in tensile strength were more pronounced in the T2 loading direction compared to the T1. For instance, at 0.2% GNP content, the tensile strength in the T2 loading direction increased by 60% compared to the control printed, while, the tensile strength in the T1 loading direction showed a smaller increase of 54% compared to the control printed.

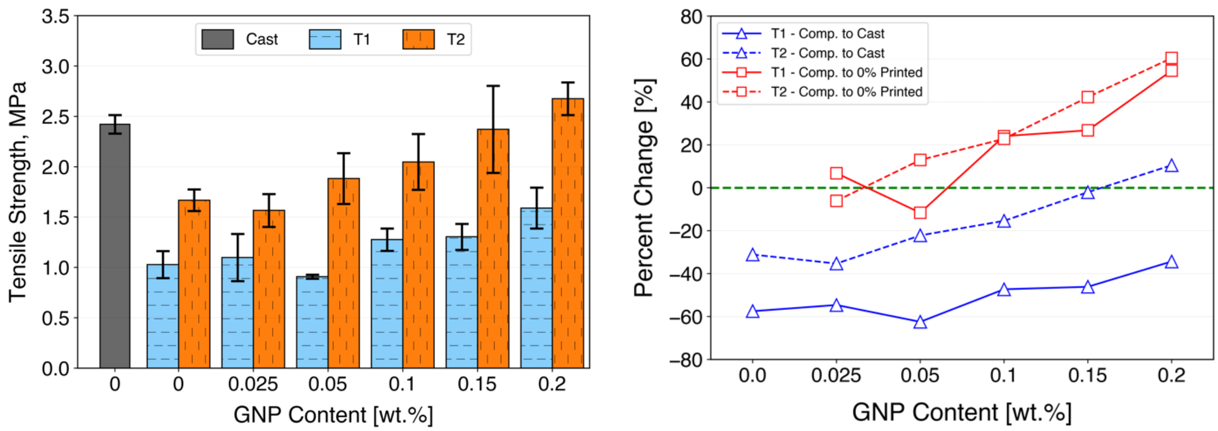

(a) (b)

Figure 6-5: (a) Variation of tensile strength with GNP concentration and (b) percent change of tensile strength with increasing GNP content

Results from the tensile tests indicated that the tensile strength of specimens tested in the T2 loading direction was significantly higher compared to those tested in the T1 loading direction. One possible explanation for this observation could be the orientation of GNPs within the matrix [138]. When the GNPs are aligned parallel to the printing direction, they may provide more effective reinforcement in the T2 loading direction, as they could bridge the interfaces between printed layers and resist shear stresses more effectively [139]. As suggested by Dalla et al. [139] the orientation of GNPs parallel to the neutral plane along which stresses is applied provides the most significant reinforcement. Owing to their planer geometry and good chemical bonding with the cement matrix, GNPs have the ability to transfer the stress to the other positions and relieve the stress concentration in the matrix [16, 140]. In contrast, GNPs lying perpendicular to the neutral plane offer minimal reinforcement, taking up only part of the transverse load arising due to the Poisson effect. Therefore, GNPs' reinforcing effect can be less pronounced in the T1 loading direction, where tensile stresses act normal to the bonded interfaces, leading to a higher propensity for interfacial failure. Additionally, the printing process itself could also contribute to the observed differences in tensile strength between the two loading directions. The layer-by-layer deposition of material during the printing process can lead to anisotropic mechanical properties due to the presence of voids or defects at the interfaces between printed layers [141]. These imperfections can reduce the tensile strength of specimens tested in the T1 loading direction, where failure is more likely to occur along the weaker interfaces.

6.5.2. Flexural Strength

Flexural strength results of the GNP reinforced cementitious composites are shown in Figure 6-6a. The control cast samples showed a flexural strength of 5.15 MPa. The average flexural strength for two loading direction for the control printed samples without any GNPs was only 4% smaller than the flexural strength of the cast specimen. The tensile stresses in the midspan for both loading directions do not align with the normal direction of the bonded interface between printed filaments. Therefore, there was no significant difference between the flexural strength of cast and printed specimens on average. Nevertheless, the specimen loaded in the F1 direction included four deposition interface layers and shear failure of the specimen at these interface layers is more likely with this loading condition. Therefore, the flexural strength at the loading direction F1 is consistently lower than the that of loading direction of F2. This finding is consistent with the finite element (FE) simulations of 3D printed specimens under flexural loading [142].

At low GNP concentrations (0.025% and 0.05%), there was no significant improvement in the flexural strength of the 3D printed samples. Increasing GNP concentration to 0.1% resulted in 7% increase in flexural strength on average for two loading directions compared with the cast specimen. The same increase was 13% compared to the printed specimens without any GNPs. Similar improvements in flexural strength were observed for the specimens with 0.15% and 0.2% GNPs as shown in Figure 6-6b. The highest flexural strength value of 7.3 MPa observed in the F2 loading direction at 0.2% GNP concentration, which indicates 51% and 34% improvement over the control cast and printed specimens, respectively. However, there was higher standard deviation in the test results of these specimens. For the loading direction F1, the flexural strength increased by 14% and 46% for the specimen with 0.2% GNPs compared with the cast and printed specimen without any GNPs.

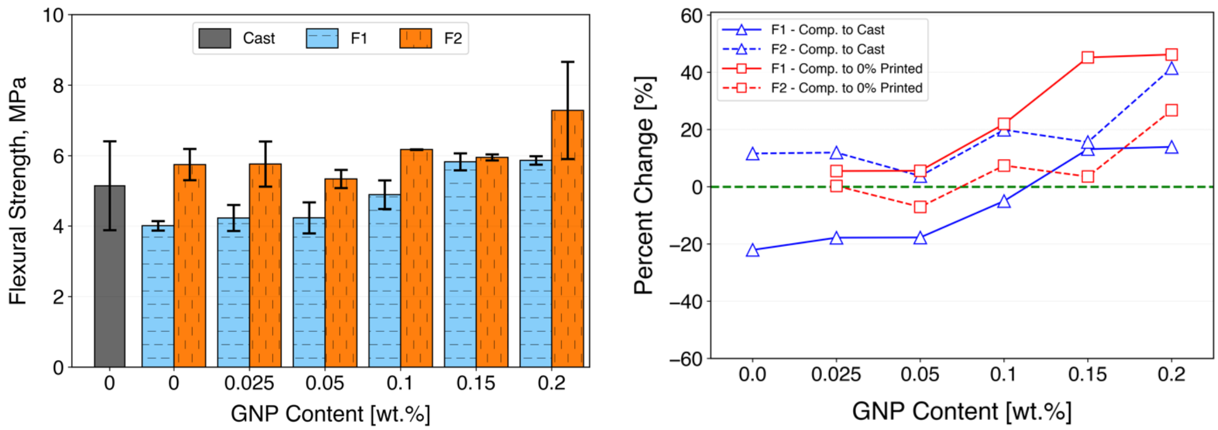

(a) (b)

Figure 6-6: (a) Variation of flexural strength with GNP concentration, and (b) percent change of flexural strength with increasing GNP content

6.5.3. Compressive Strength

Figure 6-7a shows the compressive properties of the cast specimen and 3D printed specimens considering two loading directions. The average compressive strength of the cast specimen was 38.3 MPa. When the compressive strength of the 3D printed specimen without GNP fillers is compared with that of the cast specimens, an average of 24% for two loading directions is noted. This decrease could be attributed to the imperfections such as porosity at the layer interfaces caused by the printing process. A decrease up to 48% in compressive strength in the printed specimens compared to the cast specimen was also reported in the literature [143–146]. The addition of GNPs to the printed specimens at a concentration of 0.025% and 0.05% improved the compressive strength by 8% and 16%, respectively on average for two loading directions. At 0.1% GNP concentration, the compressive strength of the printed specimens increased to 57.41 MPa and 57.43 MPa in the C1 and C2 loading directions, respectively. This was a 50% increase in compressive strength compared with the cast specimen, while it indicates 98% increase compared with the printed specimen without any GNPs on average for two loading directions. Further increasing the GNP content to 0.15% and 0.2% results in a somewhat decrease in compressive strength (Figure 6-7b) compared to the specimens with 0.1% GNPs. However, a 28% and 9% increase in compressive strength was noted for the specimens with 0.15% and 0.2% GNPs compared to the cast specimen. The improvement in compressive strength with GNP addition can be attributed to the nanofiller effects and additional nucleation sites provided by GNPs within the matrix, which improved the overall load transfer and hydration characteristics [147–149]. Nevertheless, increasing the GNP concentration over a certain concentration level makes the dispersion of the nanomaterials more difficult and reduce their effectiveness. Similar results were observed in the literature for the cast GNP-reinforced mortar composites with different GNP ratios [137, 150–152].

For the printed specimen without any GNPs, there was no significant anisotropic effect for two test directions. Similar finding was reported in the detailed FE analysis of printed specimens under compression loading [142]. For the specimens with GNPs, some specimens exhibit higher differences (up to 27% for 0.05% GNP) for the measured value of compressive strength in C1 and C2 directions, while the others have minimal differences (almost 0%). However, relatively higher differences in some GNP-reinforced printed specimens could also be due to the nonuniformity in the effects of GNPs rather than anisotropic effects.

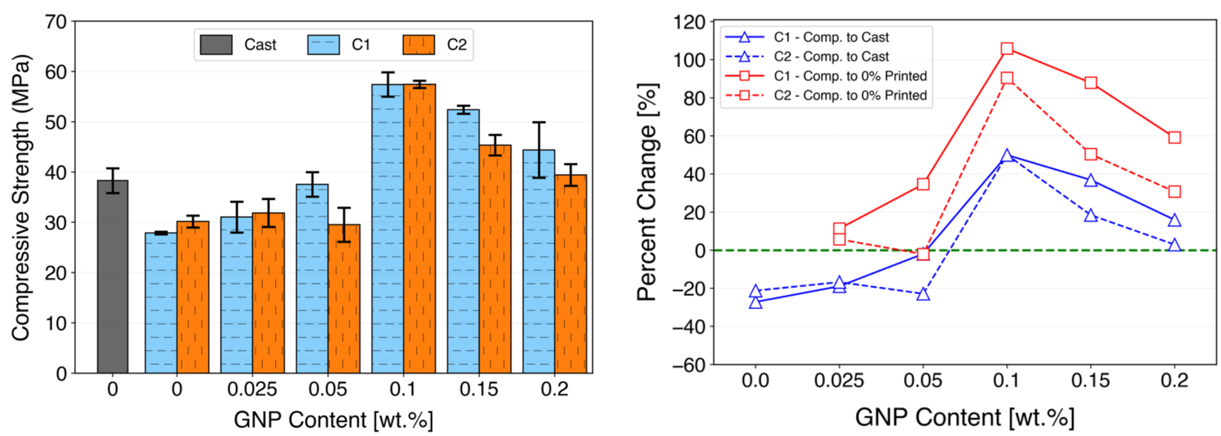

(a) (b)

Figure 6-7: (a) Variation of compressive strength with GNP concentration, and (b) percent change of compressive strength with increasing GNP content

6.6. Microstructural Analysis

The microstructural analysis of GNP-reinforced mortar mixtures was conducted to gain insights into the effects of GNPs in the cement matrix. Scanning electron microscopy (SEM) was employed to examine the fracture surfaces of the specimens after mechanical testing.

Figure 6-8a displays the SEM image of the control specimen (0% GNP). In the control sample, a large volume of porosity is evident, along with small needle-like and rod-shaped cement hydration products such as AFt and C-S-H gel. Additionally, wide and large microcracks up to 50 micrometers are visible in the control sample. Previous research has shown that graphene nanoparticles can fill voids, enhance the growth of hydration products, and alter the size and shape of hydration crystals without changing their type by reacting with cement and graphene [153].

As seen in Figure 6-8b, compared to control specimen, the specimens with GNPs (0.1%) have denser hydration products and a more consistent microstructure. The intersecting microcrystals significantly improve the mechanical properties of the concrete. It is also worth noting that with the addition of GNPs, the needle-like crystals are hardly seen in the SEM images. In the specimens with 0.1% GNP content (Figure 6-8c), a good distribution of graphene nanoparticles is observed. This well-dispersed GNP distribution leads to a more homogeneous and compact microstructure. Additionally, in Figure 6-8d, C-S-H gels were observed on GNP flakes, suggesting that GNPs serve as nucleation sites for the growth of C-S-H on their surfaces. Also, a single GNP flake was visible in this SEM and its size was measured as 22 microns. To generalize this, the flake sizes were measured to be less than 25 micrometers up to 0.1% GNP concentration, indicating a good distribution and dispersion of GNPs within the mortar mixture.

However, it should be noted that when the GNP content is further increased, GNPs and other concrete materials may not mix well, leading to uneven distribution and GNP aggregation. In Figure 6-8e, the SEM image of a 0.1% GNP-reinforced mortar tested under the C1 loading direction showed good dispersion and microstructural features. Conversely, Figure 6-8f revealed the presence of large GNP agglomerates, approximately 65 microns in size, for the mixture with 0.2% GNPs. This could help explain the poor dispersion quality and subsequent decrease in compressive strength observed in this specimen. These findings suggest that the GNP dispersion quality and agglomerate size play crucial roles in determining the mechanical properties of GNP-reinforced mortar mixtures, emphasizing the need for effective dispersion techniques and optimal GNP concentrations.

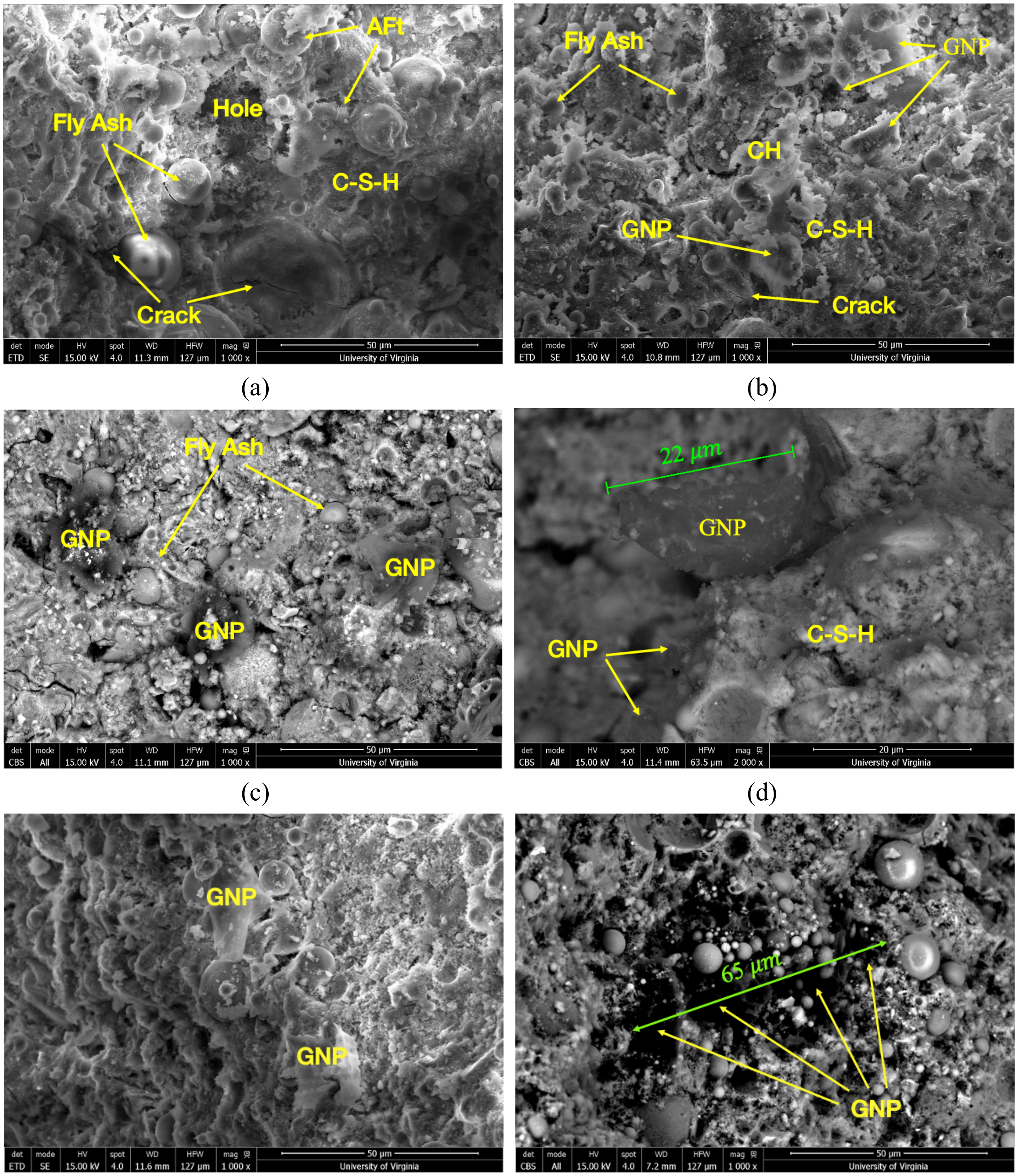

Figure 6-8: SEM images of specimens with; (a) 0% GNP, (b) 0.1% GNP that tested on T2, (c) 0.1% GNP that tested on F1, (d) 0.1% GNP that tested on F2, (e) 0.1% GNP that tested on C1, and (f) 0.2% GNP that tested on C1

6.7. Summary

This section is focused on exploring the impact of graphene nanoplatelets (GNPs) on the rheological and mechanical properties of 3D printable cementitious composites. The mortar mixtures with varying GNP contents, ranging from 0% to 0.2%, was prepared. The GNPs were sonicated in a water-SP solution before being incorporated into the mortar mixtures. Fresh and hardened properties of GNP-reinforced cementitious composites were evaluated. The findings of this study can be summarized as follows:

- As the GNP concentration increased, the SYS also increased, with the highest improvement observed at 0.2% GNP. For this mixture, there was 54% increase in SYS compared to the control mixture without any GNP. A strong linear relationship between GNP concentration and static yield stress was found, with an R^2 value of 0.963, indicating that the incorporation of GNP can predictably improve the SYS of the 3D printable cementitious mixtures.
- With increasing GNP content, DYS increased from 682 Pa to 842 Pa, with a moderate correlation (R^2 = 0.59). Viscosity showed a stronger correlation with GNP content (R^2 = 0.95) and constantly increased with GNP content, with the largest increase of 10% observed at 0.2% GNP. The addition of GNPs increased the SYS in a more pronounced way compared with the DYS and plastic viscosity.
- The storage modulus of the base mix (0% GNP) was 114.9 kPa and only slightly (4%) increased when 0.2% GNP was added. These slight improvements in viscoelastic properties of mortar mixtures can be attributed to the stiffening effect of GNP, which enhances the stiffness and rigidity of the matrix and resists plastic deformation under load.
- The tensile strength of 3D printed mortar specimens was found to be significantly influenced by both the loading direction and GNP concentration. The tensile strength of the printed specimens was consistently higher in T2 loading direction compared to the T1 loading direction, which can be attributed to the inherent anisotropic mechanical properties induced by the layer-by-layer printing process. The printed specimens without any GNPs exhibited considerably lower tensile strength compared to the cast specimen. The addition of GNPs effectively mitigated the tensile strength losses observed in printed specimens and

even increased the tensile strength by up to 11% compared to the control cast specimens when GNP concentration was 0.2%.

- The flexural strength of printed composites without any GNPs was lower than cast specimen in the F1 direction and higher in the F2 direction. The same trend was mostly present for the GNP reinforced cementitious composites. However, the addition of GNPs improved the flexural strength of the printed specimens in both directions. For GNP concentration of 0.2%, the maximum improvement in flexural strength reached 51% compared to the control cast specimen.
- The compressive strength of cast specimens was higher than the printed specimen with 0%, 0.025%, and 0.05% GNPs. However, at a GNP concentration of 0.1%, the compressive strength increased by 50% compared to the cast specimen and 98% compared to the printed specimen without any GNPs. Further increases in GNP content to 0.15% and 0.2% resulted in slightly decreases in compressive strength compared to specimens with 0.1% GNPs, yet still showed improvement over the cast and printed specimen. For the printed specimens without any GNPs, there was no significant anisotropic effect for the two test directions. However, some GNP-reinforced printed specimens exhibited higher differences in compressive strength between the two loading directions, potentially due to nonuniformity in the effects of GNPs rather than anisotropic effects.

7. Effects of PE fibers on Rheo-viscoelastic and Mechanical Characteristics of Cementitious Composites

7.1. Overview

This section investigates the effects of polyethylene (PE) fibers on the rheological and mechanical properties of 3D printable cement-based composites. PE fibers are incorporated into cementitious composites with fiber contents of 0%, 1.0%, 1.2%, 1.4%, 1.6%, and 1.8%. The rheology of the PE fiber-reinforced mortar mixtures is thoroughly evaluated using a shear rheometer. A stress growth test is carried out to quantify the static yield stress (SYS) of the cementitious mixtures. A ramp test is conducted to determine the dynamic yield stress (DYS) and plastic viscosity. The viscoelastic properties of the mortar mixes, including storage modulus and critical strain, are determined through amplitude sweep tests. Mechanical tests, including tensile, flexural, and compressive tests, are conducted in two directions, parallel and perpendicular to the printing direction. Digital Image Correlation (DIC) is employed during the mechanical tests to provide additional insight into the material behavior and deformation characteristics. Morphology of PE fibers on the fractured surfaces of the composites is investigated using Scanning Electron Microscopy (SEM) to help assess the dispersion of fibers in the cement matrix and their influence on the composite performance.

7.2. Materials and Mixture Preparation

In this study, the binder comprises 42% cement and 58% supplementary cementitious materials. Type IL Portland limestone cement and calcium sulfoaluminate (CSA) cement serve as the cementitious components. Non-crystalline silica fume (SF) and class F fly ash (FA) are utilized as supplementary cementitious materials in the mortar mixtures. An industrial quartzite sand with a particle size distribution from 0.15 mm to 0.60 mm is employed as the fine aggregate. A high-performance polycarboxylate-based superplasticizer (SP) is incorporated to improve the workability of the mortar mixes without causing segregation. The water-to-binder ratio (w/b) is maintained at 0.25. Table 7-1 shows the proportions of the control mix.

Table 7-1: Mix proportions of control mix

Materials	Proportions (wt. % of binder)
Portland cement	37.0
CSA cement	5.0
Silica fume	5.0
Fly ash	53.0
Sand	35.0
Water	25
Superplasticizer	1.0

PE fibers, provided by MiniFIBERS, Inc., with a standard filament size of 6.0 denier per filament (dpf) and a standard cut length of 6 mm, are incorporated as reinforcement in the cementitious composites. The PE fibers are used at ratios of 0%, 1%, 1.2%, 1.4%, 1.6% and 1.8% by volume of the mortar. For mixing procedure, all the dry constituents are first blended in a 20 qt Hobart mixer for 5 minutes at 50 rpm, resulting in a uniform mixture. Subsequently, the necessary quantity of water and SP is combined and introduced to the dry mixture. The mortar mix is stirred for 2 minutes at 100 rpm. After this stage, the PE fibers are progressively added to the mix over a span of 3 minutes, ensuring their even dispersion. Following the addition of PE fibers, a final mixing at 200 rpm for 3 minutes is performed to guarantee the comprehensive and uniform distribution of the PE fibers throughout the mortar mixture. After completing the mixing process, the mortar is utilized to create samples for rheological and mechanical testing.

7.3. Mechanical tests

The prepared PE fiber-reinforced mortar mixtures were printed to prepare specimens for mechanical tests. A rectangular nozzle with a breadth of 20 mm and height of 10 mm was used for printing. The cast specimens were also fabricated to compare their mechanical behavior with the printed specimens. All the mechanical tests were performed after 28 days of curing using a 100 kN capacity MTS machine.

To characterize the tensile behavior of the printed mortars, uniaxial tensile tests were conducted on dog-bone shaped specimens based on the recommendations of the Japan Society of Civil

Engineers [106]. Two loading directions were considered; one is perpendicular to the printing direction (T1), and the other is parallel to the printing direction (T2) as shown in Figure 7-1. For loading direction T1, a single-line wall was printed with dimensions of 270 × 20 × 330 mm, and three dog-bone shaped specimens were precisely cut using a water jet. For T2 loading direction, two layers of three side-by-side filaments were printed in 1000 mm long, and similarly three dog-bone shaped specimens were cut.

Four-point bending tests were performed, where 40 × 80 × 300 mm test prisms were utilized according to ASTM C1609. To prepare the tests specimens, first a long prism with dimensions of 40 × 80 × 1000 was printed and then samples with the desired dimensions were cut using a water jet. The samples were tested in F1 and F2 loading directions (Figure 7-1) to analyze the anisotropic behavior of the printed samples.

The compressive strength of the specimens was evaluated using 50 × 50 × 50 cubic specimens according to ASTM C109. Two loading directions (C1 and C2) were considered as shown in Figure 7-1 to study the anisotropy in the printed samples. A 350 mm-long prism with five vertical layers and three lateral filaments was printed and six cubic specimens were cut using a water jet, where three of them were tested in C1 direction and the other three were tested in C2.

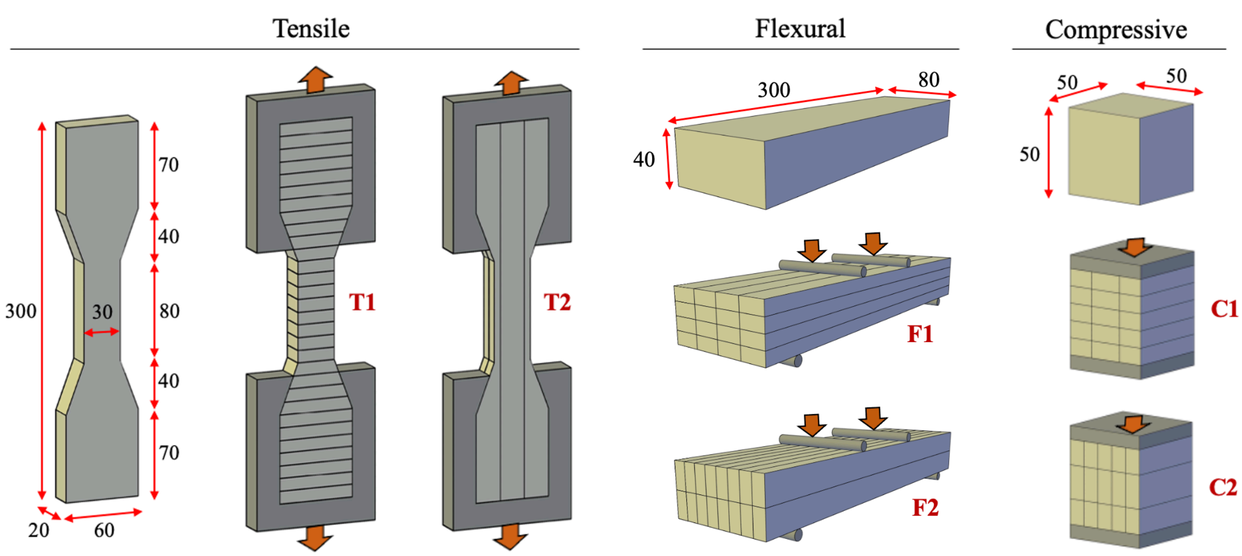

Figure 7-1: Schematic illustration of the loading directions and dimensions of the 3D printed samples for uniaxial tensile, flexural and compressive testing (all dimensions are in mm).

7.4. Rheo-viscoelastic Properties

7.4.1. Static Yield Stress (SYS)

The results from stress-growth tests indicate a rapid increase in SYS as the percentage of PE fibers increases as can be seen from the flow curves in Figure 7-2a. The SYS values were calculated from the flow curves and are presented in Figure 7-2b. A 27% increase in SYS was observed when 1% PE fibers were added to the mortar mixture, compared to the control sample. When the PE fiber content was increased to 1.4% and 1.8%, the increase in the SYS compared to the control mixture was 116% and 224%, respectively. The observed increases in SYS can be attributed to the strong fiber-matrix bonding and the bridging effect provided by the PE fibers, which enhances the load-carrying capacity between the cement matrix and fibers and internal structure of the mortar mixtures [154]. Furthermore, the fibers help to distribute stresses more evenly throughout the material, thus increasing the overall resistance to deformation [155].

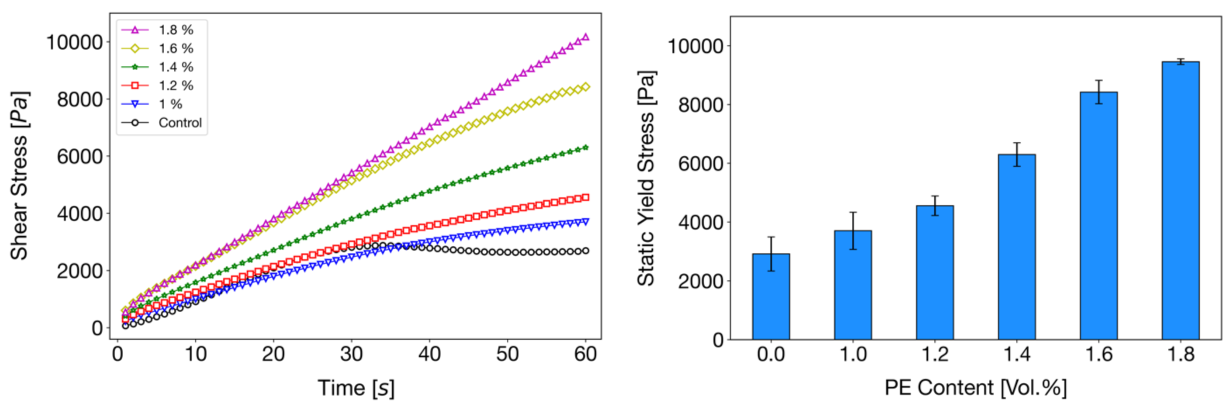

(a) (b)

Figure 7-2: (a) Flow curves, and (b) static yield stress of the mixes with increasing PE content

7.4.2. Dynamic Yield Stress (DYS) and Plastic Viscosity

The flow curve results from the ramp-up and ramp-down tests (Figure 7-3) provide valuable insights into the rheological behavior of cementitious mixtures with varying concentrations of PE fibers. For lower PE concentrations, the flow curves exhibit a relatively straight trend, indicating a stable and consistent rheological behavior. However, as the PE content is increased, the variation in the flow curves becomes more pronounced, especially at lower shear rates, resulting in increased irregularity in the flow curves. This increased variation in the flow curves with higher PE content can be attributed to the interaction between the PE fibers and the cementitious matrix. At higher PE concentrations, the fibers are more likely to create physical networks and entanglements within the matrix, leading to increased resistance to flow and shear-thinning behavior at lower shear rates [156]. This phenomenon can result in the observed wiggly lines in the flow curves, reflecting the complex rheological behavior of the cementitious mixtures with higher PE fiber content.

On the other hand, at higher shear rates, the applied forces can break up these aggregated structures, leading to a more dispersed and homogeneous distribution of PE fibers and cement particles. The underlying cause for this behavior can be that the structure of PE fibers is disorganized and exhibits high viscosity when subjected to low or static shear rates. Conversely, when exposed to high shear rates, the fibers become more ordered and align parallel to the direction of the shear force, resulting in easier movement and reduced viscosity [157].

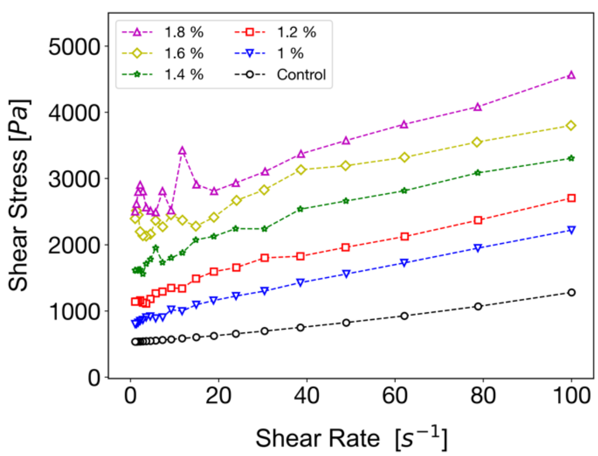

(a)

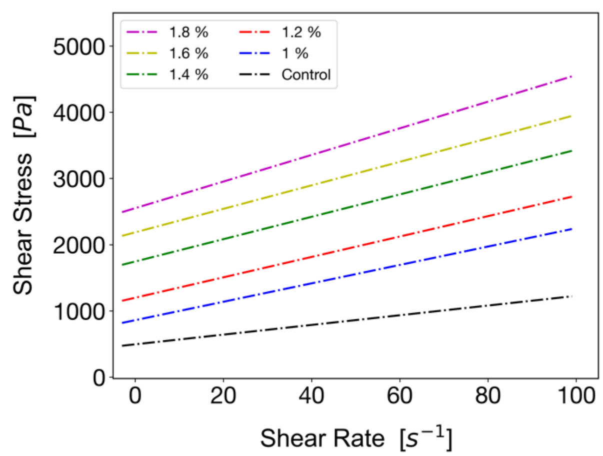

(b)

Figure 7-3: (a) Flow curves and (b) Bingham model fits on the flow curves for mixes with various PE content

DYS and plastic viscosity results are calculated using Bingham model and the results are represented in Figure 7-4. The results demonstrate a significant increase in both DYS and plastic viscosity as the percentage of PE fibers increases. When 1% PE fibers were added to the mortar mixture, the DYS increased by 60%, while the viscosity experienced a 48% increase compared to the control sample. Moreover, the addition of 1.8% PE fibers resulted in a 385% increase in DYS and a 98% increase in viscosity compared to the control. These findings suggest that the incorporation of PE fibers at higher concentrations can lead to rapid increases and very high values for plastic viscocity and DYS, which is disadvantageous for the extrudability of the mixtures. The observed increases in DYS and viscosity can be attributed to the strong fiber-matrix bonding, the bridging effect provided by the PE fibers, and the more uniform distribution of stresses within the material [158]. These factors contribute to the overall resistance to deformation and flow, which are essential for the stability and workability of the cementitious mixtures during construction.

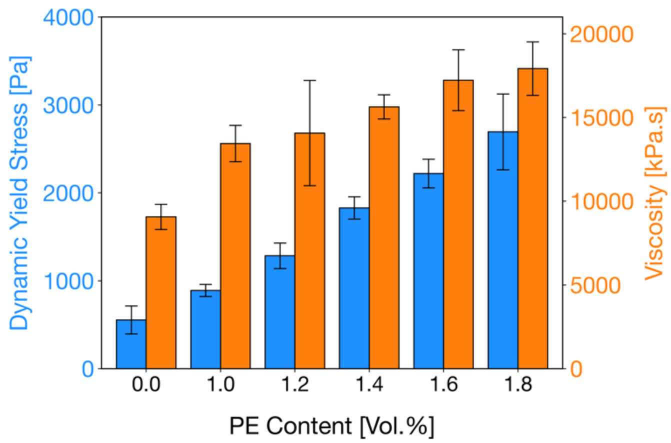

Figure 7-4: Variation of dynamic yield stress (DYS) and plastic viscosity with increasing PE content

7.4.3. Viscoelastic Properties

The storage modulus is an indicator of the material's ability to store elastic energy under deformation and is a critical parameter for evaluating the stiffness and resistance to deformation of the mixtures. Figure 7-5 shows the variation in storage modulus and critical strain with increasing PE concentration. As the percentage of PE fibers increased, a notable increase in the storage modulus was observed. When 1% PE fibers were incorporated into the mortar mixture, the storage modulus increased by 17% compared to the control sample. Further increasing the PE fiber ratio to 1.8% led to a 170% increase in the storage modulus relative to the control. A higher storage modulus indicates that the cementitious mixture has a greater ability to store elastic energy and resist deformation under applied stress. This increased stiffness ensures that the printed layers maintain their shape and do not deform or collapse under the weight of the subsequent layers. This characteristic is important for the buildability of 3D printed concrete structures, as it ensures the stability of the printed layers and prevents structural failures during the printing process.

Similarly, critical strain is an essential parameter for assessing the material's capacity to undergo deformation before failure. The results (from Figure 7-5) indicate that as the percentage of PE fibers increased, the critical strain of the cementitious mixtures also increased. For instance, when 1% PE fibers were added, the critical strain increased by 89% compared to the control sample. Similarly, the addition of 1.8% PE fibers resulted in a 122% increase in critical strain relative to the control. In 3D concrete printing, the buildability and structural integrity of the printed layers are dependent on the material's ability to withstand the stress and strain imposed by the weight of the subsequent layers. A higher critical strain implies that the material can accommodate more deformation before yielding or failing, which is essential for maintaining the stability and structural integrity of the printed structure during the printing process.

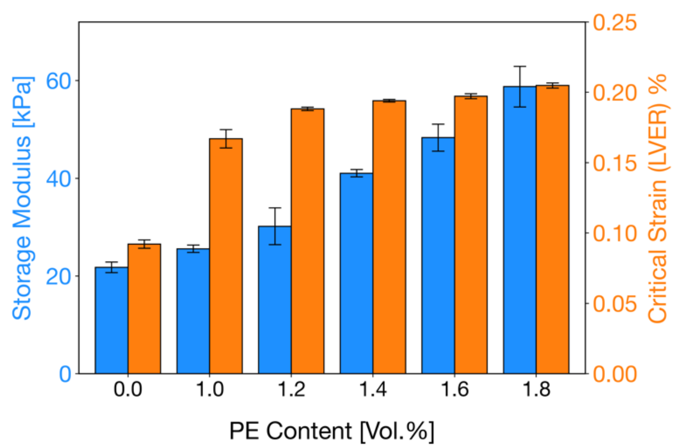

Figure 7-5: Variation of storage modulus and critical strain with increasing PE content

7.5. Mechanical Properties

7.5.1. Tensile Strength

The influence of PE fibers on the tensile properties of 3D printed cementitious mixtures was investigated and the results are represented in Figure 7-6. The tensile strength results, presented in Figure 7-6a, show a clear distinction between the cast control sample and the 3D printed samples. In particular, the cast control sample exhibited a tensile strength of 3.28 MPa, while the printed control samples had tensile strengths of 1.10 MPa and 2.09 MPa for the T1 and T2 directions, respectively. This difference in tensile strength can be attributed to the layer-by-layer deposition process in 3D printing, which can result in weaker interlayer bonding compared to the cast sample. In addition, T1 loading direction generates tensile stresses perpendicular to the bonded interface of the printed layers, which can readily result in interfacial failure. Conversely, the T2 loading direction induces shear stresses on the translation interface of the printed layers. Therefore, the tensile strength in the T1 direction was lower than that of T2 direction for the printed specimen without any fibers. As the percentage of PE fibers increased, the tensile strength of the printed samples significantly improved in the T2 direction. The decrease in the tensile strength in the control printed specimens was recovered with 1% PE addition in T2 loading direction. Further increasing PE fiber amount positively affected the tensile strength in T2 loading direction. The tensile strength increased by 124% compared to the control printed sample and reached at 4.69 MPa for the 1.6% PE fiber sample in the T2 direction. This improvement can be attributed to the enhanced fiber-matrix bonding, alignment of fibers in the printing direction (which is parallel to T2), bridging effect provided by the PE fibers, and more uniform distribution of stresses within the material, leading to improved tensile strength and overall structural performance of the 3D printed cementitious mixtures. However, the tensile strength in the T1 direction did not have considerable change or slightly decreased with increasing PE content, which could be due to fiber orientation and alignment between the subsequent layers. This fiber orientation may result in a reduced bridging effect and weaker stress transfer between the fibers and the matrix in the T1 direction.

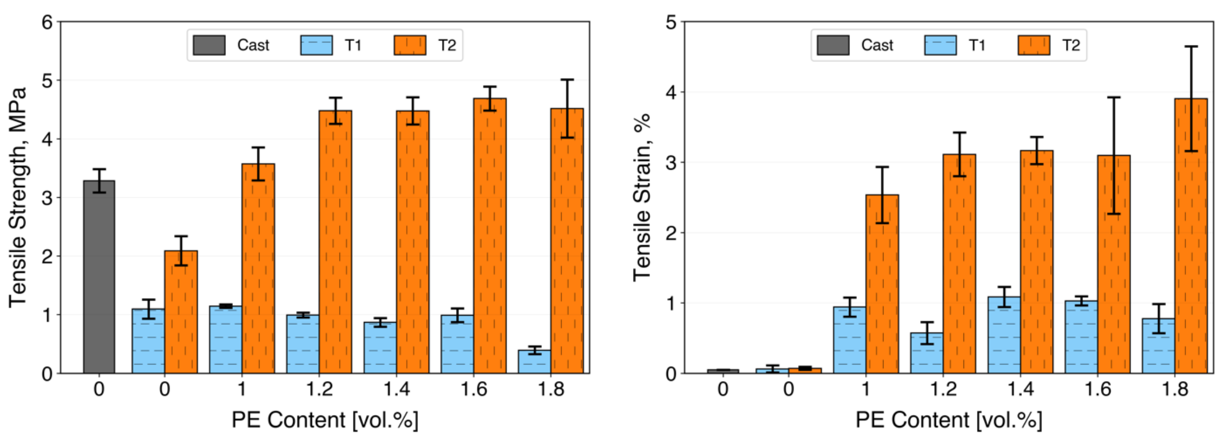

(a) (b)

Figure 7-6: (a) Tensile strength and (b) ultimate tensile strain variation with increasing PE content

Furthermore, the influence of the PE fibers on the ultimate tensile strain of the 3D printed cementitious mixtures was examined and results are shown in Figure 7-6b. The tensile strain results reveal that the cast control sample had a tensile strain of 0.05%, while the printed control samples showed tensile strains of 0.06% and 0.07% for the T1 and T2 directions, respectively. As the percentage of PE fibers increased, the tensile strain of the printed samples also improved, particularly in the T2 direction. For example, the tensile strain increased from 0.07% for the control printed sample to 3.90% for the 1.8% PE fiber sample in the T2 direction. This enhancement in tensile strain can be attributed to the strong fiber-matrix bonding, increased resistance to crack propagation provided by the PE fibers, and the more uniform distribution of stresses within the material. Consequently, the incorporation of PE fibers can significantly improve the tensile strain of 3D printed cementitious mixtures, providing enhanced ductility and resistance to failure, which are crucial for the performance of these materials in various applications. On the contrary, the tensile strain in the T1 direction decreased as the PE fiber content increased. The highest tensile strain in the T1 direction was observed for the 1.4% PE fiber sample, with a value of 1.09%. This variation in tensile strain for the T1 direction could be attributed to less effective stress transfer between the fibers and the matrix or the fiber orientation, leading to reduced ductility and resistance to failure in this direction. As the cementitious mixtures are extruded layer by layer, the fibers have a tendency to orient in the printing direction, which is parallel to the layers. Consequently, when the samples are tested in the T1 direction, the fibers are oriented perpendicular to the applied tensile force, which diminishes their ability to contribute to the bridging effect. In other words, when fibers are oriented perpendicular to the direction of the applied force, they are less effective at transferring stresses and providing reinforcement to the matrix. This leads to a reduction in tensile strength in the T1 direction, as the fibers are not optimally positioned to counteract the applied tensile forces.

The tensile strain-stress behavior of the cementitious composites which are tested on T1 loading direction was presented in Figure 7-7. In T1 direction, which corresponds to the test perpendicular to the layer interface, generally a brittle failure without any microcracking was observed. This outcome is in line with previous research that has reported fibers oriented perpendicular to the direction of the applied force are less effective in transferring stresses and providing reinforcement to the matrix [159, 160]. It is worth noting that in 3D printed concrete structures, the layer interfaces are considered to be the most vulnerable points [43]. This vulnerability arises from the fact that the breadth of the interface could be narrower than the breadth of the layer itself, leading to weaker bonding between the layers and consequently a higher inclination to failure [85]. Therefore, the absence of microcracks in the T1 direction suggests that the PE fibers are not significantly contributing to the reinforcement of the layer interface, highlighting the importance of the fiber orientation for the performance in 3D printed cementitious composites.

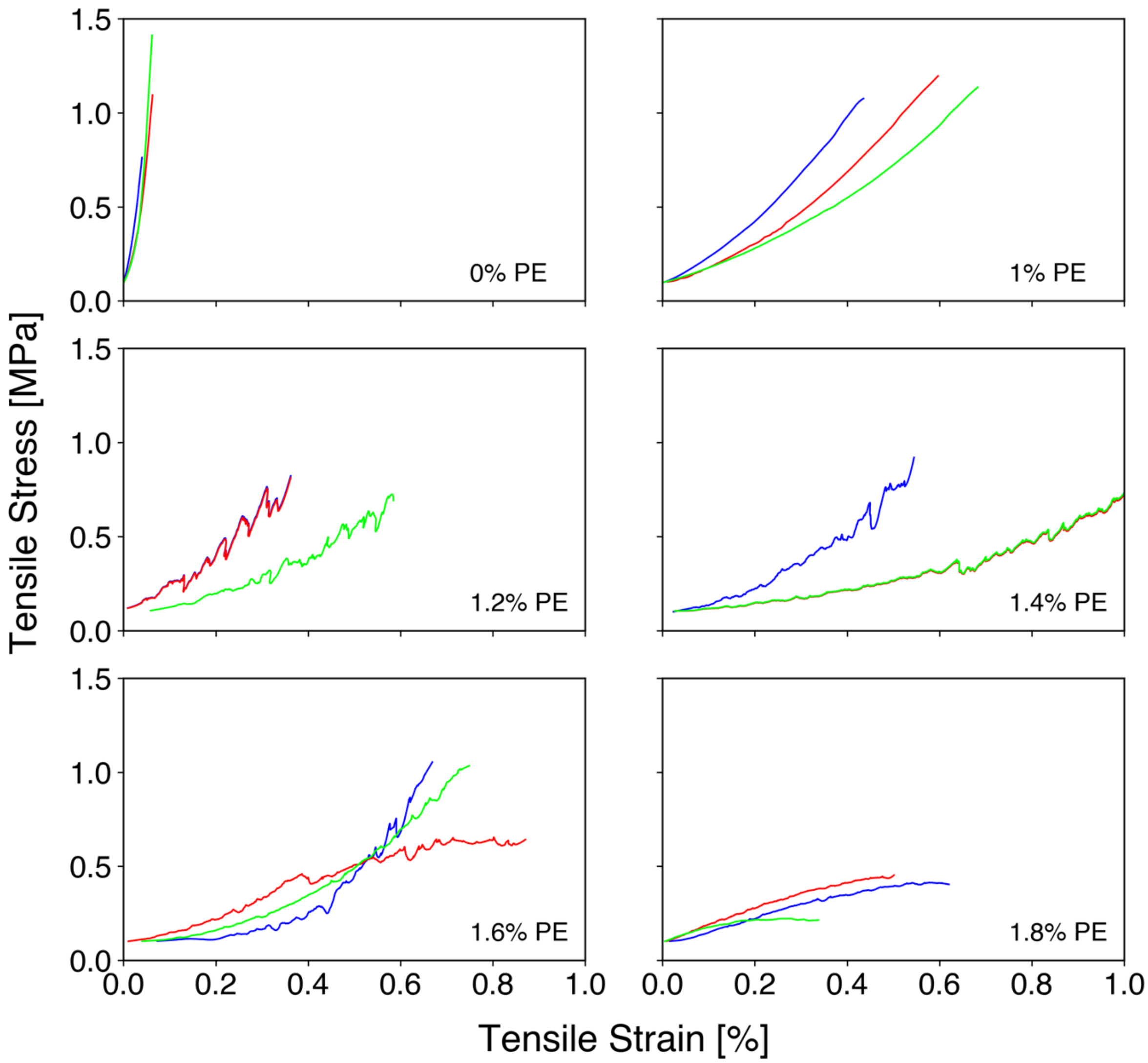

Figure 7-7: Tensile stress-strain curves of the 3D printed specimens which are reinforced by PE fibers and tested on T1

In contrast, significant improvements in tensile behavior were observed in the T2 loading direction, where the specimens were tested along the printing direction (Figure 7-8). This finding is in agreement with other studies that have demonstrated the potential of aligned fibers in enhancing the mechanical properties of cementitious composites [161, 162]. As the percentage of PE fibers increased, the number of microcracks also increased. This observation suggests that the fiber reinforcement in the T2 direction effectively bridged and inhibited the formation and propagation of microcracks, leading to improved tensile properties. Similar results have been reported in the literature, where fibers have been shown to control crack propagation and reduce the crack width in cementitious composites [163]. Nevertheless, the standard deviation in the failure strain of specimens with 1.6% and 1.8% fiber content is higher, which could indicate that the increased fiber content may lead to agglomeration or an excess of stress concentrations, which could counteract the benefits of fiber reinforcement [164, 165].

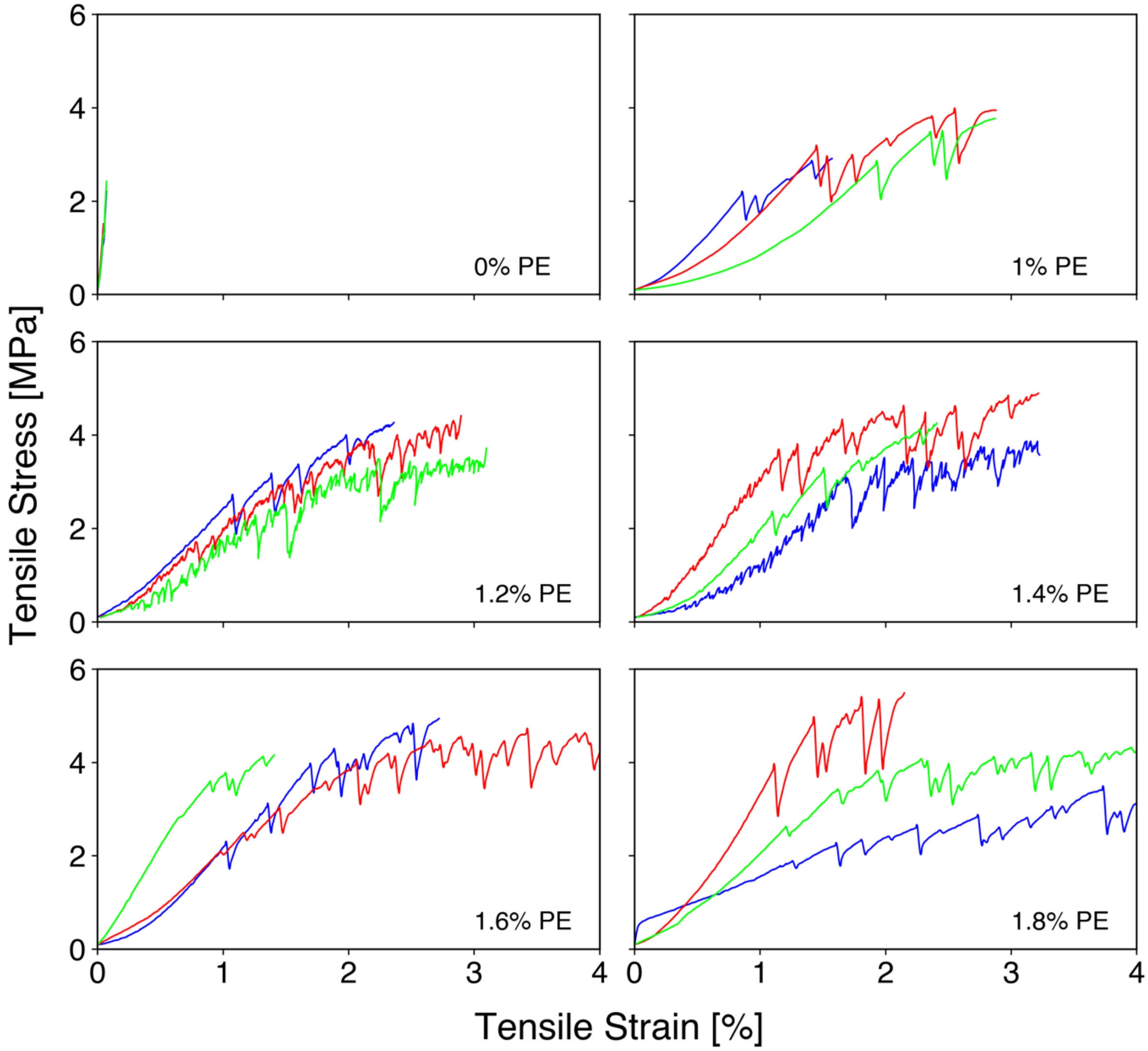

Figure 7-8: Tensile stress-strain curves of the 3D printed specimens which are reinforced by PE fibers and tested on T2

The analysis of fractured specimens supports the findings on the microcracking behavior of cementitious composites with PE fibers under different loading directions. Figure 7-9 presents the photos of two specimens with 1.4% and 1.6% PE content tested under the T1 loading direction, showing that the failure occurred at the layer interface. No microcracks was observed. This observation is consistent for all other PE loadings (1%, 1.2%, and 1.8%), confirming that fibers oriented perpendicular to the direction of applied force are less effective in providing reinforcement and stress transfer in the matrix.

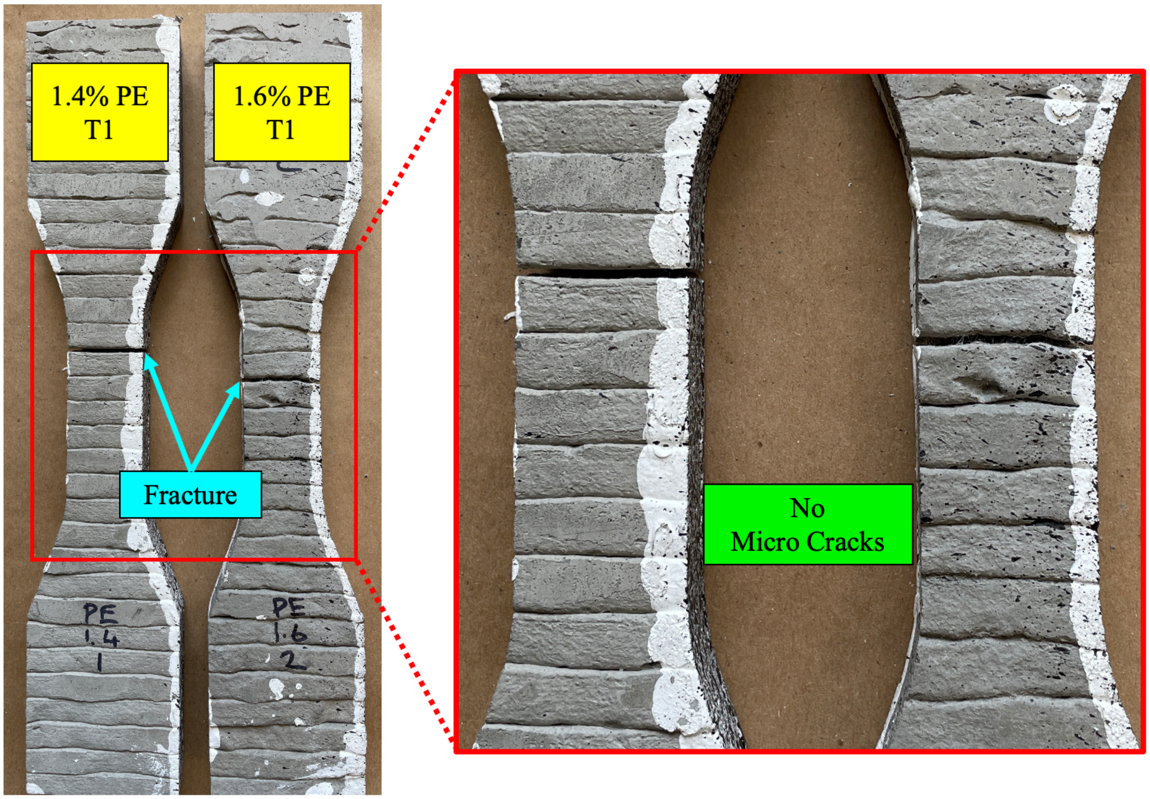

Figure 7-9: Failure of 1.4% and 1.6% PE specimens tested in T1 loading direction

On the contrary, the specimens tested under the T2 loading direction exhibit multiple microcracks as shown in Figure 7-10. The number of microcracks is found to increase with the PE concentration, which suggests that fiber reinforcement in the T2 direction is more effective in bridging and arresting the microcracks. These observations suggest that the loading direction, fiber alignment, and fiber content significantly influence the formation and propagation of microcracks in 3D printed cementitious composites with PE fibers. The presence of microcracks in the T2 loading direction, along with the increasing number of microcracks with higher PE concentrations, highlights the importance of optimizing fiber content and alignment to achieve the desired improvements in tensile behavior and microcrack mitigation.

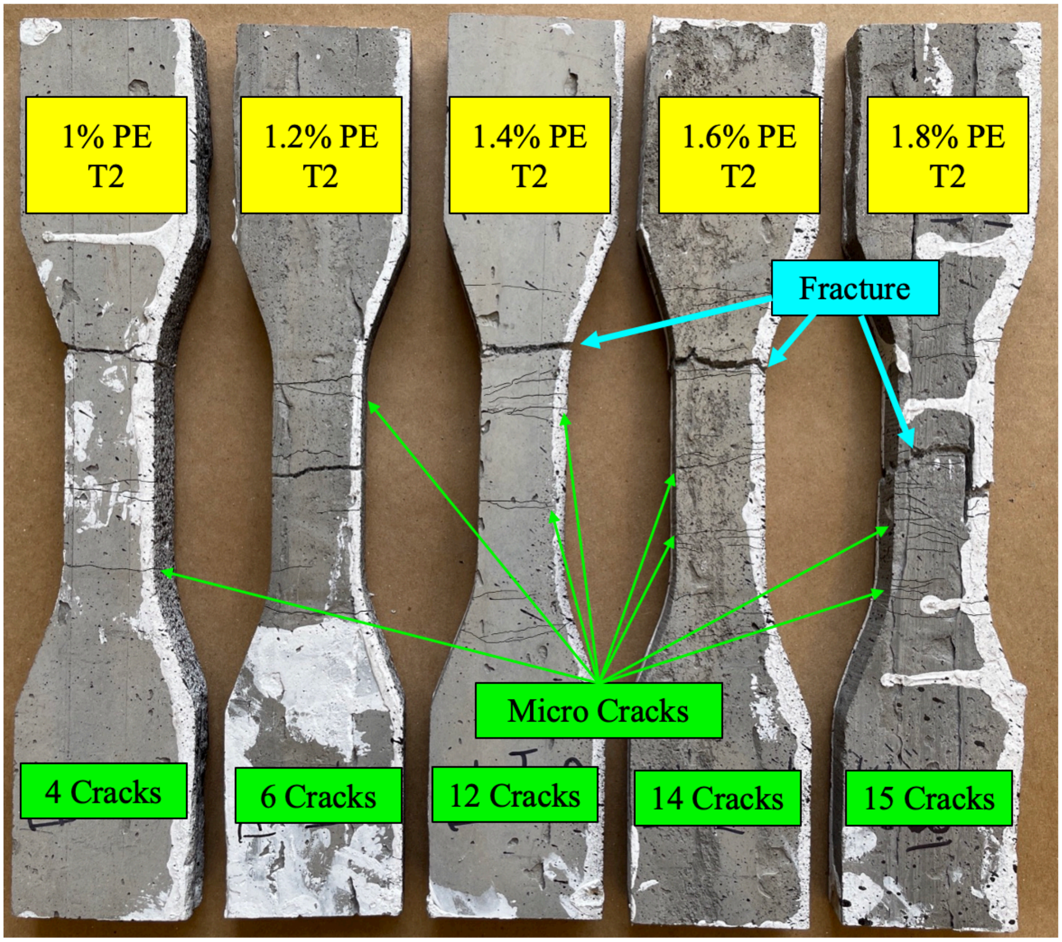

Figure 7-10: Failures and micro cracking behavior of samples tested on T1 loading direction for various PE concentrations

7.5.2. Flexural Strength

The flexural performance of the 3D printed cementitious composites with varying PE fiber content was evaluated and the results are presented in Figure 7-11a. The flexural stress and mid-span displacement values were measured for both F1 and F2 loading directions, which correspond to the tests perpendicular and parallel to the layer interface, respectively. In the control cast sample, a flexural stress of 3.7 MPa and a mid-span displacement of 0.45 mm were observed. For the printed control samples, the flexural stress values were 2.9 MPa and 3.2 MPa for the F1 and F2 directions, respectively, while the mid-span displacements were 0.73 mm and 0.68 mm, respectively. As the percentage of PE fibers increased, both the flexural stress and mid-span displacement values improved for both loading directions. For instance, the flexural stress increased by 272% to 10.8 MPa for the 1.8% PE fiber sample tested in F1 direction compared to the control printed sample. Similarly, the flexural strength increased by 259% to 11.5 MPa for the 1.8% PE fiber sample tested in F2 direction compared to the control printed sample. This improvement in flexural performance can be attributed to the bridging effects of fibers, which enhances the material's ability to resist bending and redistribute stresses more effectively [165].

Moreover, the mid-span displacement values (Figure 7-11b) also significantly increased with the addition of PE fibers, indicating that the material's ductility improved with increased fiber content [166]. For example, the mid-span displacement increased from 0.73 mm in the control printed sample (F1 direction) to 6.54 mm for the 1.8% PE fiber sample. Similarly, the mid-span displacement increased from 0.68 mm in the control printed sample (F2 direction) to 5.09 mm for the 1.8% PE fiber sample. These results suggest that the incorporation of PE fibers in 3D printed cementitious composites can significantly enhance their flexural performance, providing improved resistance to bending and increased ductility.

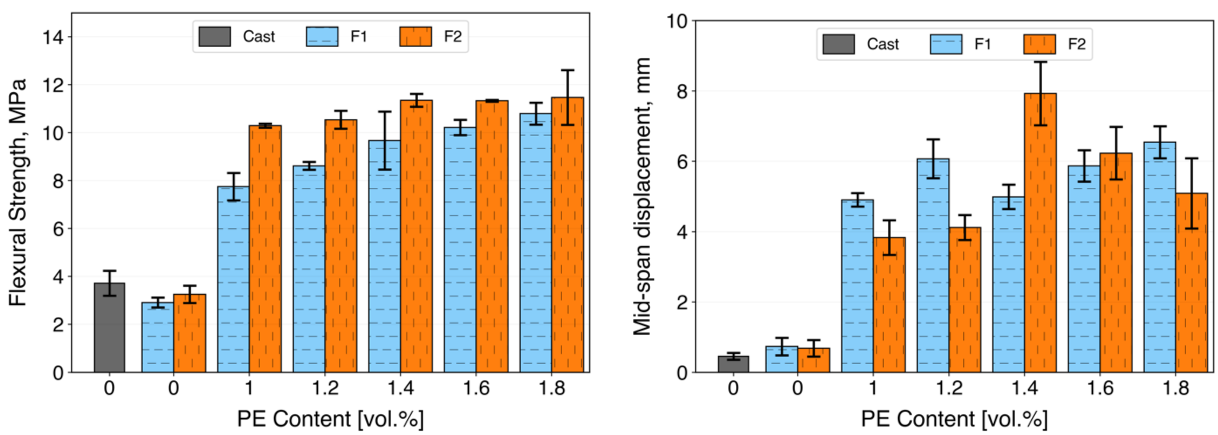

(a) (b)

Figure 7-11: (a) Flexural strength and (b) mid-span displacement variation with increasing PE content

In the flexural performance analysis, flexural strength versus mid-span displacement plots shows a slight difference between the F1 and F2 loading directions. For both loading directions, significant improvements in mid-span displacement were observed, suggesting that the addition of PE fibers contributed to the enhanced flexibility of the cementitious composites. However, unlike tensile properties, no such significant difference was observed in F1 and F2 loading directions.

This phenomenon is represented in Figure 7-12. This observation indicates that the 3D printed cementitious composites experienced increased flexibility when the loading was applied parallel or perpendicular to the layer interface. Although both flexural stress and mid-span displacement increase with increased PE fiber content for both cases, the F2 loading direction, where the layer interface is parallel to the loading direction, demonstrates a marginally dominant performance at higher PE concentrations (1.6% and above) compared to the F1 direction. This could be attributed to that the increased number of fibers on the layer interface brings more effective stress transfer and improved crack bridging in the matrix [167]. Flexural stress vs. mid-span displacement curves of all 3D printed specimens is shown in Figure 7-13. Moreover, the failures and microcracking behavior of samples tested in both F1 and F2 loading directions for various PE concentrations are illustrated in Figure 7-14a and b, respectively. It can be seen that the number of microcracks increases with an increase in PE fiber percentage. These results indicate the ability of PE fibers to control crack propagation and improve flexural behavior in cementitious composites.

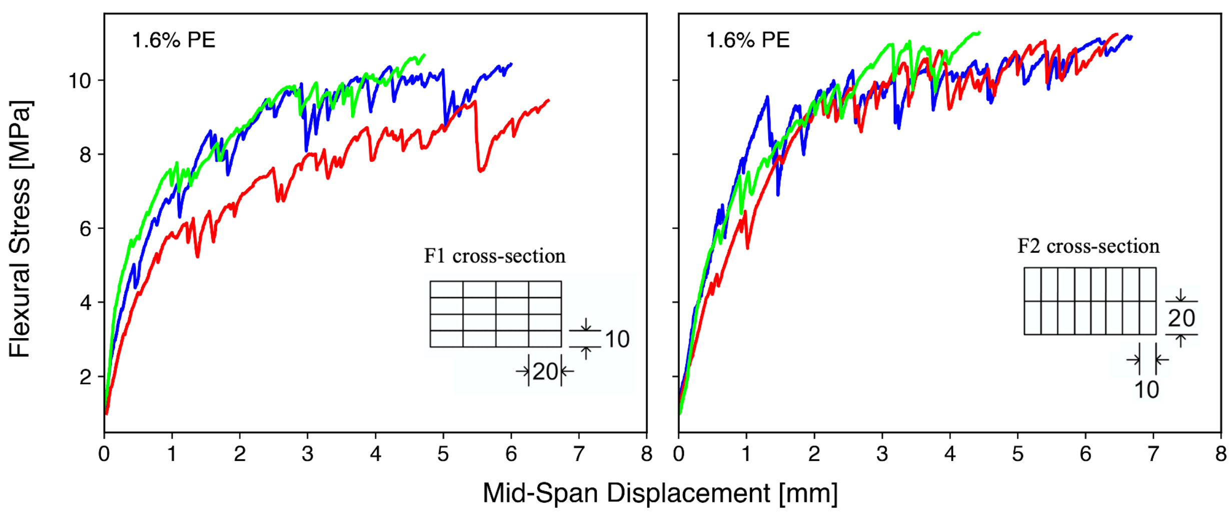

Figure 7-12: Flexural stress vs. mid-span displacement curves of the 3D printed specimens which are reinforced by 1.6% PE fibers and tested on F1 and F2 loading directions

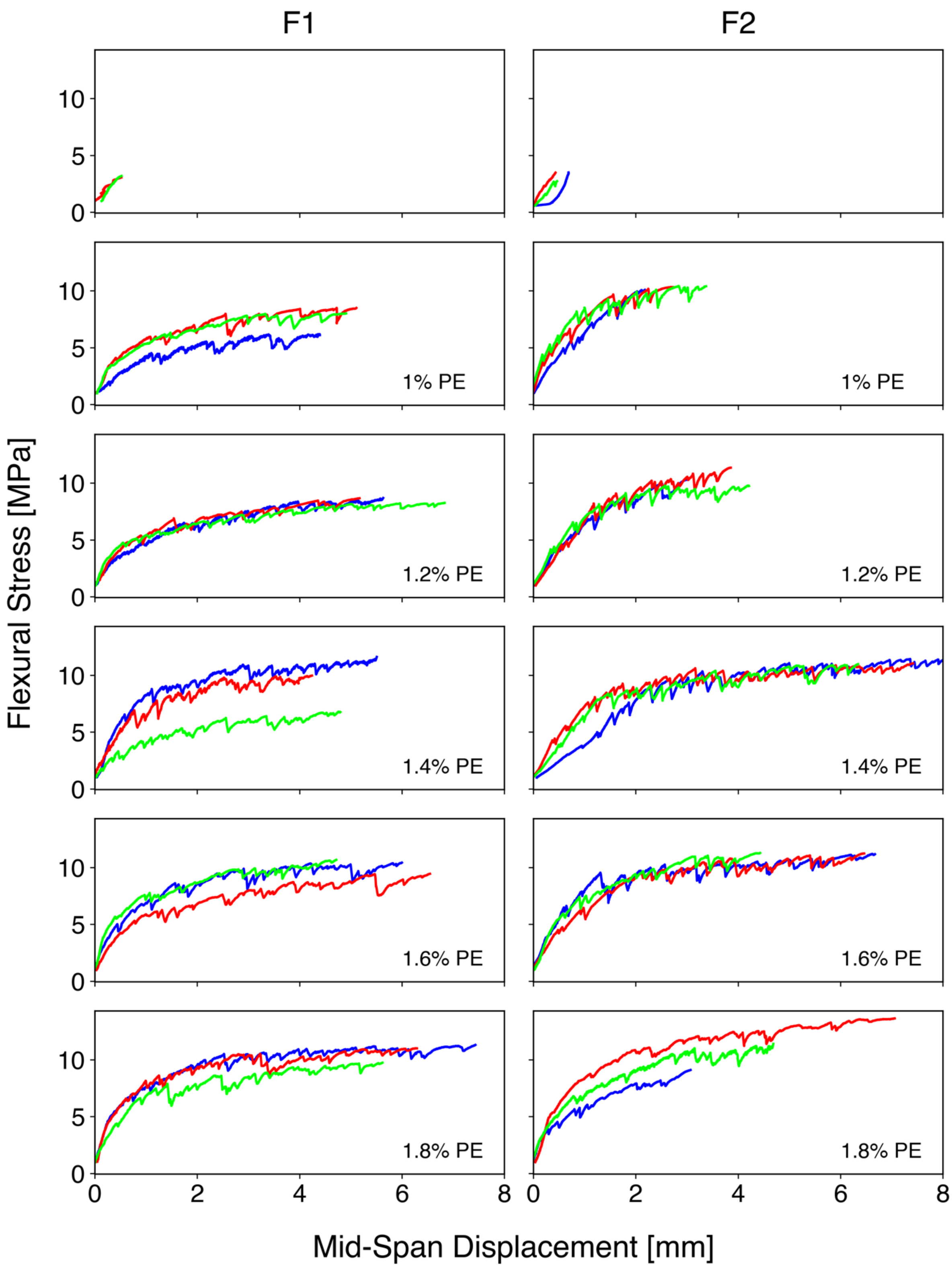

Figure 7-13: Flexural stress versus mid-span displacement curves of the mixtures reinforced by PE fibers

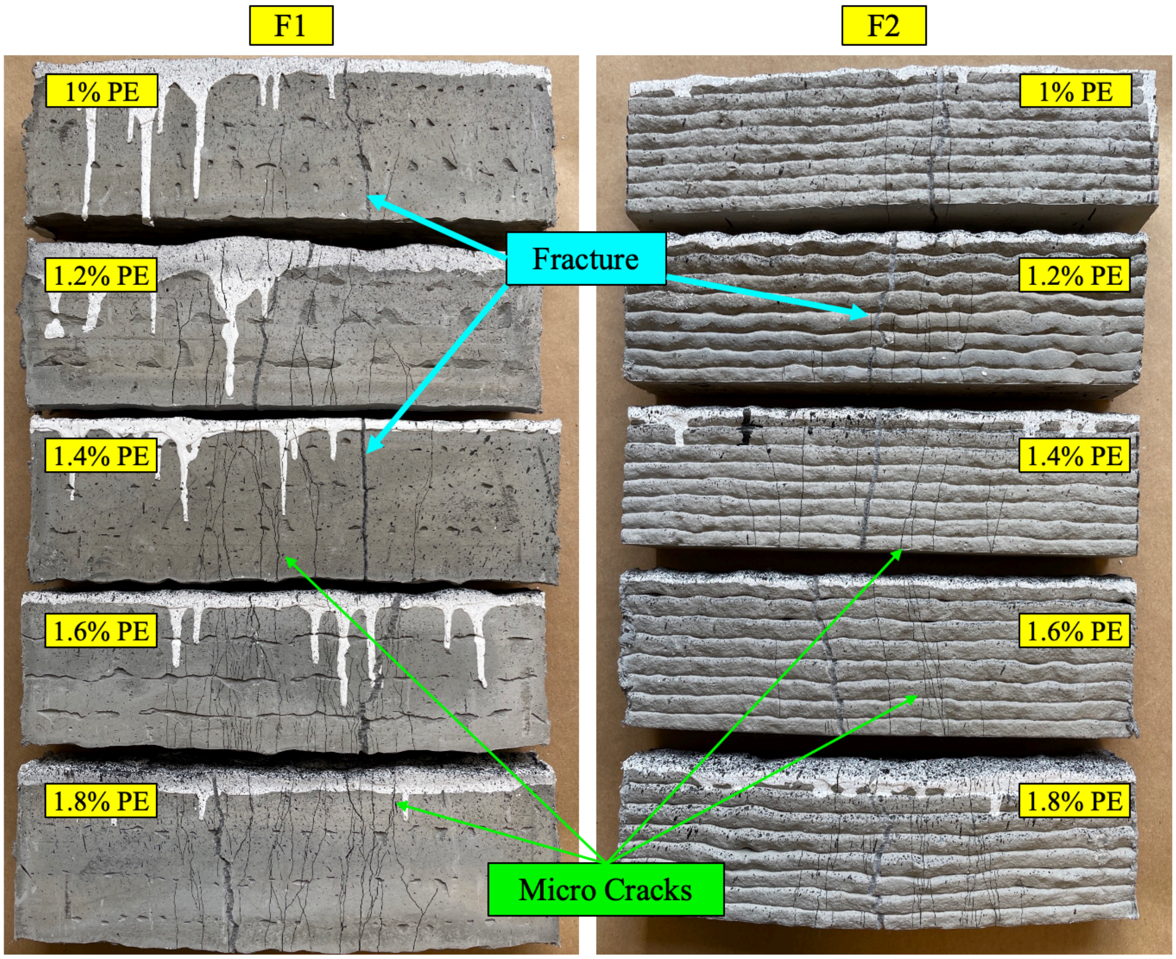

(a) (b)

Figure 7-14: Failures and micro cracking behavior of samples tested on (a) F1 loading direction, and (b) F2 loading direction for various PE concentrations

7.5.3. Compressive Strength

The compressive strength results of the cementitious composites with varying PE fiber content are shown in Figure 7-15. It can be observed that the addition of PE fibers generally led to an increase in compressive strength. For instance, the compressive strength of the control cast sample was 30.5 MPa, while the printed samples with 1% PE fibers showed an increase in strength, with values of 44.8 MPa and 56.2 MPa for C1 and C2 directions, respectively. This indicates that the addition of 1% PE fibers resulted in an increase of approximately 47% and 84% in the C1 and C2 directions, respectively, compared to the control cast sample.

The compressive strength continued to increase with the addition of 1.2% and 1.4% PE fibers, reaching maximum values of 51.7 MPa and 57.9 MPa for the C1 and C2 directions, respectively. However, at 1.6% PE fiber content, a slight decrease in compressive strength was observed, with values of 47.3 MPa and 49.0 MPa for C1 and C2 directions, respectively. A further increase in PE fiber content to 1.8% led to contrasting results: a significant increase in compressive strength for the C1 direction (58.2 MPa), while a notable decrease in strength was observed for the C2 direction (33.9 MPa).

The observed enhancement in compressive strength with the addition of PE fibers can be attributed to their ability to bridge microcracks and improve the overall load-bearing capacity of the composite [168]. However, beyond a certain fiber content threshold, it is possible that fiber agglomeration or excessive stress concentrations could counteract the benefits of fiber reinforcement, leading to inconsistent or reduced compressive strength [164, 169].

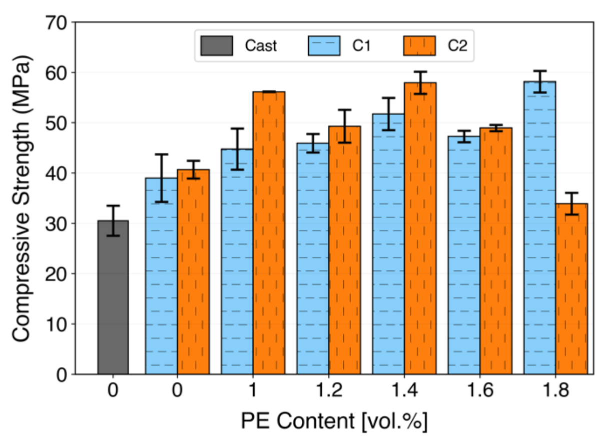

Figure 7-15: Compressive strength variation with increasing PE content

7.6. DIC Analysis

The evolution of horizontal strain fields for both F1 and F2 loading directions and varying fiber content (1%, 1.4%, and 1.8%) is illustrated in Figure 7-16. The Digital Image Correlation (DIC) strain contour images demonstrate that the number of microcracks in the specimens increases with the addition of PE fibers. For the specimen with 1% PE fiber, only a few cracks microcracks are visible for F1 and F2 loading directions as shown in Figure 7-16a and b, respectively. As the fiber content increases to 1.4%, the number of microcracks also increases, occurring in the strain concentration areas. Further increasing the PE fiber content to 1.8% leads to an increase in the concentrated strain areas (Figure 7-16e and f), indicating a higher number of microcracks. This observation suggests that the increased fiber content contributes to more extensive crack propagation and an enhanced ability to bridge and distribute stresses throughout the composite material [170]. The increased ductility and crack propagation in specimens with higher fiber content can be attributed to the fibers' ability to redistribute stresses and prevent the formation of dominant cracks [171]. The layering process inherent to 3D printing might have improved the material's performance in flexure. The inherent defects at the layer interfaces can avoid strain concentrations and crack propagation while improving deformability [172].

When the results obtained from F1 and F2 loading directions were compared, a relatively more widespread distribution of microcracks is observed when the specimens were tested in the F2 loading direction (Figure 7-16d and f). Note that the specimens tested both in F1 and F2 directions were cut from a plate that include multiple layers both in width and height. However, the specimen tested in F2 loading direction has more layer interfaces along the width of the specimen. During flexural testing of the printed specimens, the propagation of transverse cracks across the whole width of the specimen are prevented by the layer interfaces. As more interface layer are present in the F2 loading direction, the testing in this direction leads to a more widespread and complex distribution of microcracks.

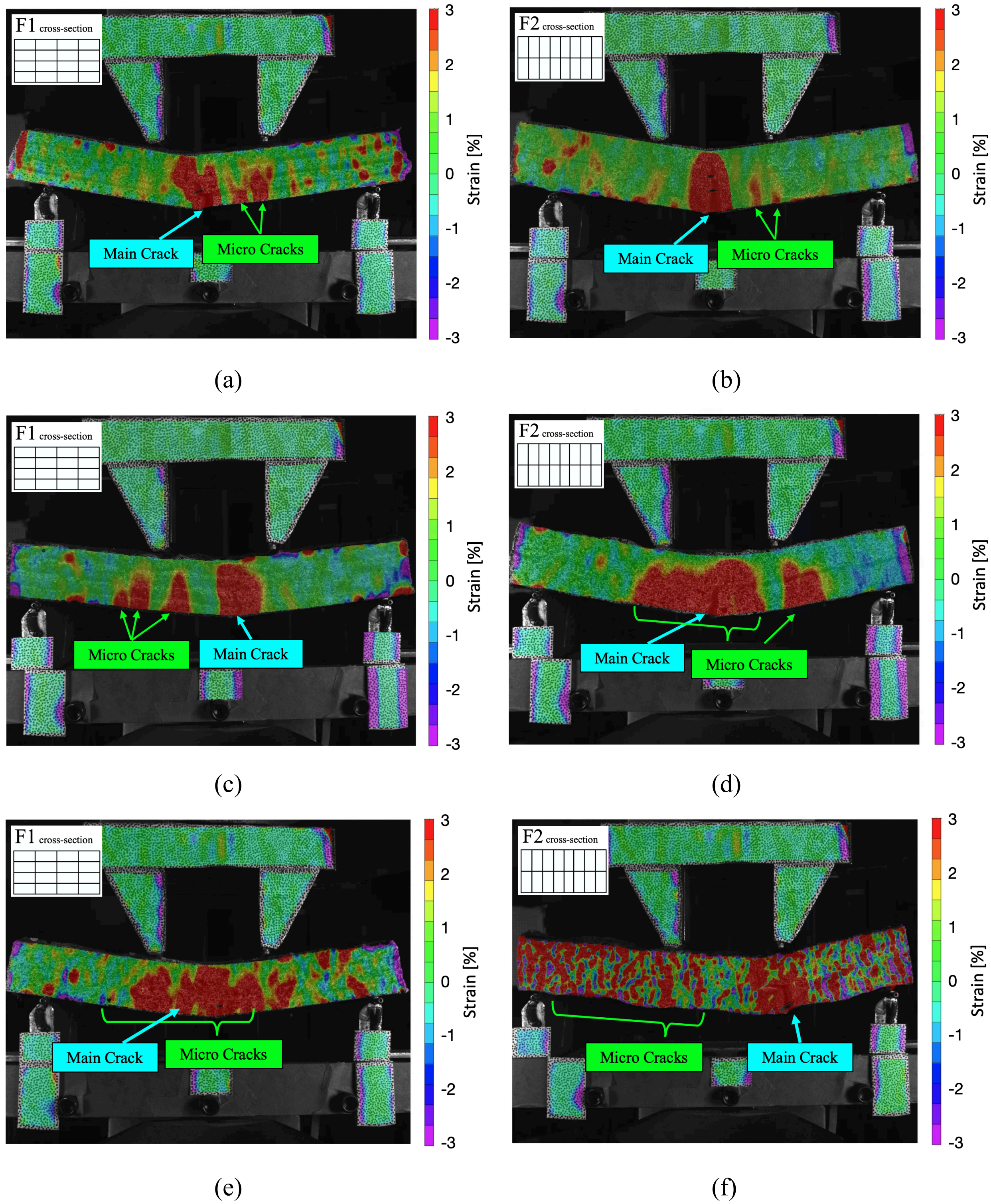

Figure 7-16: The evolution of the horizontal strain field of the specimens; (a) 1% PE tested on F1, (b) 1% PE tested on F2, (c) 1.4% PE tested on F1, (d) 1.4% PE tested on F2, (e) 1.8% PE tested on F1, and (f) 1.8% PE tested on F2

7.7. Microstructural Analysis

Figure 7-17a and b depict the fractured surface of a 1.8% PE reinforced composite tested under tensile load in the T2 direction. It is clear that the fibers are oriented along the printing direction (Figure 7-17a), aligned perpendicular to the fractured surface. This alignment demonstrates the effectiveness of the 3D printing process in achieving the desired fiber orientation to enhance tensile properties. However, the SEM images also reveal that some fibers have detached from the fractured surface, leaving behind visible fiber holes. This could be attributed to the failure of the interfacial bond between the fibers and the matrix, which might impact the composite's overall performance. In Figure 7-17c and d, the SEM images show a 1.8% PE reinforced specimen tested under flexural load in the F2 direction. Here, the fibers can be seen bridging the mortar matrix along cracking surface, effectively restraining the crack propagation and providing enhanced flexural behavior. This observation supports the previously discussed notion that adding PE fibers in 3D printed cementitious composites can significantly enhance their flexural performance.

Figure 7-17e presents an SEM image of a compressive specimen containing 1.8% PE fibers, where large PE entanglements are visible. These entanglements could potentially explain the observed decrease in compressive strength at this fiber content, as they might lead to stress concentrations and hinder the effective transfer of stress between the fibers and the matrix. Figure 7-17f illustrates the SEM image of a 1.8% PE reinforced mixture tested under tensile load in the T2 direction. Similar to Figure 7-17a, the fibers are oriented along the printing direction and elongated along the fractured surface. The presence of fiber traces suggests that some fibers may have detached from the matrix during the tensile testing, highlighting the importance of optimizing the interfacial bond between the fibers and the matrix for improved mechanical performance.

In conclusion, the SEM analysis provides a deeper understanding of the fiber distribution, orientation, and interaction with the cementitious matrix during various loading conditions. The observed fiber alignment and crack bridging behavior contribute to the enhanced mechanical properties of the 3D printed cementitious composites. However, the fiber detachment and entanglements observed in some instances emphasize the need for further research on optimizing fiber content, interfacial bonding, and fiber dispersion to achieve improved mechanical performance in 3D printed cementitious composites.

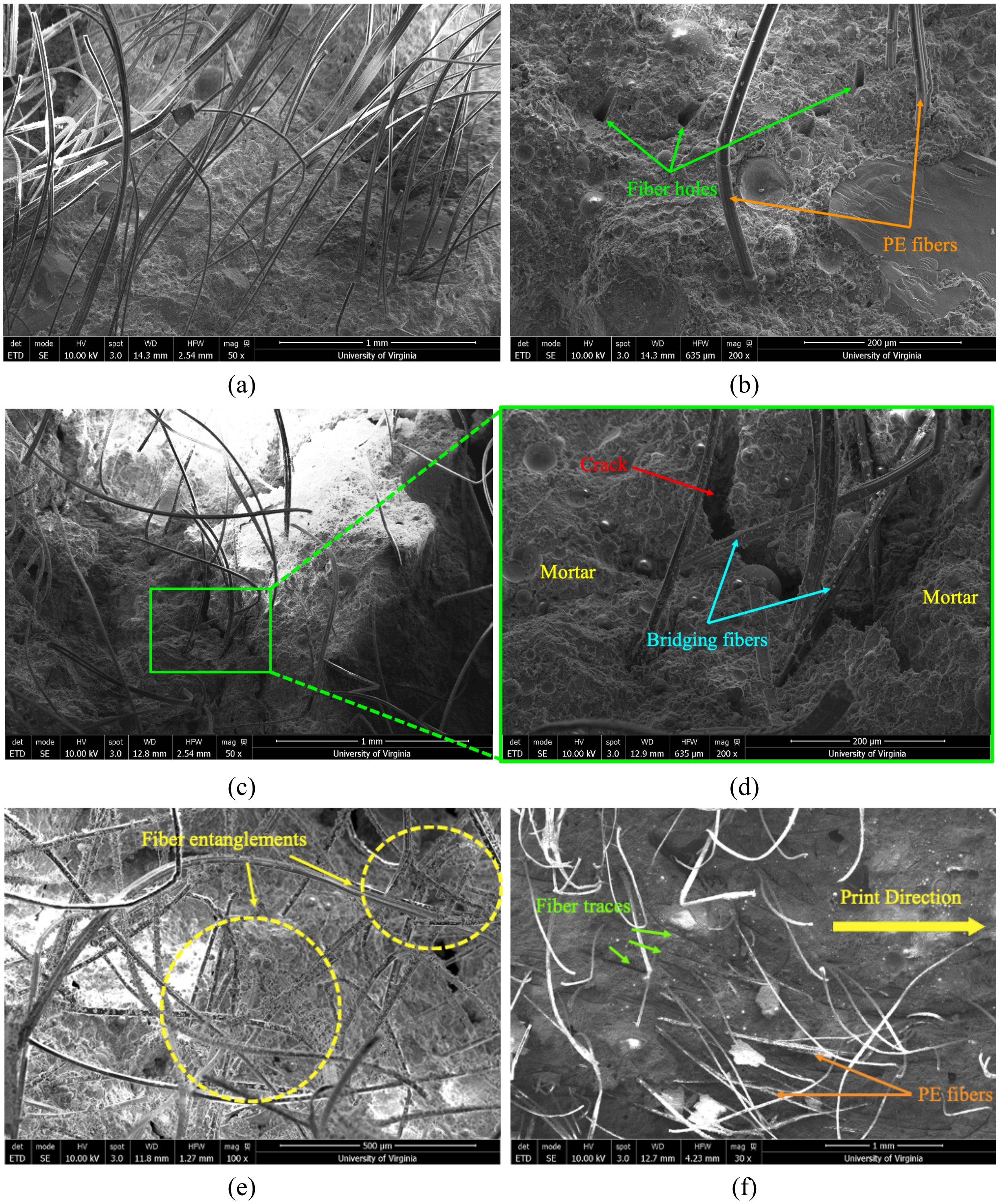

Figure 7-17: SEM images of the fractured surfaces; (a) and (b) 1.8% PE reinforced composite tested on T2, (c) and (d) 1.8% PE reinforced composite tested on F2, (e) 1.8% PE reinforced composite tested on C2, and (f) 1.8% PE reinforced composite tested on T1

7.8. Summary

In this study, the effect of PE fibers on the rheological and mechanical properties of cementitious mixtures was investigated. The PE fiber ratios used in this study are 0%, 1%, 1.2%, 1.4%, 1.6%, and 1.8% PE. The key findings of this research can be summarized as below:

- Static Yield Stress (SYS) is significantly increased with increasing PE fiber content, with a 27% enhancement at 1% PE fibers and up to a 224% increase at 1.8% PE fibers. Dynamic Yield Stress (DYS) and plastic viscosity are also showed considerable increases with the addition of PE fibers. A 60% increase in DYS and a 48% increase in viscosity was observed for 1% PE fiber addition, and a 385% increase in DYS and a 98% increase in viscosity was present for 1.8% PE fiber inclusion. Similarly, notable increases were observed in the viscoelastic properties (storage modulus and critical strain) with a 170% increase in storage modulus and a 122% increase in critical strain at 1.8% PE fibers, contributing to the stiffness, resistance to deformation, and enhanced capacity to undergo deformation before failure.
- The layer-by-layer deposition process in 3D printing resulted in weaker interlayer bonding and lower tensile strength compared to cast samples. The addition of PE fibers improved the tensile strength of printed samples, particularly in the T2 direction, due to enhanced fiber-matrix bonding, alignment of fibers parallel to the printing direction, bridging effect, and more uniform stress distribution. However, tensile strength in the T1 direction decreased with increasing PE content, possibly because of the fiber orientation and alignment between subsequent layers.
- The incorporation of PE fibers led to significant improvements in tensile strain, especially in the T2 direction. However, the tensile strain in the T1 direction decreased as the PE content increased, likely due to less effective stress transfer or fiber orientation.
- The loading in the T1 direction created tensile stresses along the normal direction of the bonded interface of printed layers, leading to interfacial failure, while loading in the T2 direction caused shear stresses on the translation interface of printed layers. Microcrack formation and propagation in 3D printed cementitious composites with PE fibers were significantly influenced by loading direction, fiber alignment, and fiber content. The absence of microcracks in the T1 direction suggests that the PE fibers are not significantly

contributing to the reinforcement of the layer interface, while the presence of microcracks in the T2 loading direction highlights the importance of optimizing fiber content and alignment for improved tensile behavior and microcrack mitigation.

- The flexural performance of the 3D printed cementitious composites experienced increased flexibility when the loading was applied parallel or perpendicular to the layer interface. The number of microcracks increased with an increase in PE fiber percentage, consistent with previous studies reporting the ability of PE fibers to control crack propagation and improve flexural behavior in cementitious composites.
- The compressive strength increased with the addition of 1.2% and 1.4% PE fibers but began to decrease at 1.6% PE fiber content. A further increase in fiber content to 1.8% led to contrasting results, with a significant increase in compressive strength for the C1 direction, while a notable decrease was observed for the C2 direction.

8. Summary, Conclusions and Recommendations

8.1. Summary

3D Concrete Printing (3DCP) is an emerging construction technology that enables digital control over design, fabrication, and assembly processes. It offers various benefits such as design freedom, lower labor costs, faster construction, reduced waste, and customization. The most common technique for commercial 3DCP is extrusion-based, which requires cementitious mixtures with specific rheological properties for pumping, extruding, and building. During pumping and extrusion processes, a workable mixture with low plastic viscosity and dynamic yield stress is required, whereas a mixture with high static yield stress and significant thixotropy is necessary for maintaining shape and buildability. The contradictory nature of these requirements highlights the need for research on the rheological properties of 3D printable cementitious mixtures to develop innovative mixtures for 3DCP applications. While prior research has investigated the impact of additives on the fresh properties of cementitious composites, there is still a limited understanding of the relationship between fresh properties, the printability characteristics of the cementitious composites. Furthermore, although the fresh state properties of printable mixtures are crucial for seamless fabrication of 3D printed concrete structures, it is vital to attain desirable hardened-state properties in the printed mixtures to fully capitalize on the advantages provided by this technology.

This dissertation aims to develop an understanding on the role of different additives on rheological characteristics and printability of cementitious mixtures as well as mechanical performance of 3D printed samples. First, a comprehensive experimental investigation is conducted to study the influence of a starch-based viscosity modifying admixture (VMA) and attapulgite nanoclay (ANC) on the fresh and rheo-viscoelastic behavior of mortar mixtures for additive manufacturing. In order to examine the influence of VMA and ANC on the rheological characteristics of mortar mixtures, a factorial design approach is used to design the experiments. With VMA (0%, 0.1%, 0.2% and 0.3%) and ANC (0%, 0.2%, 0.4% and 0.6%) as the two factors and four levels for each factor, the experimental design aims to analyze the primary effects and interaction effects of these factors on the response variables. The printability and buildability of select mixtures are characterized through direct printing tests using a 3D concrete printer with a screw pumping mechanism.

Furthermore, a thermogravimetric analysis (TGA) is performed to assess the effects of VMA and ANC on the hydration characteristics of mortar mixtures. The results obtained from the experiments are analyzed and presented to assess the role of VMA and ANC on key properties of printable mixtures, providing insights into their effects on the buildability performance for 3DCP.

Next, a relatively new and bio-based nanomaterial, cellulose nanofilaments (CNF), is used to modify the rheological properties of cementitious mixtures for the 3DCP. The mortar mixtures varying CNF contents (0%, 0.1%, 0.2%, 0.3%, 0.4%, and 0.5%) is prepared. The CNFs are dispersed in water using a high shear mixer prior to being added to the cementitious mixture. The rheological and buildability of the developed mixtures are carried out. Additionally, the mechanical tests, including tensile, flexural, and compressive strength tests, are performed to explore the effect of CNF on the mechanical properties of the cementitious mixtures. The mechanical tests are performed in two directions to evaluate anisotropy in the printed specimens. Lastly, scanning electron microscopy (SEM) analysis is performed on the fractured surfaces to study the effects of CNF incorporation into the microstructure of the mortar mixes.

The dissertation then focuses of improving mechanical properties of printed samples using nano and micro scale fibers. The effects of graphene nanoplatelets (GNPs) on 3D printable cementitious composites is investigated first. Mortar mixtures with varying GNP concentrations (0%, 0.025%, 0.05%, 0.1%, 0.15%, and 0.2%) are prepared. The GNPs are sonicated in a solution of water and a superlasticizer to improve their dispersion. The rheological properties of GNP-reinforced mortar mixtures are assessed using rotational and oscillatory tests. The 3D printed specimens with different GNP concentrations and methods are prepared to examine GNPs' impact on compressive, flexural, and tensile properties. The mechanical tests are performed in two directions to evaluate anisotropy in the printed specimens. In order to explore the effect of GNPs on microstructure of cement mortar, the SEM analysis is conducted.

Finally, the addition of polyethylene (PE) fibers on 3D printable cementitious composites to enhance their tensile characteristics is investigated. The use of PE fibers is expected to provide better crack resistance and ductility, resulting in more resilient structures. PE fiber ratios used in this chapter are 0%, 1%, 1.2%, 1.4%, 1.6% and 1.8% by volume of mortar mixture. The rheological and mechanical characterization of the developed composites are carried out. The SEM analysis is conducted to evaluate the microstructure, while Digital Image Correlation (DIC) is used to monitor full field deformations during flexural testing.

8.2. Conclusions and Recommendations

The key findings from this research can be summarized as follows:

- The addition of ANC into cementitious mixtures leads to an almost linear increase in static yield stress (SYS) and dynamic yield stress (DYS). The rate of this increase was higher when the VMA is present. On the other hand, plastic viscosity generally decreases with the ANC addition and increases with VMA addition, with no clear pattern observed. When the visco-elastic properties is considered, the ANC significantly increases the storage modulus and leads to a decrease in loss factor. The VMA has a limited influence on the visco-elastic properties of cementitious mixtures. ANOVA results show that ANC significantly affects SYS and viscoelastic properties, while VMA primarily influences plastic viscosity.
- The static yield stress and storage modulus is found to be most critical parameters for the buildability of the cementitious mixtures. The mixtures with SYS between 2200 Pa and 4200 Pa and storage modulus between 20 kPa and 45 kPa exhibited both plastic collapse and elastic buckling failures. The mixtures with SYS over 4200 Pa and storage modulus over 45 kPa retained their shape and supported deposited layers without plastic deformation and the failure occurred due to pure elastic buckling.
- The addition of CNF in cementitious composites led to a significant increase in SYS, from 86 Pa for 0% CNF to a maximum of 10,313 Pa for 0.5% CNF. The dynamic yield stress (DYS) also increases with higher CNF concentrations, with a more rapid increase observed when the CNF ratio was over 0.3%. The plastic viscosity of the mixtures also increases with the addition of CNF, although the rate of increase decreases with increasing CNF ratio. The mixes containing 0.3% to 0.5% CNF were successfully printed, while the mixtures with lower CNF ratios found not printable. The tensile and flexural strengths of cementitious mixtures increased when the CNF concentration increases from 0.3% to 0.4%. They decreased when the CNF ratio was further increase to 0.5%. The compressive

strength was highest for the specimens with 0.3% CNF. It was also observed that the hydration of the cement was affected by CNF addition, leading to increased CH content and hydration percentage at both early and later stages.

- The addition of GNPs up to 0.2% by weight of cement has modest effects on the rheological properties. The results show that increasing GNP concentration increases the SYS. The highest increase was observed for the mixtures with 0.2% GNP, where the mixture exhibited a 54% increase in SYS compared to the control mixture without any GNP. The DYS and plastic viscosity also increase with increasing GNP content, with the largest increase observed at 0.2% GNP. The viscoelastic properties of the mortar mixtures were only slightly improved with the addition of GNPs.
- The tensile strength of 3D printed mortar specimens was significantly improved by the GNP addition. The addition of GNPs effectively mitigated the tensile strength losses observed in printed specimens. There was even at least 55% increase in tensile strength for two test directions of printed specimens compared to the control cast specimens when the GNP concentration was 0.2%. The addition of 0.2% GNPs to the mortar mixtures also improved the flexural strength by 51% of the printed specimens compared to the cast specimen. The compressive strength of cast specimens was higher than the printed specimen for the mixtures with 0%, 0.025%, and 0.05% GNPs. However, when the GNP ratio was 0.1%, the compressive strength increased by 50% compared to the cast specimen and by 98% compared to the printed specimen without any GNPs. Further increases in GNP content resulted in slightly decreases in compressive strength compared to specimens with 0.1% GNPs, yet still showed improvement over the cast and printed specimens.
- The addition of PE fibers to cementitious composites leads to significant increases in SYS, DYS, plastic viscosity, and viscoelastic properties, with the highest enhancements observed at 1.8% PE fibers. The improved properties can be attributed to the stiffening effect of the fibers, which enhances the resistance to deformation and stiffness of the matrix.
- While the layer-by-layer deposition process in 3D printing typically results in weaker interlayer bonding and lower tensile strength compared to cast samples, the addition of 1.6% PE fibers improved the tensile strength of printed samples by 124% in the T2 direction compared to the printed sample without any PE fibers. However, the tensile

strength in the T1 direction was not affected considerably by the PE fiber content, possibly due to fiber orientation and alignment between subsequent layers. The loading direction also significantly influences the microcrack formation and propagation in 3D printed cementitious composites with PE fibers. There was no microcracks in the specimens tested in the T1 direction suggesting that the PE fibers are not significantly contributing to the bonding in the deposition layer interfaces. The presence of microcracks in the T2 direction highlights the importance of optimizing fiber content and alignment for improved tensile behavior and microcrack mitigation. The flexural performance of the 3D printed cementitious composites also significantly improved with an increase in PE fiber percentage. For the two test directions, there was at least 259% increase in the flexural strength for the printed mixtures with 1.8% PE fibers compared to those without any fibers. Compared to the printed samples without any PE fibers, the compressive strength mostly increased with the addition PE fibers up to 1.6% but began to slightly decrease at 1.6% PE fiber content, with contrasting results observed for two test directions at 1.8% PE fiber content.

The results obtained from these studies highlight the importance of selecting appropriate additives and concentrations to achieve desired rheological and printability characteristics in cementitious composites. Therefore, it is recommended to carefully consider the influence of different additives on different fresh and hardened properties of the cementitious matrix as revealed in this dissertation when developing printable mixtures. Further research can be conducted to explore the effects of printing process parameters on the performance of 3D printable cementitious mixtures with different additives. There is also need for research on the effects of different additivities on the durability properties of printed cementitious composites. A complete understanding of rheological, mechanical, and durability properties of printed cementitious composites reinforced with nano and micro-scale fibers can accelerate the use of such innovative mixtures for real-world 3DCP applications. It should be also noted that the dispersion of nano reinforcement such as CNF or GNPs play a critical role on the performance of the fabricated composites. In this research, a select dispersion technique was used to incorporate nano reinforcements into cementitious mixtures without an in-depth study on the influence of different dispersion techniques. Future studies can explore the performance of printable mixtures with CNF or GNP prepared with different dispersion methods. For the printable mixtures with micro-scale fibers, optimizing the content and alignments of fibers in cementitious matrices can be further studied. Future research can also be conducted on the environmental impact assessment of different printable mixtures since similar to conventional construction, the material production accounts for majority of emissions (88% to 99% of total emissions) in the 3DCP [173].

References

1. Perkins, I., & Skitmore, M. (2015). Three-dimensional printing in the construction industry: A review. International Journal of Construction Management, 15(1), 1–9. https://doi.org/10.1080/15623599.2015.1012136

2. Lim, S., Le, T., Webster, J., Buswell, R. A., Austin, S., Gibb, A., & Thorpe, A. (2009). Fabricating construction components using layer manufacturing technology. Proc Int Conf Glob Innov Constr, 512–520.

3. Lu, B., Weng, Y., Li, M., Qian, Y., Leong, K. F., Tan, M. J., & Qian, S. (2019). A systematical review of 3D printable cementitious materials. Construction and Building Materials, 207, 477–490. https://doi.org/10.1016/j.conbuildmat.2019.02.144

4. Mohan, M. K., Rahul, A. V., Van Tittelboom, K., & De Schutter, G. (2021). Rheological and pumping behaviour of 3D printable cementitious materials with varying aggregate content. Cement and Concrete Research, 139, 106258. https://doi.org/10.1016/j.cemconres.2020.106258

5. Kazemian, A., Yuan, X., Cochran, E., & Khoshnevis, B. (2017). Cementitious materials for construction-scale 3D printing: Laboratory testing of fresh printing mixture. Construction and Building Materials, 145, 639–647. https://doi.org/10.1016/j.conbuildmat.2017.04.015

6. Jayathilakage, R., Rajeev, P., & Sanjayan, J. G. (2020). Yield stress criteria to assess the buildability of 3D concrete printing. Construction and Building Materials, 240, 117989. https://doi.org/10.1016/j.conbuildmat.2019.117989

7. Tramontin Souza, M., Maia Ferreira, I., Guzi de Moraes, E., Senff, L., Arcaro, S., Castro Pessôa, J. R., … Novaes de Oliveira, A. P. (2022). Role of chemical admixtures on 3D printed Portland cement: Assessing rheology and buildability. Construction and Building Materials, 314, 125666. https://doi.org/10.1016/j.conbuildmat.2021.125666

8. Papatzani, S. (2016). Effect of nanosilica and montmorillonite nanoclay particles on cement hydration and microstructure. Materials Science and Technology, 32(2), 138–153. https://doi.org/10.1179/1743284715Y.0000000067

9. Qian, Y., & De Schutter, G. (2018). Enhancing thixotropy of fresh cement pastes with nanoclay in presence of polycarboxylate ether superplasticizer (PCE). Cement and Concrete Research, 111, 15–22. https://doi.org/10.1016/j.cemconres.2018.06.013

10. Varela, H., Barluenga, G., & Palomar, I. (2020). Influence of nanoclays on flowability and rheology of SCC pastes. Construction and Building Materials, 243, 118285. https://doi.org/10.1016/j.conbuildmat.2020.118285

11. Long, W.-J., Tao, J.-L., Lin, C., Gu, Y., Mei, L., Duan, H.-B., & Xing, F. (2019). Rheology and buildability of sustainable cement-based composites containing micro-crystalline

cellulose for 3D-printing. Journal of Cleaner Production, 239, 118054. https://doi.org/10.1016/j.jclepro.2019.118054

12. Muhammad Salman, N., Ma, G., Ijaz, N., & Wang, L. (2021). Importance and potential of cellulosic materials and derivatives in extrusion-based 3D concrete printing (3DCP): Prospects and challenges. Construction and Building Materials, 291, 123281. https://doi.org/10.1016/j.conbuildmat.2021.123281

13. Cao, Y., Zavaterri, P., Youngblood, J., Moon, R., & Weiss, J. (2015). The influence of cellulose nanocrystal additions on the performance of cement paste. Cement and Concrete Composites, 56, 73–83. https://doi.org/10.1016/j.cemconcomp.2014.11.008

14. Cao, Y., Tian, N., Bahr, D., Zavattieri, P. D., Youngblood, J., Moon, R. J., & Weiss, J. (2016). The influence of cellulose nanocrystals on the microstructure of cement paste. Cement and Concrete Composites, 74, 164–173. https://doi.org/10.1016/j.cemconcomp.2016.09.008

15. Balandin, A. A., Ghosh, S., Bao, W., Calizo, I., Teweldebrhan, D., Miao, F., & Lau, C. N. (2008). Superior Thermal Conductivity of Single-Layer Graphene. Nano Letters, 8(3), 902–907. https://doi.org/10.1021/nl0731872

16. Wang, B., Jiang, R., & Wu, Z. (2016). Investigation of the Mechanical Properties and Microstructure of Graphene Nanoplatelet-Cement Composite. Nanomaterials, 6(11), 200. https://doi.org/10.3390/nano6110200

17. Zheng, Q., Han, B., Cui, X., Yu, X., & Ou, J. (2017). Graphene-engineered cementitious composites: Small makes a big impact. Nanomaterials and Nanotechnology, 7, 1847980417742304. https://doi.org/10.1177/1847980417742304

18. Abedi, M., Fangueiro, R., & Gomes Correia, A. (2020). Ultra-Sensitive Affordable Cementitious Composite with High Mechanical and Microstructural Performances by Hybrid CNT/GNP. Materials, 13(16), 3484. https://doi.org/10.3390/ma13163484

19. Dong, W., Li, W., Zhu, X., Sheng, D., & Shah, S. P. (2021). Multifunctional cementitious composites with integrated self-sensing and hydrophobic capacities toward smart structural health monitoring. Cement and Concrete Composites, 118, 103962. https://doi.org/10.1016/j.cemconcomp.2021.103962

20. Kirschbaum, R., & van Dingenen, J. L. J. (1989). Advances in gel-spinning technology and Dyneema fiber applications. In P. J. Lemstra & L. A. Kleintjens (Eds.), Integration of Fundamental Polymer Science and Technology—3 (pp. 178–198). Dordrecht: Springer Netherlands. https://doi.org/10.1007/978-94-009-1115-4_20

21. Naaman, A. E., Wongtanakitcharoen, T., & Hauser, G. (2005). Influence of Different Fibers on Plastic Shrinkage Cracking of Concrete. ACI Materials Journal, 102(1), 49–58.

22. Mukhopadhyay, S., & Khatana, S. (2015). A review on the use of fibers in reinforced cementitious concrete. Journal of Industrial Textiles, 45(2), 239–264. https://doi.org/10.1177/1528083714529806

23. Shakor, P., Nejadi, S., Paul, G., & Malek, S. (2019). Review of Emerging Additive Manufacturing Technologies in 3D Printing of Cementitious Materials in the Construction Industry. Frontiers in Built Environment, 4, 85. https://doi.org/10.3389/fbuil.2018.00085

24. Gardan, J. (2016). Additive manufacturing technologies: state of the art and trends. International Journal of Production Research, 54(10), 3118–3132. https://doi.org/10.1080/00207543.2015.1115909

25. Najmon, J. C., Raeisi, S., & Tovar, A. (2019). 2 - Review of additive manufacturing technologies and applications in the aerospace industry. In F. Froes & R. Boyer (Eds.), Additive Manufacturing for the Aerospace Industry (pp. 7–31). Elsevier. https://doi.org/10.1016/B978-0-12-814062-8.00002-9

26. Sing, S. L., Tey, C. F., Tan, J. H. K., Huang, S., & Yeong, W. Y. (2020). 2 - 3D printing of metals in rapid prototyping of biomaterials: Techniques in additive manufacturing. In R. Narayan (Ed.), Rapid Prototyping of Biomaterials (Second Edition) (pp. 17–40). Woodhead Publishing. https://doi.org/10.1016/B978-0-08-102663-2.00002-2

27. Chen, Z., Li, Z., Li, J., Liu, C., Lao, C., Fu, Y., … He, Y. (2019). 3D printing of ceramics: A review. Journal of the European Ceramic Society, 39(4), 661–687. https://doi.org/10.1016/j.jeurceramsoc.2018.11.013

28. Duda, T., & Raghavan, L. V. (2016). 3D Metal Printing Technology. IFAC-PapersOnLine, 49(29), 103–110. https://doi.org/10.1016/j.ifacol.2016.11.111

29. Singh, S., Ramakrishna, S., & Berto, F. (2020). 3D Printing of polymer composites: A short review. Material Design & Processing Communications, 2(2), e97. https://doi.org/10.1002/mdp2.97

30. A. Lifton, V., Lifton, G., & Simon, S. (2014). Options for additive rapid prototyping methods (3D printing) in MEMS technology. Rapid Prototyping Journal, 20(5), 403–412. https://doi.org/10.1108/RPJ-04-2013-0038

31. Ngo, T. D., Kashani, A., Imbalzano, G., Nguyen, K. T. Q., & Hui, D. (2018). Additive manufacturing (3D printing): A review of materials, methods, applications and challenges. Composites Part B: Engineering, 143, 172–196. https://doi.org/10.1016/j.compositesb.2018.02.012

32. Xiao, J., Ji, G., Zhang, Y., Ma, G., Mechtcherine, V., Pan, J., … Du, S. (2021). Large-scale 3D printing concrete technology: Current status and future opportunities. Cement and Concrete Composites, 122, 104115. https://doi.org/10.1016/j.cemconcomp.2021.104115

33. Zou, S., Xiao, J., Ding, T., Duan, Z., & Zhang, Q. (2021). Printability and advantages of 3D printing mortar with 100% recycled sand. Construction and Building Materials, 273, 121699. https://doi.org/10.1016/j.conbuildmat.2020.121699

34. Buswell, R. A., Leal de Silva, W. R., Jones, S. Z., & Dirrenberger, J. (2018). 3D printing using concrete extrusion: A roadmap for research. Cement and Concrete Research, 112, 37–49. https://doi.org/10.1016/j.cemconres.2018.05.006

35. Nematollahi, B., Xia, M., & Sanjayan, J. (2017). Current Progress of 3D Concrete Printing Technologies. https://doi.org/10.22260/ISARC2017/0035

36. Hossain, M. A., Zhumabekova, A., Paul, S. C., & Kim, J. R. (2020). A Review of 3D Printing in Construction and its Impact on the Labor Market. Sustainability, 12(20), 8492. https://doi.org/10.3390/su12208492

37. Delgado Camacho, D., Clayton, P., O'Brien, W. J., Seepersad, C., Juenger, M., Ferron, R., & Salamone, S. (2018). Applications of additive manufacturing in the construction industry – A forward-looking review. Automation in Construction, 89, 110–119. https://doi.org/10.1016/j.autcon.2017.12.031

38. Ooms, T., Vantyghem, G., Van Coile, R., & De Corte, W. (2021). A parametric modelling strategy for the numerical simulation of 3D concrete printing with complex geometries. Additive Manufacturing, 38, 101743. https://doi.org/10.1016/j.addma.2020.101743

39. Bos, F., Wolfs, R., Ahmed, Z., & Salet, T. (2016). Additive manufacturing of concrete in construction: potentials and challenges of 3D concrete printing. Virtual and Physical Prototyping, 11(3), 209–225. https://doi.org/10.1080/17452759.2016.1209867

40. Lim, S., Buswell, R. A., Le, T. T., Austin, S. A., Gibb, A. G. F., & Thorpe, T. (2012). Developments in construction-scale additive manufacturing processes. Automation in Construction, 21, 262–268. https://doi.org/10.1016/j.autcon.2011.06.010

41. Perrot, A., Rangeard, D., & Pierre, A. (2016). Structural built-up of cement-based materials used for 3D-printing extrusion techniques. Materials and Structures, 49(4), 1213–1220. https://doi.org/10.1617/s11527-015-0571-0

42. Nerella, V. N., Hempel, S., & Mechtcherine, V. (2019). Effects of layer-interface properties on mechanical performance of concrete elements produced by extrusion-based 3D-printing. Construction and Building Materials, 205, 586–601. https://doi.org/10.1016/j.conbuildmat.2019.01.235

43. Le, T. T., Austin, S. A., Lim, S., Buswell, R. A., Gibb, A. G. F., & Thorpe, T. (2012). Mix design and fresh properties for high-performance printing concrete. Materials and Structures, 45(8), 1221–1232. https://doi.org/10.1617/s11527-012-9828-z

44. Ghaffar, S. H., Corker, J., & Fan, M. (2018). Additive manufacturing technology and its implementation in construction as an eco-innovative solution. Automation in Construction, 93, 1–11. https://doi.org/10.1016/j.autcon.2018.05.005

45. Žujović, M., Obradović, R., Rakonjac, I., & Milošević, J. (2022). 3D Printing Technologies in Architectural Design and Construction: A Systematic Literature Review. Buildings, 12(9), 1319. https://doi.org/10.3390/buildings12091319

46. Paul, S. C., van, Z. G. P. A. G., Tan, M. J., & Gibson, I. (2018). A review of 3D concrete printing systems and materials properties: current status and future research prospects. Rapid Prototyping Journal, 24(4), 784–798. https://doi.org/10.1108/RPJ-09-2016-0154

47. Pessoa, S., Guimarães, A. S., Lucas, S. S., & Simões, N. (2021). 3D printing in the construction industry - A systematic review of the thermal performance in buildings. Renewable and Sustainable Energy Reviews, 141, 110794. https://doi.org/10.1016/j.rser.2021.110794

48. Danielsen Evjemo, L., Moe, S., Gravdahl, J. T., Roulet-Dubonnet, O., Gellein, L. T., & Br⊘tan, V. (2017). Additive manufacturing by robot manipulator: An overview of the state-of-the-art and proof-of-concept results. In 2017 22nd IEEE International Conference on Emerging Technologies and Factory Automation (ETFA) (pp. 1–8). Presented at the 2017 22nd IEEE International Conference on Emerging Technologies and Factory Automation (ETFA). https://doi.org/10.1109/ETFA.2017.8247617

49. Schuldt, S. J., Jagoda, J. A., Hoisington, A. J., & Delorit, J. D. (2021). A systematic review and analysis of the viability of 3D-printed construction in remote environments. Automation in Construction, 125, 103642. https://doi.org/10.1016/j.autcon.2021.103642

50. Roman, M. C., Kim, T., Sudnik, J., Cylar, R., Porter, M., Sivak, A., … Krome, K. (2017). Centennial Challenges Program Overview: How NASA Successfully Involves the General Public in the Solving of Current Technology Gaps. In AIAA SPACE and Astronautics Forum and Exposition. Presented at the AIAA SPACE and Astronautics Forum and Exposition, Orlando, FL: American Institute of Aeronautics and Astronautics. https://doi.org/10.2514/6.2017-5159

51. Chougan, M., Ghaffar, S. H., Sikora, P., Chung, S.-Y., Rucinska, T., Stephan, D., … Swash, M. R. (2021). Investigation of additive incorporation on rheological, microstructural and mechanical properties of 3D printable alkali-activated materials. Materials & Design, 202, 109574. https://doi.org/10.1016/j.matdes.2021.109574

52. Panda, B., Lim, J. H., & Tan, M. J. (2019). Mechanical properties and deformation behaviour of early age concrete in the context of digital construction. Composites Part B: Engineering, 165, 563–571. https://doi.org/10.1016/j.compositesb.2019.02.040

53. Mechtcherine, V., Bos, F. P., Perrot, A., da Silva, W. R. L., Nerella, V. N., Fataei, S., … Roussel, N. (2020). Extrusion-based additive manufacturing with cement-based materials – Production steps, processes, and their underlying physics: A review. Cement and Concrete Research, 132, 106037. https://doi.org/10.1016/j.cemconres.2020.106037

54. Bhattacherjee, S., Basavaraj, A. S., Rahul, A. V., Santhanam, M., Gettu, R., Panda, B., … Mechtcherine, V. (2021). Sustainable materials for 3D concrete printing. Cement and Concrete Composites, 122, 104156. https://doi.org/10.1016/j.cemconcomp.2021.104156

55. Dey, D., Srinivas, D., Panda, B., Suraneni, P., & Sitharam, T. G. (2022). Use of industrial waste materials for 3D printing of sustainable concrete: A review. Journal of Cleaner Production, 340, 130749. https://doi.org/10.1016/j.jclepro.2022.130749

56. Siddika, A., Mamun, Md. A. A., Ferdous, W., Saha, A. K., & Alyousef, R. (2020). 3D-printed concrete: applications, performance, and challenges. Journal of Sustainable Cement-Based Materials, 9(3), 127–164. https://doi.org/10.1080/21650373.2019.1705199

57. Javaid, M., Haleem, A., Singh, R. P., Suman, R., & Rab, S. (2021). Role of additive manufacturing applications towards environmental sustainability. Advanced Industrial and Engineering Polymer Research, 4(4), 312–322. https://doi.org/10.1016/j.aiepr.2021.07.005

58. Raza, M. H., & Zhong, R. Y. (2022). A sustainable roadmap for additive manufacturing using geopolymers in construction industry. Resources, Conservation and Recycling, 186, 106592. https://doi.org/10.1016/j.resconrec.2022.106592

59. Comminal, R., Leal da Silva, W. R., Andersen, T. J., Stang, H., & Spangenberg, J. (2020). Modelling of 3D concrete printing based on computational fluid dynamics. Cement and Concrete Research, 138, 106256. https://doi.org/10.1016/j.cemconres.2020.106256

60. Qian, Y., & Kawashima, S. (2018). Distinguishing dynamic and static yield stress of fresh cement mortars through thixotropy. Cement and Concrete Composites, 86, 288–296. https://doi.org/10.1016/j.cemconcomp.2017.11.019

61. Liu, Z., Li, M., Weng, Y., Wong, T. N., & Tan, M. J. (2019). Mixture Design Approach to optimize the rheological properties of the material used in 3D cementitious material printing. Construction and Building Materials, 198, 245–255. https://doi.org/10.1016/j.conbuildmat.2018.11.252

62. Zhang, Y., Zhang, Y., Liu, G., Yang, Y., Wu, M., & Pang, B. (2018). Fresh properties of a novel 3D printing concrete ink. Construction and Building Materials, 174, 263–271. https://doi.org/10.1016/j.conbuildmat.2018.04.115

63. Lu, B., Qian, Y., Li, M., Weng, Y., Leong, K. F., Tan, M. J., & Qian, S. (2019). Designing spray-based 3D printable cementitious materials with fly ash cenosphere and air entraining agent. Construction and Building Materials, 211, 1073–1084. https://doi.org/10.1016/j.conbuildmat.2019.03.186

64. Panda, B., & Tan, M. J. (2019). Rheological behavior of high volume fly ash mixtures containing micro silica for digital construction application. Materials Letters, 237, 348–351. https://doi.org/10.1016/j.matlet.2018.11.131

65. de Matos, P. R., Pilar, R., Casagrande, C. A., Gleize, P. J. P., & Pelisser, F. (2020). Comparison between methods for determining the yield stress of cement pastes. Journal of the Brazilian Society of Mechanical Sciences and Engineering, 42(1), 24. https://doi.org/10.1007/s40430-019-2111-2

66. Divoux, T., Barentin, C., & Manneville, S. (2011). Stress overshoot in a simple yield stress fluid: An extensive study combining rheology and velocimetry. Soft Matter, 7(19), 9335–9349. https://doi.org/10.1039/C1SM05740E

67. Chang, C., Boger, D. V., & Nguyen, Q. D. (1998). The Yielding of Waxy Crude Oils. Industrial & Engineering Chemistry Research, 37(4), 1551–1559. https://doi.org/10.1021/ie970588r

68. Güneyisi, E., Gesoglu, M., Naji, N., & İpek, S. (2016). Evaluation of the rheological behavior of fresh self-compacting rubberized concrete by using the Herschel-Bulkley and modified Bingham models. Archives of Civil and Mechanical Engineering, 16(1), 9–19. https://doi.org/10.1016/j.acme.2015.09.003

69. de Larrard, F., Ferraris, C. F., & Sedran, T. (1998). Fresh concrete: A Herschel-Bulkley material. Materials and Structures, 31(7), 494–498. https://doi.org/10.1007/BF02480474

70. Chen, M., Yang, L., Zheng, Y., Huang, Y., Li, L., Zhao, P., … Cheng, X. (2020). Yield stress and thixotropy control of 3D-printed calcium sulfoaluminate cement composites with metakaolin related to structural build-up. Construction and Building Materials, 252, 119090. https://doi.org/10.1016/j.conbuildmat.2020.119090

71. Jayathilakage, R., Sanjayan, J., & Rajeev, P. (2019). Direct shear test for the assessment of rheological parameters of concrete for 3D printing applications. Materials and Structures, 52(1), 12. https://doi.org/10.1617/s11527-019-1322-4

72. Weng, Y., Lu, B., Li, M., Liu, Z., Tan, M. J., & Qian, S. (2018). Empirical models to predict rheological properties of fiber reinforced cementitious composites for 3D printing. Construction and Building Materials, 189, 676–685. https://doi.org/10.1016/j.conbuildmat.2018.09.039

73. Chen, M., Liu, B., Li, L., Cao, L., Huang, Y., Wang, S., … Cheng, X. (2020). Rheological parameters, thixotropy and creep of 3D-printed calcium sulfoaluminate cement composites modified by bentonite. Composites Part B: Engineering, 186, 107821. https://doi.org/10.1016/j.compositesb.2020.107821

74. Tay, Y. W. D., Ting, G. H. A., Qian, Y., Panda, B., He, L., & Tan, M. J. (2019). Time gap effect on bond strength of 3D-printed concrete. Virtual and Physical Prototyping, 14(1), 104–113. https://doi.org/10.1080/17452759.2018.1500420

75. Rubio-Hernández, F. J., Velázquez-Navarro, J. F., & Galindo-Rosales, F. J. (2009). Rheological characterization of a time dependent fresh cement paste. Mechanics of Time-Dependent Materials, 13(2), 199–206. https://doi.org/10.1007/s11043-009-9078-9

76. Feys, D., Cepuritis, R., Jacobsen, S., Lesage, K., Secrieru, E., & Yahia, A. (2017). Measuring Rheological Properties of Cement Pastes: Most common Techniques, Procedures and Challenges. RILEM Technical Letters, 2, 129–135. https://doi.org/10.21809/rilemtechlett.2017.43

77. Ranjbar, N., Mehrali, M., Kuenzel, C., Gundlach, C., Pedersen, D. B., Dolatshahi-Pirouz, A., & Spangenberg, J. (2021). Rheological characterization of 3D printable geopolymers. Cement and Concrete Research, 147, 106498. https://doi.org/10.1016/j.cemconres.2021.106498

78. Ivanova, I., Ivaniuk, E., Bisetti, S., Nerella, V. N., & Mechtcherine, V. (2022). Comparison between methods for indirect assessment of buildability in fresh 3D printed mortar and concrete. Cement and Concrete Research, 156, 106764. https://doi.org/10.1016/j.cemconres.2022.106764

79. Moeini, M. A., Hosseinpoor, M., & Yahia, A. (2020). Effectiveness of the rheometric methods to evaluate the build-up of cementitious mortars used for 3D printing. Construction and Building Materials, 257, 119551. https://doi.org/10.1016/j.conbuildmat.2020.119551

80. Marchon, D., Kawashima, S., Bessaies-Bey, H., Mantellato, S., & Ng, S. (2018). Hydration and rheology control of concrete for digital fabrication: Potential admixtures and cement chemistry. Cement and Concrete Research, 112, 96–110. https://doi.org/10.1016/j.cemconres.2018.05.014

81. Tarhan, Y., & Şahin, R. (2021). Fresh and Rheological Performances of Air-Entrained 3D Printable Mortars. Materials, 14(9), 2409. https://doi.org/10.3390/ma14092409

82. Chen, Y., Chaves Figueiredo, S., Li, Z., Chang, Z., Jansen, K., Çopuroğlu, O., & Schlangen, E. (2020). Improving printability of limestone-calcined clay-based cementitious materials by using viscosity-modifying admixture. Cement and Concrete Research, 132, 106040. https://doi.org/10.1016/j.cemconres.2020.106040

83. Sikora, P., Chung, S.-Y., Liard, M., Lootens, D., Dorn, T., Kamm, P. H., … Abd Elrahman, M. (2021). The effects of nanosilica on the fresh and hardened properties of 3D printable mortars. Construction and Building Materials, 281, 122574. https://doi.org/10.1016/j.conbuildmat.2021.122574

84. Wang, Y., Jiang, Y., Pan, T., & Yin, K. (2021). The Synergistic Effect of Ester-Ether Copolymerization Thixo-Tropic Superplasticizer and Nano-Clay on the Buildability of 3D Printable Cementitious Materials. Materials, 14(16), 4622. https://doi.org/10.3390/ma14164622

85. Tay, Y. W. D., Panda, B., Paul, S. C., Noor Mohamed, N. A., Tan, M. J., & Leong, K. F. (2017). 3D printing trends in building and construction industry: a review. Virtual and Physical Prototyping, 12(3), 261–276. https://doi.org/10.1080/17452759.2017.1326724

86. Asprone, D., Auricchio, F., Menna, C., & Mercuri, V. (2018). 3D printing of reinforced concrete elements: Technology and design approach. Construction and Building Materials, 165, 218–231. https://doi.org/10.1016/j.conbuildmat.2018.01.018

87. Panda, B., & Tan, M. J. (2018). Experimental study on mix proportion and fresh properties of fly ash based geopolymer for 3D concrete printing. Ceramics International, 44(9), 10258–10265. https://doi.org/10.1016/j.ceramint.2018.03.031

88. Chang, Z., Zhang, H., Liang, M., Schlangen, E., & Šavija, B. (2022). Numerical simulation of elastic buckling in 3D concrete printing using the lattice model with geometric nonlinearity. Automation in Construction, 142, 104485. https://doi.org/10.1016/j.autcon.2022.104485

89. Nguyen-Van, V., Nguyen-Xuan, H., Panda, B., & Tran, P. (2022). 3D concrete printing modelling of thin-walled structures. Structures, 39, 496–511. https://doi.org/10.1016/j.istruc.2022.03.049

90. Suiker, A. S. J., Wolfs, R. J. M., Lucas, S. M., & Salet, T. A. M. (2020). Elastic buckling and plastic collapse during 3D concrete printing. Cement and Concrete Research, 135, 106016. https://doi.org/10.1016/j.cemconres.2020.106016

91. Panda, B., Noor Mohamed, N. A., Paul, S. C., Bhagath Singh, G. V. P., Tan, M. J., & Šavija, B. (2019). The Effect of Material Fresh Properties and Process Parameters on Buildability and Interlayer Adhesion of 3D Printed Concrete. Materials, 12(13), 2149. https://doi.org/10.3390/ma12132149

92. Jayathilakage, R., Rajeev, P., & Sanjayan, J. (2022). Rheometry for Concrete 3D Printing: A Review and an Experimental Comparison. Buildings, 12(8), 1190. https://doi.org/10.3390/buildings12081190

93. Wolfs, R. J. M., Bos, F. P., & Salet, T. A. M. (2018). Early age mechanical behaviour of 3D printed concrete: Numerical modelling and experimental testing. Cement and Concrete Research, 106, 103–116. https://doi.org/10.1016/j.cemconres.2018.02.001

94. Zhang, N., & Sanjayan, J. (2023). Extrusion nozzle design and print parameter selections for 3D concrete printing. Cement and Concrete Composites, 137, 104939. https://doi.org/10.1016/j.cemconcomp.2023.104939

95. Assaedi, H., Alomayri, T., Kaze, C. R., Jindal, B. B., Subaer, S., Shaikh, F., & Alraddadi, S. (2020). Characterization and properties of geopolymer nanocomposites with different contents of nano-CaCO3. Construction and Building Materials, 252, 119137. https://doi.org/10.1016/j.conbuildmat.2020.119137

96. Mahboubi, B., Guo, Z., & Wu, H. (2019). Evaluation of Durability Behavior of Geopolymer Concrete Containing Nano-Silica and Nano-Clay Additives in Acidic Media. Journal of Civil Engineering and Materials Application, 3(3). https://doi.org/10.22034/jcema.2019.95839

97. Sun, X., Wang, Q., Wang, H., & Chen, L. (2020). Influence of multi-walled nanotubes on the fresh and hardened properties of a 3D printing PVA mortar ink. Construction and Building Materials, 247, 118590. https://doi.org/10.1016/j.conbuildmat.2020.118590

98. Afroz, M., Venkatesan, S., & Patnaikuni, I. (2019). Effects of hybrid fibers on the development of high volume fly ash cement composite. Construction and Building Materials, 215, 984–997. https://doi.org/10.1016/j.conbuildmat.2019.04.083

99. Ali, B., & Qureshi, L. A. (2019). Influence of glass fibers on mechanical and durability performance of concrete with recycled aggregates. Construction and Building Materials, 228, 116783. https://doi.org/10.1016/j.conbuildmat.2019.116783

100. Das, C. S., Dey, T., Dandapat, R., Mukharjee, B. B., & Kumar, J. (2018). Performance evaluation of polypropylene fibre reinforced recycled aggregate concrete. Construction and Building Materials, 189, 649–659. https://doi.org/10.1016/j.conbuildmat.2018.09.036

101. Chen, M., Li, L., Wang, J., Huang, Y., Wang, S., Zhao, P., … Cheng, X. (2020). Rheological parameters and building time of 3D printing sulphoaluminate cement paste modified by retarder and diatomite. Construction and Building Materials, 234, 117391. https://doi.org/10.1016/j.conbuildmat.2019.117391

102. Mostafa, A. M., & Yahia, A. (2016). New approach to assess build-up of cement-based suspensions. Cement and Concrete Research, 85, 174–182. https://doi.org/10.1016/j.cemconres.2016.03.005

103. He, Z., Jiang, R., & Li, Y. (2018). Dynamic Rheological Behavior of Low Water-to-binder Ratio Mortars under Large Amplitude Oscillatory Shear (LAOS). Journal of Wuhan University of Technology-Mater. Sci. Ed., 33(3), 608–618. https://doi.org/10.1007/s11595-018-1868-y

104. Yuan, Q., Lu, X., Khayat, K. H., Feys, D., & Shi, C. (2016). Small amplitude oscillatory shear technique to evaluate structural build-up of cement paste. Materials and Structures, 50(2), 112. https://doi.org/10.1617/s11527-016-0978-2

105. Saasen, A., Marken, C., Dawson, J., & Rogers, M. (1991). Oscillating rheometer measurements on oilfield cement slurries. Cement and Concrete Research, 21(1), 109–119. https://doi.org/10.1016/0008-8846(91)90037-I

106. Yokota, H., Rokugo, K., & Sakata, N. (2007). Recommendations for Design and Construction of High Performance Fiber Reinforced Cement Composite with Multiple Fine Cracks. Retrieved from https://www.semanticscholar.org/paper/Recommendations-for-Design-and-Construction-of-High-Yokota-Rokugo/3c6fd2115706186a9841674260fe2ff8a9b2e65a

107. 332.1R-06 Guide to Residential Concrete Construction. (n.d.), 52.

108. Panda, B., Ruan, S., Unluer, C., & Tan, M. J. (2019). Improving the 3D printability of high volume fly ash mixtures via the use of nano attapulgite clay. Composites Part B: Engineering, 165, 75–83. https://doi.org/10.1016/j.compositesb.2018.11.109

109. Eugenin, C., Navarrete, I., Brevis, W., & Lopez, M. (2022). Air Bubbles as an Admixture for Printable Concrete: A Review of the Rheological Effect of Entrained Air. 3D Printing and Additive Manufacturing, 9(1), 64–80. https://doi.org/10.1089/3dp.2020.0302

110. Kawashima, S., Kim, J. H., Corr, D. J., & Shah, S. P. (2012). Study of the mechanisms underlying the fresh-state response of cementitious materials modified with nanoclays. Construction and Building Materials, 36, 749–757. https://doi.org/10.1016/j.conbuildmat.2012.06.057

111. Ma, S., Qian, Y., & Kawashima, S. (2018). Performance-based study on the rheological and hardened properties of blended cement mortars incorporating palygorskite clays and carbon nanotubes. Construction and Building Materials, 171, 663–671. https://doi.org/10.1016/j.conbuildmat.2018.03.121

112. Cao, E., Bryant, R., & Williams, D. J. A. (1996). Electrochemical Properties of Na–Attapulgite. Journal of Colloid and Interface Science, 179(1), 143–150. https://doi.org/10.1006/jcis.1996.0196

113. Roussel, N., Ovarlez, G., Garrault, S., & Brumaud, C. (2012). The origins of thixotropy of fresh cement pastes. Cement and Concrete Research, 42(1), 148–157. https://doi.org/10.1016/j.cemconres.2011.09.004

114. Qian, Y., & Kawashima, S. (2016). Use of creep recovery protocol to measure static yield stress and structural rebuilding of fresh cement pastes. Cement and Concrete Research, 90, 73–79. https://doi.org/10.1016/j.cemconres.2016.09.005

115. Nehdi, M., & Al Martini, S. (2007). Effect of Temperature on Oscillatory Shear Behavior of Portland Cement Paste Incorporating Chemical Admixtures. Journal of Materials in Civil Engineering, 19(12), 1090–1100. https://doi.org/10.1061/(ASCE)0899-1561(2007)19:12(1090)

116. Ma, S., Qian, Y., & Kawashima, S. (2018). Experimental and modeling study on the non-linear structural build-up of fresh cement pastes incorporating viscosity modifying admixtures. Cement and Concrete Research, 108, 1–9. https://doi.org/10.1016/j.cemconres.2018.02.022

117. Tregger, N. A., Pakula, M. E., & Shah, S. P. (2010). Influence of clays on the rheology of cement pastes. Cement and Concrete Research, 40(3), 384–391. https://doi.org/10.1016/j.cemconres.2009.11.001

118. Jain, S., & Pradhan, B. (2019). Effect of cement type on hydration, microstructure and thermo-gravimetric behaviour of chloride admixed self-compacting concrete. Construction and Building Materials, 212, 304–316. https://doi.org/10.1016/j.conbuildmat.2019.04.001

119. Deboucha, W., Leklou, N., Khelidj, A., & Oudjit, M. N. (2017). Hydration development of mineral additives blended cement using thermogravimetric analysis (TGA): Methodology of calculating the degree of hydration. Construction and Building Materials, 146, 687–701. https://doi.org/10.1016/j.conbuildmat.2017.04.132

120. Massana, J., Reyes, E., Bernal, J., León, N., & Sánchez-Espinosa, E. (2018). Influence of nano- and micro-silica additions on the durability of a high-performance self-compacting concrete. Construction and Building Materials, 165, 93–103. https://doi.org/10.1016/j.conbuildmat.2017.12.100

121. Lin, K. L., Chang, W. C., Lin, D. F., Luo, H. L., & Tsai, M. C. (2008). Effects of nano-SiO2 and different ash particle sizes on sludge ash–cement mortar. Journal of Environmental Management, 88(4), 708–714. https://doi.org/10.1016/j.jenvman.2007.03.036

122. Casagrande, L., Esposito, L., Menna, C., Asprone, D., & Auricchio, F. (2020). Effect of testing procedures on buildability properties of 3D-printable concrete. Construction and Building Materials, 245, 118286. https://doi.org/10.1016/j.conbuildmat.2020.118286

123. Peng, Y., Gardner, D. J., & Han, Y. (2012). Drying cellulose nanofibrils: in search of a suitable method. Cellulose, 19(1), 91–102. https://doi.org/10.1007/s10570-011-9630-z

124. Cengiz, A., Kaya, M., & Pekel Bayramgil, N. (2017). Flexural stress enhancement of concrete by incorporation of algal cellulose nanofibers. Construction and Building Materials, 149, 289–295. https://doi.org/10.1016/j.conbuildmat.2017.05.104

125. Mònica Ardanuy, Josep Claramunt, Raquel Arévalo, Ferran Parés, Elisabetta Aracri, & Vidal, T. (2012). NANOFIBRILLATED CELLULOSE (NFC) AS A POTENTIAL REINFORCEMENT FOR HIGH PERFORMANCE CEMENT MORTAR COMPOSITES. BioResources, 7(3), 3883–3894.

126. Flores, J., Kamali, M., & Ghahremaninezhad, A. (2017). An Investigation into the Properties and Microstructure of Cement Mixtures Modified with Cellulose Nanocrystal. Materials, 10(5), 498. https://doi.org/10.3390/ma10050498

127. Mejdoub, R., Hammi, H., Suñol, J. J., Khitouni, M., M'nif, A., & Boufi, S. (2017). Nanofibrillated cellulose as nanoreinforcement in Portland cement: Thermal, mechanical and microstructural properties. Journal of Composite Materials, 51(17), 2491–2503. https://doi.org/10.1177/0021998316672090

128. Zhang, Z., & Angst, U. (2022). Microstructure and moisture transport in carbonated cement-based materials incorporating cellulose nanofibrils. Cement and Concrete Research, 162, 106990. https://doi.org/10.1016/j.cemconres.2022.106990

129. Števulová, N., Hospodarova, V., Václavík, V., & Dvorský, T. (2020). Physico-Mechanical Properties of Cellulose Fiber-Cement Mortars. Key Engineering Materials, 838, 31–38. Presented at the Advances in Environmental Engineering. https://doi.org/10.4028/www.scientific.net/KEM.838.31

130. Bentz, D. P. (2006). Influence of water-to-cement ratio on hydration kinetics: Simple models based on spatial considerations. Cement and Concrete Research, 36(2), 238–244. https://doi.org/10.1016/j.cemconres.2005.04.014

131. Patural, L., Marchal, P., Govin, A., Grosseau, P., Ruot, B., & Devès, O. (2011). Cellulose ethers influence on water retention and consistency in cement-based mortars. Cement and Concrete Research, 41(1), 46–55. https://doi.org/10.1016/j.cemconres.2010.09.004

132. Lee, H.-J., Kim, S.-K., Lee, H.-S., & Kim, W. (2019). A Study on the Drying Shrinkage and Mechanical Properties of Fiber Reinforced Cement Composites Using Cellulose Nanocrystals. International Journal of Concrete Structures and Materials, 13(1), 39. https://doi.org/10.1186/s40069-019-0351-2

133. El-Feky, M. S., Youssef, P., El-Tair, A. M., Ibrahim, S., & Serag, M. (n.d.). Effect of nano silica addition on enhancing the performance of cement composites reinforced with nano cellulose fibers. AIMS Materials Science, 6(6).

134. Kohail, M., Elfeky, M., Maher, A., & Serag, M. (2019). Nano-Fibrillated Cellulose as a Green Alternative to Carbon Nanotubes in Nano Reinforced Cement Composites, 8, 484–491. https://doi.org/10.35940/ijitee.L3377.1081219

135. Hisseine, O. A., Basic, N., Omran, A. F., & Tagnit-Hamou, A. (2018). Feasibility of using cellulose filaments as a viscosity modifying agent in self-consolidating concrete. Cement and Concrete Composites, 94, 327–340. https://doi.org/10.1016/j.cemconcomp.2018.09.009

136. Cao, Y., Zavattieri, P., Youngblood, J., Moon, R., & Weiss, J. (2016). The relationship between cellulose nanocrystal dispersion and strength. Construction and Building Materials, 119, 71–79. https://doi.org/10.1016/j.conbuildmat.2016.03.077

137. Jiang, Z., Sevim, O., & Ozbulut, O. E. (2021). Mechanical properties of graphene nanoplatelets-reinforced concrete prepared with different dispersion techniques. Construction and Building Materials, 303, 124472. https://doi.org/10.1016/j.conbuildmat.2021.124472

138. Krystek, M., Ciesielski, A., & Samorì, P. (2021). Graphene-Based Cementitious Composites: Toward Next-Generation Construction Technologies. Advanced Functional Materials, 31(27), 2101887. https://doi.org/10.1002/adfm.202101887

139. Dalla, P. T., Tragazikis, I. K., Trakakis, G., Galiotis, C., Dassios, K. G., & Matikas, T. E. (2021). Multifunctional Cement Mortars Enhanced with Graphene Nanoplatelets and Carbon Nanotubes. Sensors, 21(3), 933. https://doi.org/10.3390/s21030933

140. Meng, W., & Khayat, K. H. (2016). Mechanical properties of ultra-high-performance concrete enhanced with graphite nanoplatelets and carbon nanofibers. Composites Part B: Engineering, 107, 113–122. https://doi.org/10.1016/j.compositesb.2016.09.069

141. Ma, G., Li, Z., Wang, L., Wang, F., & Sanjayan, J. (2019). Mechanical anisotropy of aligned fiber reinforced composite for extrusion-based 3D printing. Construction and Building Materials, 202, 770–783. https://doi.org/10.1016/j.conbuildmat.2019.01.008

142. Xiao, J., Liu, H., & Ding, T. (2021). Finite element analysis on the anisotropic behavior of 3D printed concrete under compression and flexure. Additive Manufacturing, 39, 101712. https://doi.org/10.1016/j.addma.2020.101712

143. Liu, J., & Lv, C. (2022). Properties of 3D-Printed Polymer Fiber-Reinforced Mortars: A Review. Polymers, 14(7), 1315. https://doi.org/10.3390/polym14071315

144. Xu, Z., Zhang, D., Li, H., Sun, X., Zhao, K., & Wang, Y. (2022). Effect of FA and GGBFS on compressive strength, rheology, and printing properties of cement-based 3D printing material. Construction and Building Materials, 339, 127685. https://doi.org/10.1016/j.conbuildmat.2022.127685

145. Lee, H., Kim, J.-H. J., Moon, J.-H., Kim, W.-W., & Seo, E.-A. (2019). Evaluation of the Mechanical Properties of a 3D-Printed Mortar. Materials, 12(24), 4104. https://doi.org/10.3390/ma12244104

146. Alchaar, A. S., & Al-Tamimi, A. K. (2021). Mechanical properties of 3D printed concrete in hot temperatures. Construction and Building Materials, 266, 120991. https://doi.org/10.1016/j.conbuildmat.2020.120991

147. Kalantari, B., Mohaddes Mojtahedi, M. R., Sharif, F., & Semnani Rahbar, R. (2015). Effect of graphene nanoplatelets presence on the morphology, structure, and thermal properties of polypropylene in fiber melt-spinning process. Polymer Composites, 36(2), 367–375. https://doi.org/10.1002/pc.22951

148. Sutar, H., Mishra, B., Senapati, P., Murmu, R., & Sahu, D. (2021). Mechanical, Thermal, and Morphological Properties of Graphene Nanoplatelet-Reinforced Polypropylene Nanocomposites: Effects of Nanofiller Thickness. Journal of Composites Science, 5(1), 24. https://doi.org/10.3390/jcs5010024

149. Chatterjee, S., Nüesch, F. A., & Chu, B. T. T. (2013). Crystalline and tensile properties of carbon nanotube and graphene reinforced polyamide 12 fibers. Chemical Physics Letters, 557, 92–96. https://doi.org/10.1016/j.cplett.2012.11.091

150. Sevim, O., Jiang, Z., & Ozbulut, O. E. (2022). Effects of graphene nanoplatelets type on self-sensing properties of cement mortar composites. Construction and Building Materials, 359, 129488. https://doi.org/10.1016/j.conbuildmat.2022.129488

151. Li, Z., Sheikh, M. N., Feng, H., & Hadi, M. N. S. (2022). Mechanical properties of engineered geopolymer composite with graphene nanoplatelet. Ceramics International, 48(23, Part A), 34915–34930. https://doi.org/10.1016/j.ceramint.2022.08.081

152. Du, H., Gao, H. J., & Pang, S. D. (2016). Improvement in concrete resistance against water and chloride ingress by adding graphene nanoplatelet. Cement and Concrete Research, 83, 114–123. https://doi.org/10.1016/j.cemconres.2016.02.005

153. Zhang, Y., Cui, M., Chen, G., & Han, W. (2022). Experimental study of the effects of graphene nanoplatelets on microstructure and compressive properties of concrete under

chloride ion corrosion. Construction and Building Materials, 360, 129564. https://doi.org/10.1016/j.conbuildmat.2022.129564

154. Saruhan, V., Keskinateş, M., & Felekoğlu, B. (2022). A comprehensive review on fresh state rheological properties of extrusion mortars designed for 3D printing applications. Construction and Building Materials, 337, 127629. https://doi.org/10.1016/j.conbuildmat.2022.127629

155. Fu, C., Guo, R., Lin, Z., Xia, H., Yang, Y., & Ma, Q. (2021). Effect of nanosilica and silica fume on the mechanical properties and microstructure of lightweight engineered cementitious composites. Construction and Building Materials, 298, 123788. https://doi.org/10.1016/j.conbuildmat.2021.123788

156. Hanehara, S., & Yamada, K. (2008). Rheology and early age properties of cement systems. In Cement and concrete research (Vol. 38, pp. 175–195). Presented at the Cement Systems - A Knowledge-based Approach. Retrieved from http://pascal-francis.inist.fr/vibad/index.php?action=getRecordDetail&idt=20077345

157. Chen, M., Li, L., Zheng, Y., Zhao, P., Lu, L., & Cheng, X. (2018). Rheological and mechanical properties of admixtures modified 3D printing sulphoaluminate cementitious materials. Construction and Building Materials, 189, 601–611. https://doi.org/10.1016/j.conbuildmat.2018.09.037

158. Bentur, A., & Akers, S. A. S. (1989). The microstructure and ageing of cellulose fibre reinforced cement composites cured in a normal environment. International Journal of Cement Composites and Lightweight Concrete, 11(2), 99–109. https://doi.org/10.1016/0262-5075(89)90120-6

159. Banthia, N., & Soleimani, S. M. (2005). Flexural Response of Hybrid Fiber-Reinforced Cementitious Composites. ACI Materials Journal, 102(6), 382–389.

160. Lin, Z., & Li, V. C. (1997). Crack bridging in fiber reinforced cementitious composites with slip-hardening interfaces. Journal of the Mechanics and Physics of Solids, 45(5), 763–787. https://doi.org/10.1016/S0022-5096(96)00095-6

161. Zhang, D., Yu, J., Wu, H., Jaworska, B., Ellis, B. R., & Li, V. C. (2020). Discontinuous micro-fibers as intrinsic reinforcement for ductile Engineered Cementitious Composites (ECC). Composites Part B: Engineering, 184, 107741. https://doi.org/10.1016/j.compositesb.2020.107741

162. Liu, D., Yu, J., Qin, F., Zhang, K., & Zhang, Z. (2023). Mechanical performance of high-strength engineering cementitious composites (ECC) with hybriding PE and steel fibers. Case Studies in Construction Materials, 18, e01961. https://doi.org/10.1016/j.cscm.2023.e01961

163. Yao, W., Li, J., & Wu, K. (2003). Mechanical properties of hybrid fiber-reinforced concrete at low fiber volume fraction. Cement and Concrete Research, 33(1), 27–30. https://doi.org/10.1016/S0008-8846(02)00913-4

164. Hu, C., Li, L., & Li, Z. (2022). Effect of fiber factor on the workability and mechanical properties of polyethylene fiber-reinforced high toughness geopolymers. Ceramics International, 48(8), 10458–10471. https://doi.org/10.1016/j.ceramint.2021.12.254

165. Tang, Z., Chen, D., Wang, X., Han, Z., Tao, R., Zhang, G., … Ding, Q. (2023). Impact of polyethylene fiber on the ductility and durability of magnesium phosphate cement. Journal of Building Engineering, 68, 106123. https://doi.org/10.1016/j.jobe.2023.106123

166. Zhu, S., Zhang, Y. X., & Lee, C. K. (2022). Experimental investigation of flexural behaviours of hybrid engineered cementitious composite beams under static and fatigue loading. Engineering Structures, 262, 114369. https://doi.org/10.1016/j.engstruct.2022.114369

167. Fu, S.-Y., & Lauke, B. (1996). Effects of fiber length and fiber orientation distributions on the tensile strength of short-fiber-reinforced polymers. Composites Science and Technology, 56(10), 1179–1190. https://doi.org/10.1016/S0266-3538(96)00072-3

168. González-Aviña, J. V., Juárez-Alvarado, C. A., Terán-Torres, B. T., Mendoza-Rangel, J. M., Durán-Herrera, A., & Rodríguez-Rodríguez, J. A. (2022). Influence of fibers distribution on direct shear and flexural behavior of synthetic fiber-reinforced self-compacting concrete. Construction and Building Materials, 330, 127255. https://doi.org/10.1016/j.conbuildmat.2022.127255

169. Yoo, D.-Y., Oh, T., & Chun, B. (2021). Highly ductile ultra-rapid-hardening mortar containing oxidized polyethylene fibers. Construction and Building Materials, 277, 122317. https://doi.org/10.1016/j.conbuildmat.2021.122317

170. Yu, K.-Q., Yu, J.-T., Dai, J.-G., Lu, Z.-D., & Shah, S. P. (2018). Development of ultra-high performance engineered cementitious composites using polyethylene (PE) fibers. Construction and Building Materials, 158, 217–227. https://doi.org/10.1016/j.conbuildmat.2017.10.040

171. Xiao, J., Zou, S., Ding, T., Duan, Z., & Liu, Q. (2021). Fiber-reinforced mortar with 100% recycled fine aggregates: A cleaner perspective on 3D printing. Journal of Cleaner Production, 319, 128720. https://doi.org/10.1016/j.jclepro.2021.128720

172. Effect of polyethylene fiber content on workability and mechanical-anisotropic properties of 3D printed ultra-high ductile concrete. (2021). Construction and Building Materials, 281, 122586. https://doi.org/10.1016/j.conbuildmat.2021.122586

173. Gangotra, A., Del Gado, E., & Lewis, J. I. (2023). 3D printing has untapped potential for climate mitigation in the cement sector. Communications Engineering, 2(1), 1–5. https://doi.org/10.1038/s44172-023-00054-7